Republic of Iraq

Ministry of Higher Education and

Scientific Research

University of Babylon

Faculty of Materials Engineering

Department of Metallurgical Engineering

Investigation the Effect of Laser Welding Processes and Their Parameters on Titanium Alloy Welds

A Thesis

Submitted to the Council of the Faculty of Materials Engineering/University of Babylon in Partial Fulfillment of the Requirements for the PhD Degree in Materials Engineering/Metallurgical Engineering

by

Marwa Mohammed Abdul Redha

Master's Degree in Material Eng./Metallurgical Eng.

Supervised by

Assist. Prof. Dr. Abdul Sameea J. A. Z. Jilabi

2023 A.D **1444 A.H**

بسم الله الرحمن الرحيم

((وَالرَّاسِخُونَ فِي الْعِلْمِ يَقُولُونَ آمَنَّا بِهِ كُلٌّ مِنْ عِنْدِ رَبِّنَا))

صدق الله العلي العظيم

(آل عمران: آية : 7)

الاهداء

إلى من كلله الله بالهيبة والوقار ..إلى من علمني العطاء بدون انتظار ..إلى من احمل اسمه بكل افتخار ..أرجو من الله أن يمد في عمرك لترى ثمارا ق حان قطافها بعد طول انتظار

(والدي العزيز)

إلى ملاكي في الحياة.. إلى معنى الحب والى معنى الحنان والتفاني ..إلى بسمة الحياة وسر الوجود..إلى من كان دعائها سر نجاحي وحنانها بلسم جراحي.. إلى من فارقت الدنيا بجسدها ولكن روحها لا تزال بجانبي ...إلى أغلى الحبايب

(أمي الحبيبة)

إلى من هم اقرب آلي من روحي ..إلى من شاركني حضن الأم وبهم استمد عزتي وإصراري (إخوتي)

إلى من تحملني وساندني وشاركني مصاعب مسيرتي

(زوجي وأطفالي)

MARWA MOHAMMED

Acknowledgments

First, I thank God for the blessing of health, determination, and patience that He granted me to challenge the difficulties I faced to complete this research.

It really gives me great pleasure to express my deepest gratitude and gratitude to my mentor and mentor, ***Asst.Prof.Dr.Abdul Sameea Jasim Abdul Zahra*** for his great interest and sincerity in supporting me in every stage of my studies, he was mainly responsible for finishing my work. His constant scholarly advice, meticulous scrutiny, and scientific approach have enabled me largely to complete my dissertation.

I also extend my thanks to the staff of the Metallurgical Engineering Department, the University of Babylon / The College of Materials Engineering, and the University of Kufa /Department of Materials to help me.

Finally, I extend my thanks and appreciation to my family, my parents, and my husband for their financial and moral support throughout the study period.

Supervisor Certificate

I certify that this thesis entitled "***Investigation the Effect of Laser Welding Processes and Their Parameters on Titanium Alloy Welds***" is prepared by **(*Marwa Mohammed Abdul Redha*)** under my supervision at the Department of Metallurgical Engineering/Faculty of Materials Engineering/University of Babylon in partial fulfillment of the requirements for the Ph.D. Degree in Materials Engineering/Metallurgical Engineering.

Signature:

Name of Supervisor:

Assist. Prof. Dr. Abdul Sameea J. A. Z. Jilabi

Date: / / 2023

(Examining committee Certification)

We certify that have read this thesis entitled **" *Investigation the Effect of Laser Welding Processes and Their Parameters on Titanium Alloy Welds*** " and as an examining committee,we have examined the student**(*Marwa Mohammed Abdul Redha*)** in contents and that is related to it, and that in our opinion it meets the standard of a thesis for the degree of Philosophy-Doctorate in Materials Engineering/ Metallurgical.

Signature:
Prof. Dr. Ahmed O. Al-Roubaiy
(Committee Chair)
Date: / /2023

Signature:
Prof. Dr.Abdul Rahman Najem Abed
(Committee Member)
Date : / / 2023

Signature:
Prof. Dr. Ahmed Ameed Zainulabdeen
(Committee Member)
Date : / / 2023

Signature:
Asst. Prof. Dr. Akeel Dhahir Subhi
(Committee Member)
Date : / / 2023

Signature:
Ass. Prof. Dr. Basem M. AL-Zubaid
(Committee Member)
Date : / / 2023

Signature:
Asst.Prof. Dr. Abdul Sameea J.A.Z.Jilabi
(supervisor)
Date : / / 2023

Approval of the Department of Matellurgical Engineering
Head of Department

Approval of the College of Materials Engineering
Dean of the College

Signature:
Prof. Dr.Saad Hameed Al-Shafaie
Date : / / 2023

Signature:
Prof. Dr.Imad Ali Disher
Date : / / 2023

Abstract

Titanium (Ti) alloys are engineering materials widely used in various fields including aviation, marine, petrochemical, sports, medical and more. During manufacturing, all of these applications require the use of welding processes. Laser welding is one of the most important processes used to weld Ti alloys, because Ti has a high reactivity with atmospheric components at high temperatures. This leads to the formation of hard and brittle compounds that promote the development of weld defects. Therefore, it requires the use of inert gas shielded welding processes.

The research objectives are to study the effect of changing laser welding methods and welding parameters on Ti alloy welds. It is study the effect of these parameters on weld geometry (weld penetration depth and weld zone width), HAZ width, microstructure, hardness, tensile strength and fracture surfaces.

In this work, continuous fiber and pulsed Nd:YAG lasers were used for welding similar 3mm thick butt joints of CP-Ti and Ti-6Al-4V alloys. Two variables were selected for each welding method: laser power and welding speed with four values for each variable. Several tests have been carried out to evaluate the performance of laser welds, including non-destructive tests (energy dispersive spectrometry, X-ray diffraction, X-ray radiography and macrography to measure the HAZ width). Other tests such as optical and scanning electron microscopy, microhardness, tensile test and fractography were also performed.

The most important results showed that the HAZ width in fiber laser welds decreased with increasing welding speed. The HAZ's of the Ti-6Al-4V alloy welds were wider than those that appeared in the CP-Ti welds. The maximum penetration depths of the Nd:YAG CP-Ti and Ti-6Al-4V welds, joined from both sides, were slightly higher than those of the one side fiber welds. The fusion zone (FZ) microstructure of the CP-Ti laser welds

consisted of acicular α, and there was no martensite formed. However, the FZ structure of the Ti-6Al-4V welds showed an acicular α` (martensite) phase. The HAZ microstructure of the CP-Ti welds was mainly composed of acicular α near the FZ, which gradually decreased while moving towards the BM. On the other hand, the HAZ microstructure of the Ti-6Al-4V welds consisted of a small amount of acicular α`, primary α and β grains near the BM, and a large amount of acicular α` near the FZ.

The maximum hardness values across the welds were in the weld center, and decreased steeply while advancing towards the BM. The hardness across the Nd:YAG laser welds was higher than that across the fiber welds, and was significantly higher across the Ti-6Al-4V welds than that across the CP-Ti welds. The maximum hardness across the welds was generally associated with the lowest heat input.

For the CP-Ti welds joined by the fiber and Nd:YAG laser methods, the maximum tensile strength values were 790MPa and 850MPa respectively, while for the Ti-6Al-4V alloy welds were 1639MPa and 1695MPa respectively. The most noticeable defects observed in laser welds were the incomplete penetration and a few of porosity mainly related to the lowest heat input, in addition to deep craters associated with the highest heat input. There were no indications of cracks across all laser welds. Finally, the fracture behavior of all laser welds was brittle, except the welds that showed the highest tensile strengths, where the fracture mode was a brittle-ductile.

CONTENTS

Abbreviations and Symbols

Abbreviations and symbols	Description
Ti	Titanium
LBW	Laser Beam Welding
EBW	Electron Beam Welding
BCC	Body-Centered Cubic
HCP	Hexagonal Close-Packed
CP-Ti	Commercially pure titanium
FZ	Fusion Zone
WZ	Weld Zone
HAZ	Heat Affected Zone
BM	Base Metal
Nd:YAG	Neodymium-doped Yttrium Aluminum Garnet
SEM	Scanning Electron Microscopy
P/M	Powder Metallurgy
XRD	X-ray diffraction
α	Alpha Phase
UTS	Ultimate tensile strength
β	Beta Phase
Beta-Transus	The temperature of transition from alpha phase to beta phase in titanium and its alloys
α'	The hexagonal martensite phase
α''	The orthorhombic martensite
ELI	Extra low interstitials

LSA	Laser Supported Absorption
H	The ratio between laser power absorbed by the workpiece and incident power
CW	Continuous Wave
TIG	Tungsten Inert Gas
G	Thermal gradient
R	Growth rate
YS	Yield strength
OM	Optical microscopy
FESEM	Field emission scanning electron microscopy
EDS	Energy-dispersive spectroscopy
SGBs	Solidification grain boundary secondary
CNC	Computerized numerical control
R	Remainder
ASTM	American Society for Testing and Materials
W-EDM	Wire electro-discharge machining

List of Figure

List of Tables

Chapter One

Introduction and the Aims of the Research

CHAPTER ONE: INTRODUCTION

1.1 Introduction

Titanium (Ti) and its alloys are considered important engineering materials for industrial applications. The most important properties of Ti and Ti alloys, which make these materials very attractive in various applications, are the high strength-to-weight ratio, corrosion resistance at room and elevated temperatures and mechanical properties that do not deteriorate even at higher temperatures. Ti and its alloys are therefore used in several industrial fields, including aerospace, shipbuilding, food industries, petrochemicals and medical fields [1].

There are however, some alloying elements added to Ti alloys such as aluminum, vanadium, molybdenum, manganese and others to enhance specific properties such as workability, strength and hardness. These elements are called “the stabilizer elements”, and they are two types, the first stabilizes the alpha phase (α), and the second stabilizes the beta phase (β) [2].

Ti also has the characteristic of allotropic transformation at 882.5 °C, where it changes from α to β phase, and from Hexagonal close-packed (HCP) to Body-Centered Cubic (BCC) crystal structure. The transition temperature is affected by the chemical composition of the alloy, where some elements which are stabilizers to the β phase, reduce the transition temperature, and some that act as α-phase stabilizers, increase the degree of transformation [3].

Ti alloys are usually classified as α, α+β and β alloys, with further subdivision into near-α and metastable β alloys, depending on the stabilizing elements [4]. Commercially pure titanium (CP-Ti) alloys have a Ti content of about 98 to 99.5% at least. They are used for thier excellent

resistance to corrosion, especially in applications where high durability is not required. The yield strength of these alloys varies with the content of alloying elements from 170 to 485MPa. The most important of these impurities are iron and oxygen. When the alloy is of high purity, the strength and stiffness are lower. The microstructure of the CP-Ti at room temperature is 100% of the α-crystalline structure with a small content of impurities, but when the content of stabilizing elements increases, a β-phase appears on the grain boundaries of the α-grains [5]. CP-Ti has established a reputation for low density, high corrosion resistance and excellent biocompatibility for dental prosthetic applications including crown and bridge, partial framework and dental implant [6].

The Ti-6Al-4V alloy is the most important of the (α+β) alloys, and the amount of β phase stabilizers is more than that of near α alloys. It is also a heat treatable alloy for improving strengthening and mechanical properties. One of its most important applications is the manufacture of aircraft bodies, in addition to propellers and compressor blades in gas turbine engines and other applications [7].

Ti alloys are easily weldable and less sensitive to cracking [8], but due to the high affinity for reaction with some atmospheric constituents, embrittlement may occur from contamination if the weld metal is not adequately protected. Thus, these defects cause danger to the welded parts. These defects often arise when the energy density is not high enough for the welding process, or due to residual stresses [9]. Because of its high melting point, and its ability to react with the elements in the medium at high temperatures, it is preferable to use laser welding compared to traditional methods [10].

Nowadays, laser beam welding (LBW) is widely used to minimize the drawbacks of normal fusion welding processes. The welding speed is higher, and the weld pool of the LBW is much smaller than that of the arc

welding due to the small focusing diameter used. In addition, LBW has higher aspect ratio and higher welding efficiency [11]. The geometry of the welds mainly depends on the welding parameters, which affect the penetration depth and the width of the fusion zone (FZ) and heat affected zone (HAZ) [12]. When welding CP-Ti by the laser welding process, the microstructure of the FZ has a columnar (α) phase, while the HAZ is composed of a mixture of columnar α and α phase [13]. On the other hand, the FZ in the Ti-6Al-4V alloy however consists of ά martensite. The HAZ microstructure typically composed of primary α, acicular α, and acicular ά due to the increase of β stabilizer elements [14].

There are various laser welding systems used in industries. Each type has different characteristics that mainly depend on the active medium used to generate the laser [15]. Among the most important of these types are the CO_2, Nd:YAG and fiber lasers. The fast developments in laser technology have contributed to reducing cost and weight and, on the other hand, improving welding quality [16].

1.2 The Aims of the Research

Nowadays, Ti alloys are gaining great importance in industrial applications, and laser offers a promising process for welding these alloys. This work aims to conduct a comparative study on the effect of using efficient and diverse laser welding methods, and the most effective parameters of these methods on the industrially common Ti alloy welds. The study includes investigating the influence of laser power and welding speed on the microstructure and mechanical properties (tensile strength and hardness) of the continuous fiber and pulsed Nd:YAG Ti alloy laser welds. The research also aims to laser weld both the commercially pure titanium CP-Ti (grade 2) and Ti-6Al-4V (grade 5) alloys, and to introduce

outstanding weld joint efficiencies. Another objective of this work is to analyze the effect of laser welding parameters on weld geometry, penetration and potentially defects, using several examinations.

1.3 Outline of the Thesis

The thesis consists of five chapters. The introduction to the research, which includes a background on Ti alloys, the laser welding methods used, and the research objectives, was presented in the first chapter. The second chapter includes the theoretical part and literature background related to laser welding of Ti alloys. The details of various experimental procedures related to laser welding, microstructure analysis, hardness, tensile testing, XRD, etc. are discussed in chapter three. The fourth chapter includes the results obtained from practical experiments with their detailed discussion. The fifth chapter includes the conclusions obtained from this work. The references section contains all the references mentioned in the thesis.

Chapter Two

Theoretical Part and Literature Review

CHAPTER TWO: THEORETICAL PART AND LITERATURE REVIEW

2.1 Titanium and Its Alloys

Recently, Ti has become a very important technical material whether in form of a technically pure metal or an alloy. Ti has been discovered in 1791by Englishman W. Gregor. In nature, it is the tenth most common element, but its use is limited primarily due to its high affinity to atmospheric contamination. Despite being very chemically reactive, it exhibits great resistance to corrosion because (similar to aluminum) it covers itself with an oxide coating (TiO_2) [17].

Ti and its alloys have also low specific weight, high strength, attractive fracture behavior and relatively high melting point [18]. Figure (2.1) shows the density of several metals.

Weldability of CP-Ti and most Ti alloys is good in general, although specific cares must be taken during the welding process because pure titanium and its alloys are highly susceptible to contamination from atmospheric gases [19, 20]. They react during welding with atmospheric oxygen forming TiO_2. The oxide layer, however, prevents the surface from more oxidation. At 550 °C, Ti also combines with chlorine, halogens and hydrogen. Ti reacts with nitrogen at 800 °C to form TiN, which causes embrittlement and thus loses ductility. Hence, vacuum or inert atmosphere is suitable for processing of Ti [21]. When the shielding is insufficient, the heated Ti surface absorbs gases from atmosphere and finally Ti forms brittle carbides, nitrides and oxides causing hardness increasing and simultaneously reducing the fatigue strength and notch toughness of the welded joint and HAZ. The groove of the weld joint also must be perfectly protected by shielding gas. Additionally, any surface impurities can diffuse into the molten Ti, causing porosity and brittleness, thus, the joint area

must be reduced and cleaned precisely. The content of carbon in the pure titanium should not exceed 0.1%, but even very low content of carbon may result in formation of Ti carbides, which have hardness up to 900 HV. Additionally, in a case of low content of oxygen, the carbon oxide and/or carbon dioxide may be formed causing weld porosity [22].

The electrical and thermal conductivity of Ti is relatively low, and significantly affects the thermal cycle of welding, thus the cooling rate of the FZ and HAZ is relatively low too. The low cooling rates usually lead to grain growth of weld metal and HAZ as well [19]. Hard martensitic microstructures can form under rapid cooling conditions, often requiring post weld heat treatments. However, the martensite formed in Ti alloys has less hardness compared to that associated with steels [23].

Ti and its alloys are produced in a wide variety of product forms shown in Figure (2.2). Ti that can be wrought, cast, or made by powder metallurgy techniques (P/M) may be joined by means of fusion welding, brazing, adhesives, diffusion bonding, or fasteners. Ti and its alloys are formable and readily machineable, assuming reasonable care is taken[7].

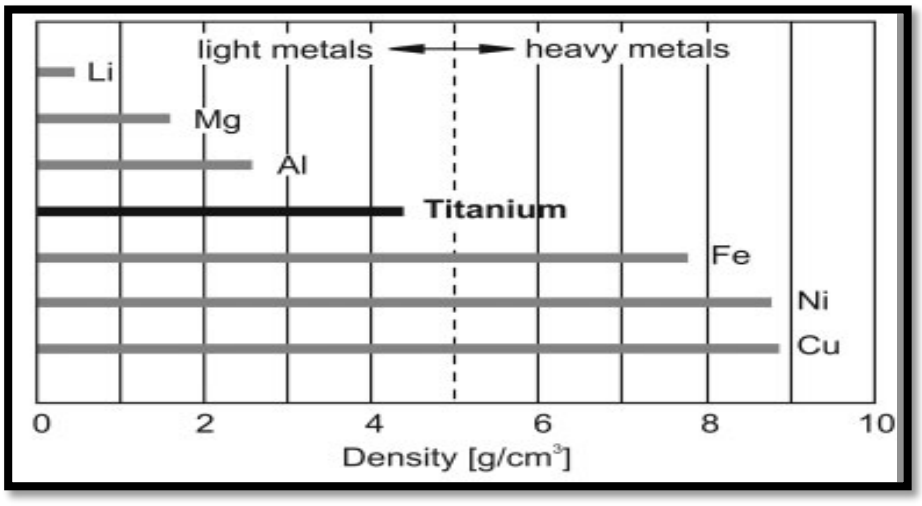

Figure (2.1): Density of some metals [7].

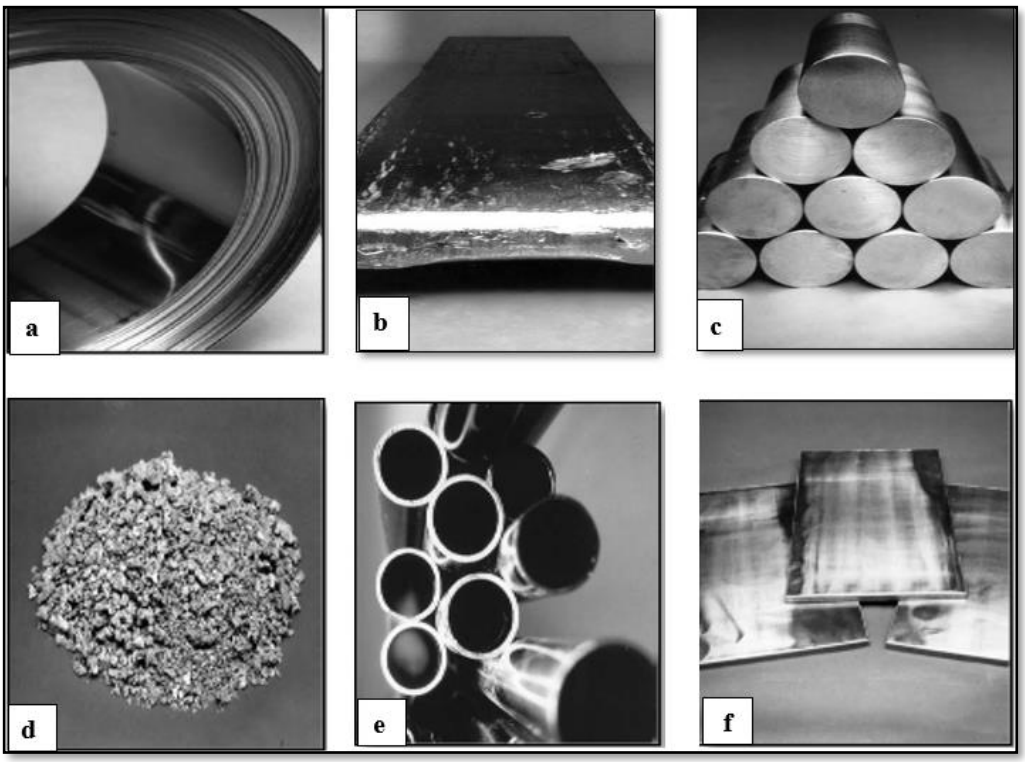

Figure (2.2): Some forms of Ti and Ti alloy products: (a) strip, (b) slab, (c) billet, (d) sponge, (e) tube and (f) plate [24].

2.2 Influence of Elements on Properties of Titanium Alloys

In relation to the existence of allotropic change (882°C) of α into β, the additives in Ti alloys are classified based on whether they increase or decrease the temperature of this transformation, i.e. which of the two given phases stabilizes in larger temperature range. This influence is closely related to their higher solubility in phases. Impurities are especially interstitial elements, such as oxygen, nitrogen, carbon and hydrogen, which form interstitial solid solutions (O, N and C are α- stabilizers, H is a β-stabilizer) or brittle oxides, carbides, nitrides or hydrides. These additives lower the degree of plasticity properties, worsen weldability and increase the corrosion susceptibility. On the other hand, they increase strength and hardness [17].

2.3 Physical Metallurgy of Titanium

Ti is an allotropic element, which means that it can exist in more than one crystallographic form. At room temperature, pure titanium has an HCP crystal structure, which is referred to as α phase. When temperature exceeds 882°C, Ti transforms to a BCC crystal structure, called β phase as shown in Figure (2.3). The temperature transition from α to β phase is called β-transus, which dependent on the alloying elements. The β to α transformation is very important due to its influence on the microstructure formed in Ti alloys. The phase transformation from the high temperature β phase to the low temperature α phase depends on the cooling rate, so that the phase transformation can either be diffusion-less (martensitic) or diffusion controlled. Both of these transformations occur during welding of Ti alloys [25]**.** The α stabilizing elements, such as Al, C, O, N can increase the α - β transformation temperature and stabilize the α phase at higher temperatures. On the other hand, β stabilizing elements, such as Mo, V, Ta, Fe, Mn, Cr, Co, Ni, Cu, Si and H shift the field to lower temperatures by reducing the β-α transformation temperature. Neutral elements, such as Sn, Zr have however very small influence on the β transus temperature. Due to the different usage of alloying elements and the fabrication process, Ti alloys can form as a combination of various amounts and arrangement of α and β phases. According to the amount of the two phases, Ti alloys can be classified as α, near α, α+β, β and metastable alloys [26]. Two specific cases of phase arrangement namely lamellar microstructure and equiaxed microstructure exist. Normally, the lamellar microstructure is generated upon cooling from the α phase field, while the equiaxed microstructure is a result of the recrystallization process. Both types of microstructure can have fine and coarse arrangements of the two phases [4].

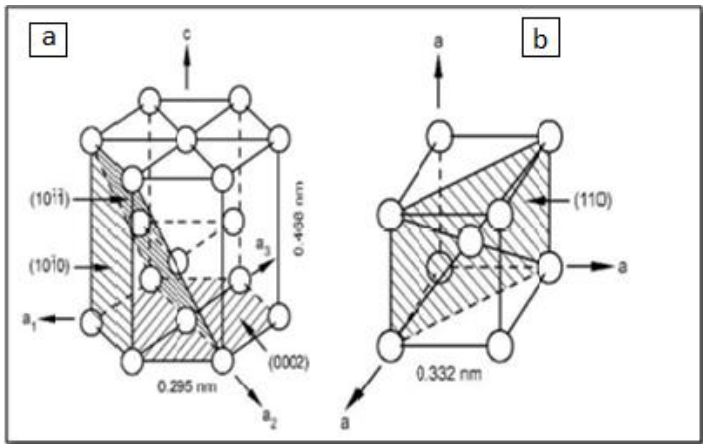

Figure (2.3): Structure modification of Ti with slip systems and lattice parameters in (a) HCP and (b) BCC lattice [25].

In what follows the common thermomechanical process of Ti-based alloys and microstructures evolution are detailed. Afterwards, microstructure evolution in three important Ti-based alloys, Ti6Al4V, Ti6246 and Ti834, which have been widely used for compressor manufacturing in aerospace engines are discussed. Microstructures in Ti-based alloys are highly dependent on the thermomechanical treatment including deformation, solution heat treatment, recrystallization, aging and annealing. A commonly used thermomechanical treatment is outlined in Figure (2.4). By combining complex sequenced processes, various microstructure morphologies can be formed in Ti-based alloys [26].

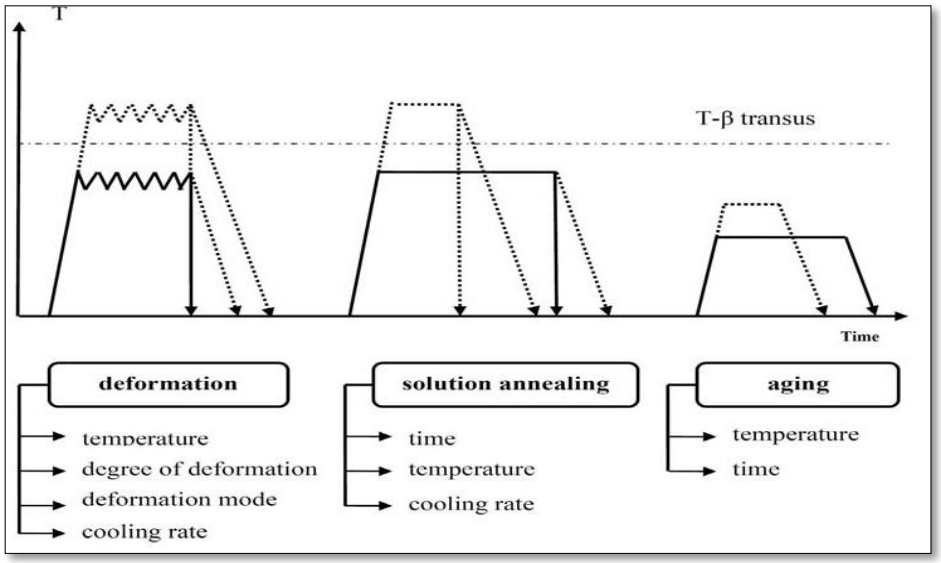

Figure (2.4): Thermomechanical treatment of Ti alloys [17].

2.3.1 Phase Diagrams

Alloying elements in Ti alloys are classified into α or β stabilizers based on their effects on the α/β transformation temperature or on their differing solubilities in the α or β phases. The substitutional element (Al) and the interstitial elements (O, N and C) are strong α stabilizers, which increase the transus temperature as shown in the schematic phase diagrams in Figure (2.5a). On the other hand, the β-stabilizing elements lower the transus temperature. Those are distinguished into β-isomorphous types (e.g. V, Mo, Nb and Ta) and β-eutectoid types (e.g. Mn, Fe, Cr, Co, Ni. Cn, Si and H) [27]. TTT diagram of the Ti alloys are also shown in Figure (2.5b).

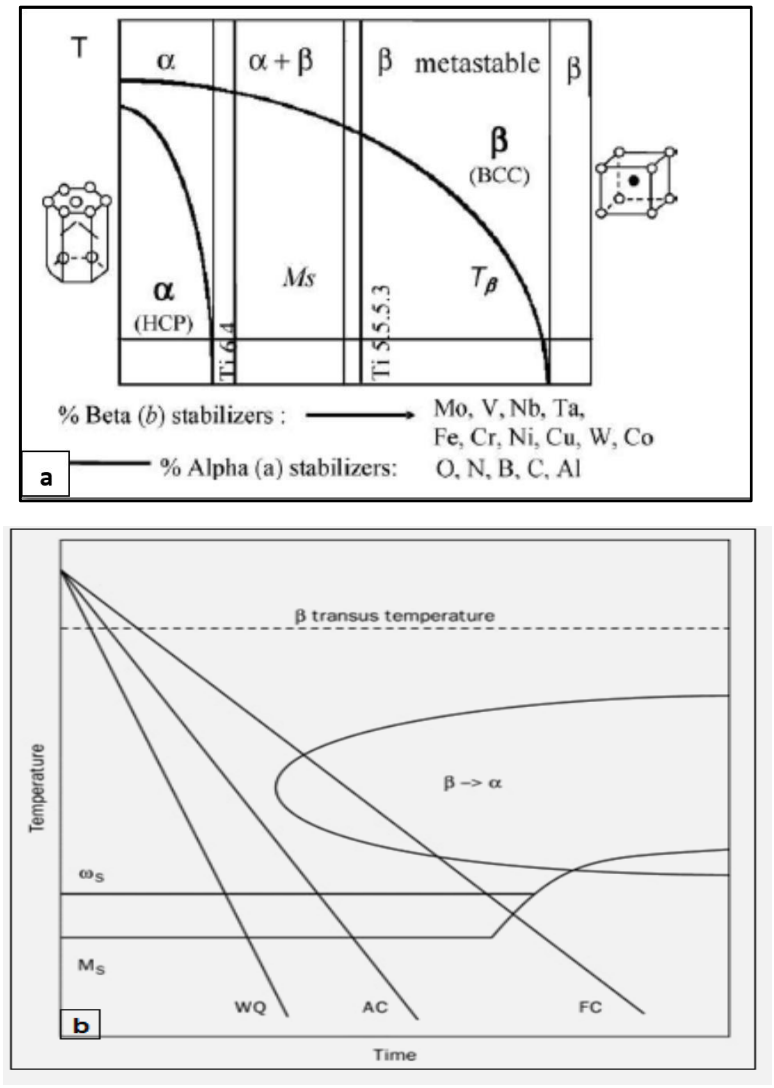

Figure (2.5): (a) phase diagram of Ti alloys, (b) TTT diagrams of Ti alloys [30, 31, 34].

2.3.2 Martensitic Transformations

This process involves a cooperative movement of atoms, resulting in a microscopically homogeneous tranformation of the BCC into the HCP crystal lattice. Quenching of the BCC β phase of pure Ti and dilute Ti-alloys can result essentially in two different crystal structures of martensites: the hexagonal martensite which is designated (α'), and the orthorhombic martensite which is designated (α''). The most prevalent type is α', which can occur in two limiting morphologies: massive or lath martensite (high purity Ti and very dilute alloys) and "acicular" martensite in alloys with slightly higher solute contents. The acicular martensite α' occurs as an intimate mixture of individual plates, each having a different variant of the Burgers relation. The orthorhombic martensite α'' seems to occur mainly in Ti-alloys with β stabilizers of the transition metals Mo, Nb, Ta, W, Re and in Ti-alloys with Al and V. The compositional boundaries α'/α'' differ from alloy to another. The lattice parameters of α'' are strongly dependent on solute content, and the α'' crystal structure is sometimes conveniently viewed as a distorted hexagonal structure [28, 29]. Ti martensite (α' phase) strengthens alloys to a lesser extent than martensite in steels. Ti martensite of the (α'') type generally has no effect on the strength of the alloys (i.e., the strength is no higher than that of the original β phase). Nevertheless, considerable strengthening of Ti alloys due to the formation of α' martensite occur [29].

2.4 Mechanical Properties of Titanium Alloys

Titanium and its alloys exhibit a unique combination of mechanical and physical properties and corrosion resistance, which have made them desirable for critical demanding in aerospace, chemical and energy industry services. Titanium’s elevated strength-to-density represents the traditional

primary incentive for selection and design into aerospace engines and airframe structures. Its exceptional corrosion/erosion resistance provides the prime motivation for chemical process and marine industrial use. Ti alloys also offer attractive elevated temperature properties for application in hot gas turbine and auto engine components, where more creep resistant alloys can be selected for temperatures as high as 600°C [5, 32].

2.5 Corrosion Properties of Titanium and Its Alloys

Unalloyed Ti is very resistant to corrosion in various environments: seawater, body fluids, and vegetable and fruit juices, salt solutions of chlorides, sulfides, sulphates, HNO_3 solution, and wet chlorine. Ti has a limited resistance to oxidation above 540°C in air. Alloys depending on the composition and surrounding environments may be affected by galvanic corrosion (generated galvanic cells), crevice corrosion (hot solutions of chlorides, iodides, bromides and sulphates), erosion-corrosion and cavitation, stress-corrosion cracking [1,32,33].

2.6 Titanium Alloy Classification

The two crystal structures of Ti are commonly known as α and β. α actually refers to any HCP titanium, pure or alloyed, while β denotes any BCC titanium, pure or alloyed. The alpha and beta structures (sometimes called systems or types) are the basis for the generally accepted five classes of Ti alloys: alpha, near-alpha, alpha-beta, and beta. Figure (2.6) schematically shows some effects of alloying elements on structure for representative alloys and classes or subclasses of titanium alloys [6, 34].

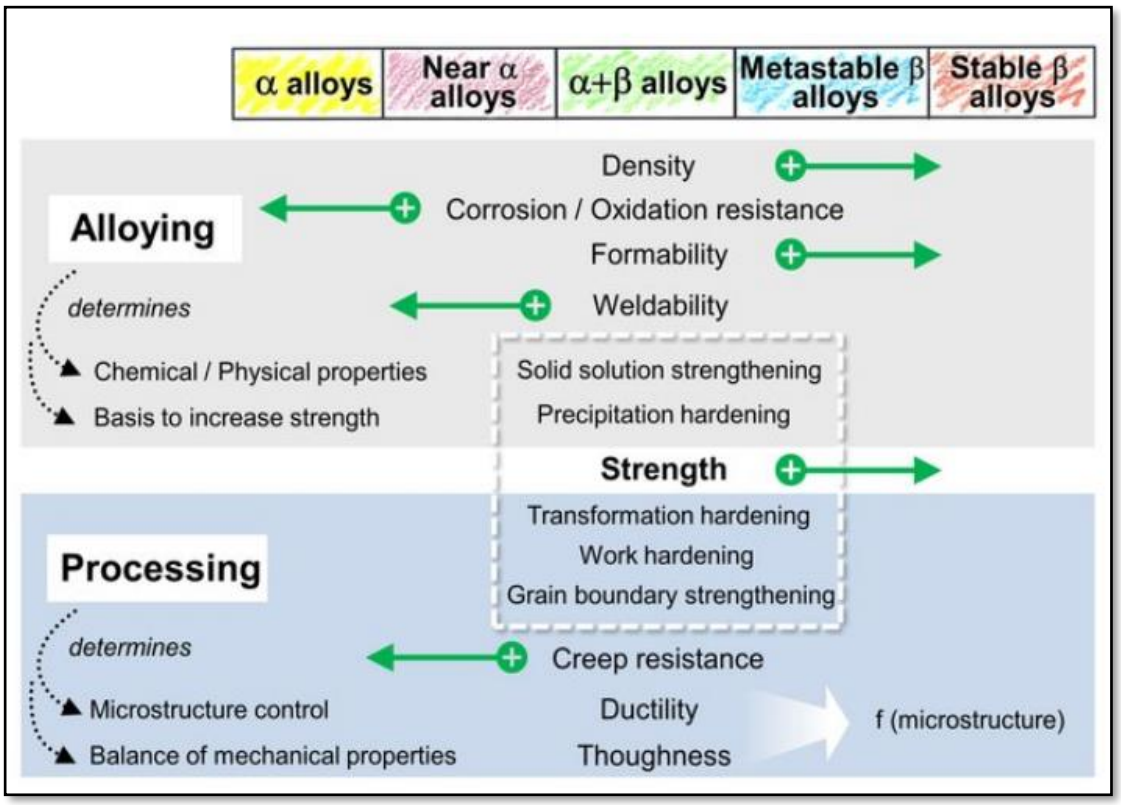

Figure (2.6): Effects of alloying elements on structure and some properties [34].

2.6.1 Unalloyed Commercially Pure Titanium and Alpha Alloys

The group of alloys called α alloys in Table (2.1) consists of the most grades of CP-Ti and α alloys which upon annealing well below the β transus contain only small amounts of β phase (2-5vol.%) stabilized by iron. The β phase is helpful in controlling the recrystallized α grain size and improves the hydrogen tolerance of these alloys. The four different grades of CP-Ti differ with respect to their oxygen content from 0.18% (grade 1) to 0.40% (grade 4) in order to increase the yield stress level. The two alloys Ti-0.2Pd and Ti-0.3Mo-0.8Ni offer better corrosion resistance than CP-Ti. Their common names are grade 7 and grade 12, respectively, and the iron and oxygen limits are identical to grade 2 of CP-Ti. Ti-0.2Pd is however more expensive than Ti-0.3Mo-0.8Ni. The (α) alloy Ti-5Al-2.5Sn (0.20% oxygen) has a much higher yield stress level (780-820 MPa) than the CP-Ti grades (grade 4: 480 MPa). It can be used at service temperatures up to

480°C and in its ELI (extra low interstitials) version with 0.12% oxygen also at low temperatures (–250°C). It is an old alloy, first manufactured in 1950, but still on the market, although it is being replaced by Ti-6Al-4V in many applications [35].

Table (2.1) Some Ti alloys and it properties [7,17].

Alloy Composition (ASTM Grade)	General description and typical use
Grade1(CP-Ti)	Ti is the highest ductility, cold formability, and impact toughness, with excellent resistance to mildly reducing to highly oxidizing media with or without chlorides and high weldability
Grade2 (CP-Ti)	For anticorrosive protection in chemical and maritime industries and good weldability. Some applications are Aircraft ducting, hydraulic, tubing, misc., Air pollution control equipment, Architectural, roofing, Consumer products (watches, eyeglass frames, etc.)
Grade 5(Ti-6Al-4V)	This titanium alloy is a versatile medium-strength titanium alloy that exhibits good tensile properties at room temperature, creeps resistance up to 325°C, and excellent fatigue strength. It is often used in less critical applications up to 400°C. It is the alloy most commonly used in wrought and cast forms. Turbines discs and blades, parts of airframe structures. Implants, prosthesis
Ti-3Al-8V-6Cr-4Zr-4Mo (Beta C alloy)	Equiaxed beta grain structure with fine alpha precipitates within the matrix. Good ductility, high strength. Applications: Fasteners, springs, torsion bars, foil, tubular and casings in oil, gas, and geothermal wells.

2.6.2 Alpha/Beta Alloys

These alloys contain larger amounts of β stabilizers (4 to 6%). α/β alloys can be heat-treated to develop a variety of microstructures and mechanical propertys [36]. Ti-6Al-4V (Ti64) alloy is one of the most important Ti alloys. It accounts for about 45% of the total weight of all Ti alloys produced, and more than 80% of Ti alloys used in fan and compressor sections, where temperatures do not exceed ~350°C [25]. Ti-

6Al-4 V is also used in the aerospace industry, medical implants and in automotive, marine and chemical industries. It is an α+β alloy, which combines attractive mechanical properties with good workability and the best weldability. Ti-6Al-4V has a relatively low hardenability and the α` martensite in this alloy is not as hard and brittle as in more heavily β-stabilized alloys. The microstructure can be varied by varying the solution and aging temperatures and times as well as cooling rates from above the β transus [36]. Air cooling results in a needle-like α-phase (acicular α). Different varieties of phase morphologies form depending on the temperature history of the Ti-6Al-4V alloy. Intermediate cooling develops Widmanstätten microstructures, quenching from temperatures greater than 900 °C results in a needle-like (HCP) martensite α', while quenching from 750-900 °C produces an orthorhombic martensite α" [37, 38]. Three basic and typical microstructures are shown in Figure (2.7).

2.6.3 Metastable Beta-Alloys

The β-phase is stable at room temperature with appropriate alloying elements called β-stabilizers, which lower the β-transus temperature such as Nb, Ta, Mo, V, and Cr. Alloys that have a high volume fraction of β-phase are β alloys. Examples of β-alloys are the binary alloys Ti-Mo and Ti-Nb, or the quaternaries Ti-13V-11Cr-3Al and Ti-11.5Mo-6Zr-4.5Sn. The elements V, Mo and Nb are commonly chosen as β-stabilizers because they lower the β-transus temperature and do not readily promote the formation of metastable phases in titanium alloys. These alloys possess the distinctive properties of fatigue resistance, strength and toughness in wide sections, thus being the most versatile Ti alloy [39].

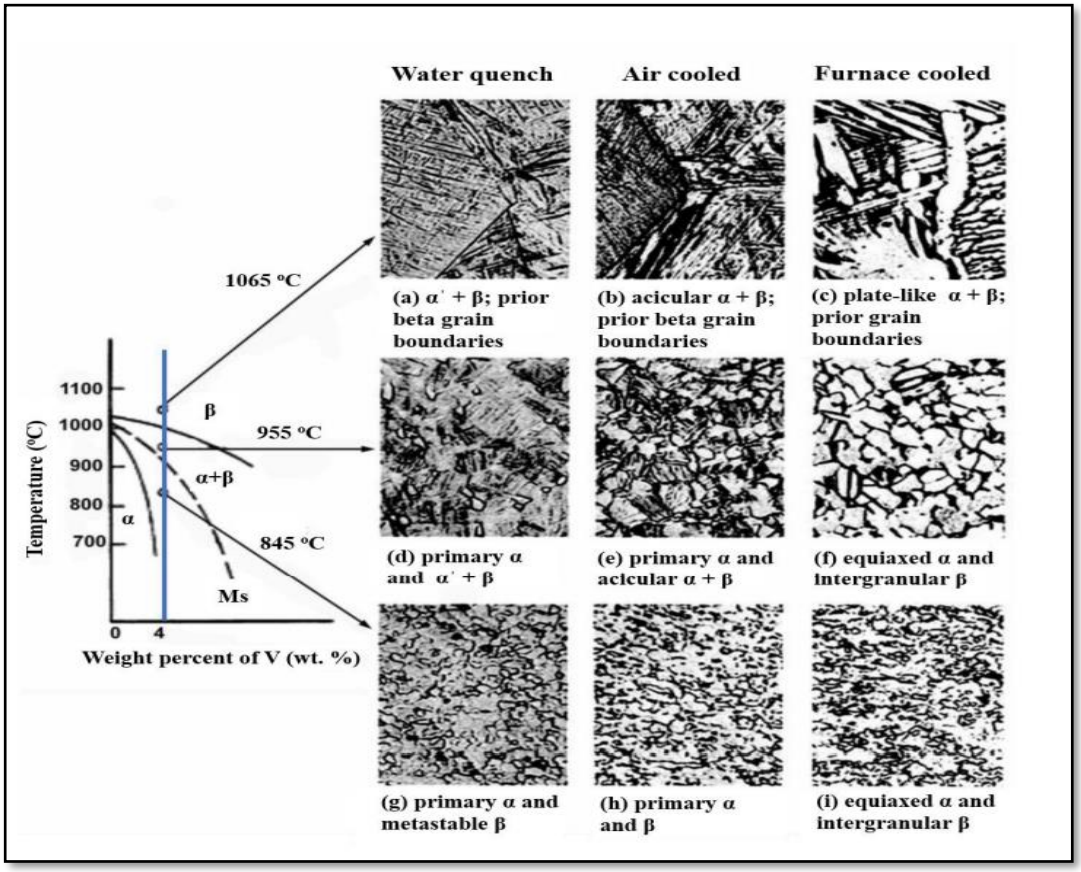

Figure (2.7): The microstructure of Ti-6Al-4V for different cooling processes [39].

2.6.4 Beta Alloys

Very large addition (30%) of β stabilizers results in retaining β as a stable phase at room temperature. β alloys resemble refractory metals in their high densities and poor ductility and are used for highly specialized burn-resistance and corrosion-resistance applications [38].

Figure (2.8) illustrates some of the microstructure of the Ti alloys.

2.8 Application of Titanium Alloys

Titanium and its alloys are used in many different fields such as erospace, automotive, sporting equipment, chemical, marine and medicine due to their excellent high strength-to-weight ratio, good creep resistance, excellent corrosion resistance and good biocompatibility [41,42]. Figure (2.9) outlines some applications of Ti alloys.

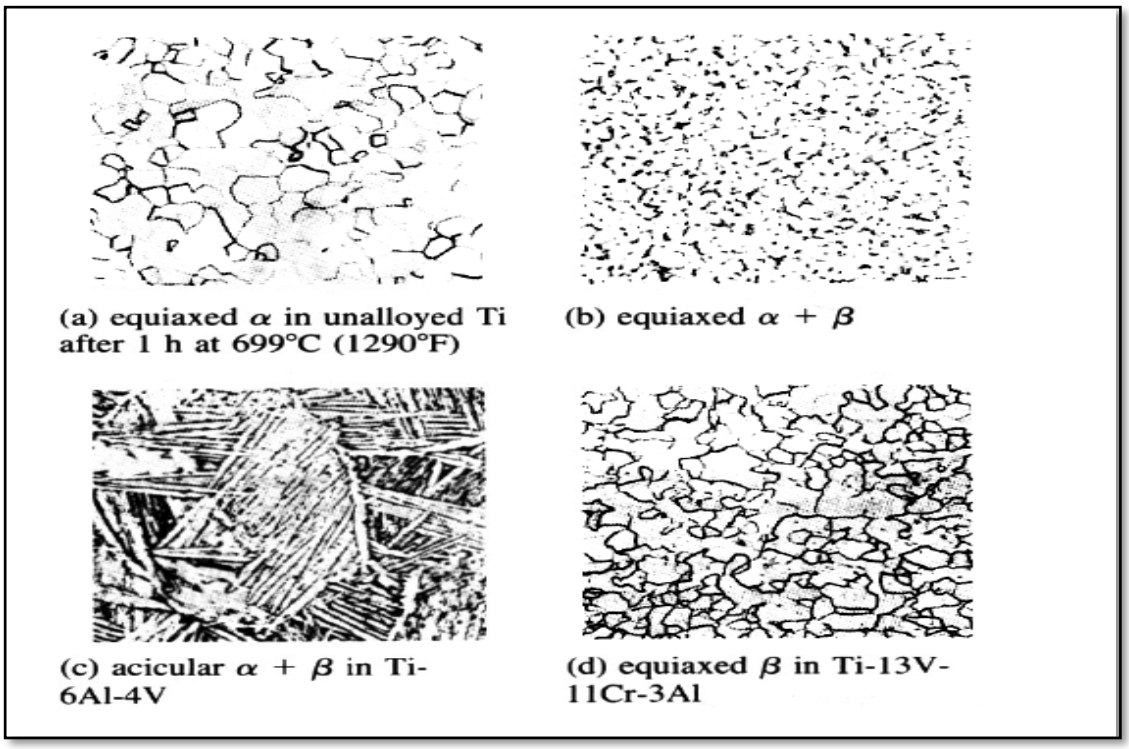

Figure (2.8): Typical microstructures of α, α+β, and β Ti alloys [41].

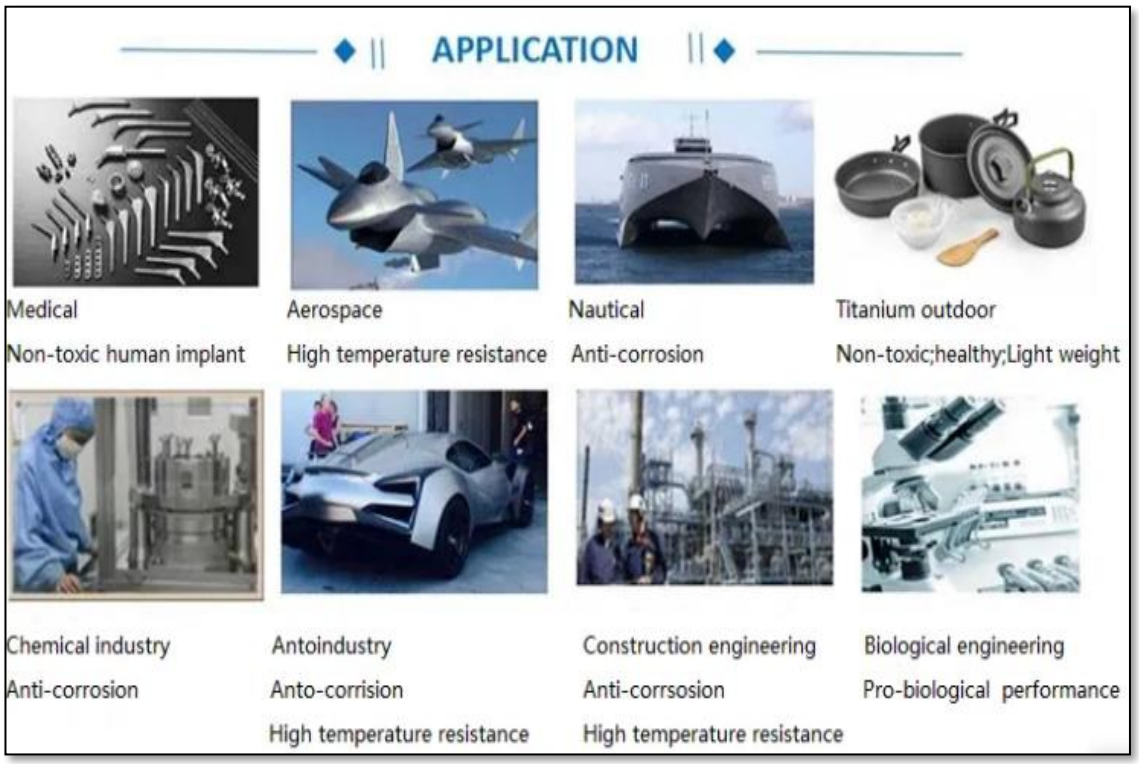

Figure (2.9): General characteristics and typical applications of Ti alloys [43].

2.9 Weldability of Titanium and Its Alloys

Most Ti alloys have excellent weldabilty in the annealed condition, and relatively limited weldability in the solution treated and aged conditions. In general, CP-Ti, α-Ti and α/β Ti alloys have better weldability compared with metastable β Ti alloys. These facts imply the effects of composition of the material and their conditions. Aside from the materials, welding methods may have different influences on the weldability of Ti and its alloys [42].

Ti alloys are characterized by high melting point, and high affinity for interaction with oxygen at high temperatures during welding processes. Therefore, they need welding techniques that provide high protection efficiency, high welding efficiency, few distortion and complete penetration. This is what made industrial trends move towards laser welding [13,44].

2.10 Laser Welding Principle

Laser beam welding (LBW) and electron beam welding (EBW) are classified as high-energy density welding processes. One of the characteristics of these two processes is the high aspect ratio (penetration depth to the width of the weld) compared to the conventional arc welding processes. It is well known that the joint penetration depth of LBW is lower than that of EBW at the same power level due to the formation of a laser-induced plume during welding. This plume causes severe attenuation of the incident laser power.

In recent years, various deep penetration techniques for LBW have been developed through the control of the laser-induced plume. LBW is a high energy-density welding technique, and is well known for its high speed, minimum HAZ, fine quality of welds seam, and low heat input per unit

volume. Figure (2.10) shows power density profiles of laser, electron beam, plasma and arc, and the consequent weld bead geometries [22,45]. Laser welding is a thermal process that follows the thermal cycle of heating, melting and vaporizing. The effectiveness of this process depends on thermal properties and to a certain extent, the optical properties, rather than the mechanical properties of the material to be welded. Therefore, materials that exhibit a high degree of brittleness, or hardness, and have favorable thermal properties, such as low thermal diffusivity and conductivity, are particularly well suited for laser welding. Laser welding is a flexible process when combined with a multi-axis workpiece positioning system or robot. The laser beam can be used for executing different welding geometries on a single machine. This flexibility eliminates transportation necessary for processing parts with a set of specialized machines. In addition, laser welding can result in higher precision welded parts than that produced by comparable other techniques [70].

The requirements of knowledge before designing a laser-based process include the selection of lasers, the beam delivery system, the interaction time between the laser beam and the workpiece, and the possible unwanted side effects. In addition, important requirements for lasers, which are used for materials processing, need to concern the sufficient power available at the workpiece, controlled focal intensity profile (well-characterized spatial mode). Repeatability of the laser characteristics such as power, mode, polarization, pointing-stability, reliability, and capital and running costs which are economic for the application are other requirements have also to be concerned [71].

The principle of operation is shown in Figure (2.11). In this technique, a laser beam is directed to a joint, and moved along the joint. The metals will melt and turn into a liquid, fuse with each other and then solidify,

completing the process of joining the two pieces. Laser processing is free of electromagnetic fields and is thus, suitable for welding different couples.

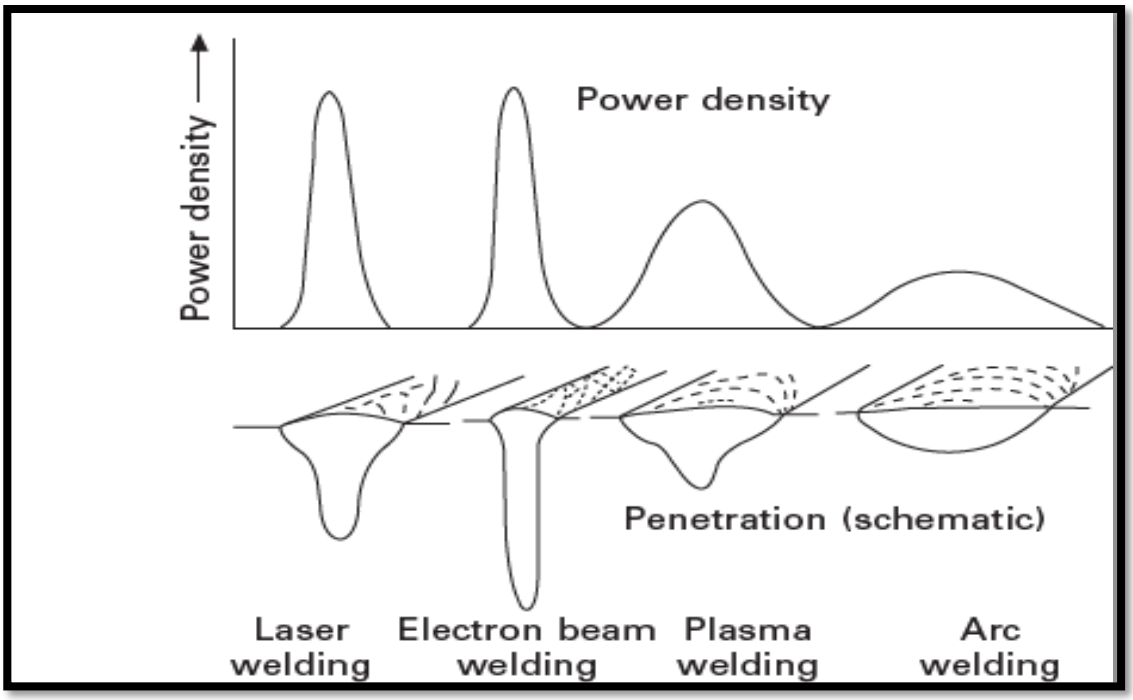

With flexibility in the power intensity, power distribution and scanning velocity, laser welding is emerging as a major joining process.

Figure (2.10): Power densities for typical welding heat sources, and geometry of weld beads obtained at respective densities [49].

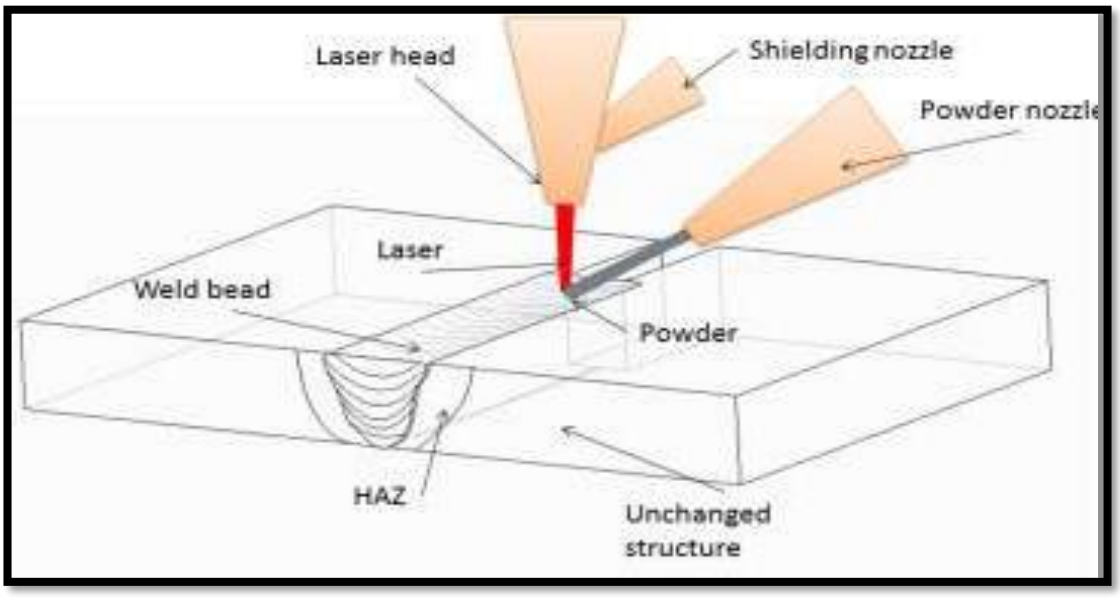

Figure (2.11): Principle of laser welding [50].

The procedures and equipment used for welding CP-Ti and many Ti alloys needs additional precautions to shield the molten weld pool due to their increased reactivity with atmospheric elements [48].

The gas shield used in laser welding is of great importance to prevent the brittleness of the welding zone (WZ), porosity and the resulting losses in ductility. It improves the coupling between the incident beam and the workpiece as well as avoids the formation of oxide on its surface. Several nozzles for laser welding have been developed. The conical nozzle for fixing the used plasma column is designed for good quality welding; the ring nozzle is designed to avoid ambient air pollution. Greater penetration depth is achieved using helium gas than argon due to the lower ionization energy of argon, which reduces energy transfer to the material [50].

2.11 Generation of Laser

Lasers convert electrical energy into a high energy density beam of light through stimulation and amplification. Stimulation (Figure 2.12) occurs when electrons in the lasing medium are excited by an external source such as an electrical arc or flash lamp, resulting in the emission of photons. The energy required to raise an electron from one energy state to another is provided by an excitation process or pumping. This is achieved by the lasing medium's absorption of energy from mechanical, chemical, electrical, or light sources. The lasing medium typically contains ions, atoms or molecules whose electrons cause changes in energy level. According to quantum mechanics, atoms or molecules in the lasing medium have discrete electron energy levels. Laser light is created by the transition from a higher to a lower energy level, and the wavelength produced is a characteristic of the lasing medium. At the beginning of the lasing process, photon emissions are random in nature. Each photon

stimulates other excited electrons to emit photons. However, the new photons will have similar wavelength, direction, and phase characteristics as the initial photon. Eventually, a stream of photons with identical wavelength, direction and phase will be produced [51, 53].

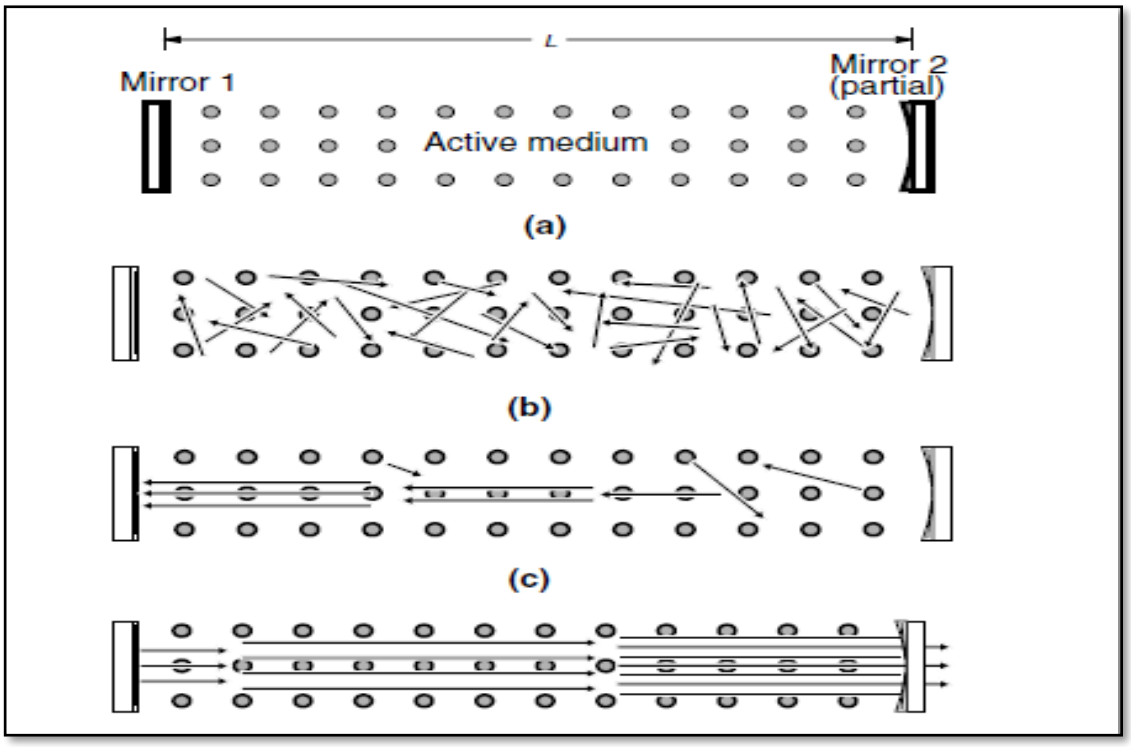

Figure (2.12): Illustration of laser amplification [53].

The laser beam exiting from the laser source may be 1-10mm in diameter, when focused on a spot has energy density of more than 10kW/mm^2.

Laser beam welding is a thermoelectric process accomplished by material melting and evaporation [45]. As the metal atoms evaporate and leave the surface of the molten metal, forces in the opposite direction of evaporation create a significant localized vapor pressure. This pressure depresses the molten metal surface creating a hole, which is known as a keyhole. The weld metal solidifies behind the keyhole as it progresses along the joint. This method of welding produces high depth-to-width ratio welds, and is the most common approach when using either LBW or EBW [23].

2.12 Laser Material Interactions

The important physical phenomena that occur during the interaction of high power laser radiation with surfaces are sketched in figure (2-13). The top left portion of the figure indicates the absorption of the incident laser light according to Beer Lambert's law (in the red rectangular), where Ix: the intensity, I_o: the initial intensity, α: the coefficient of absorption and x: the depth in meters.

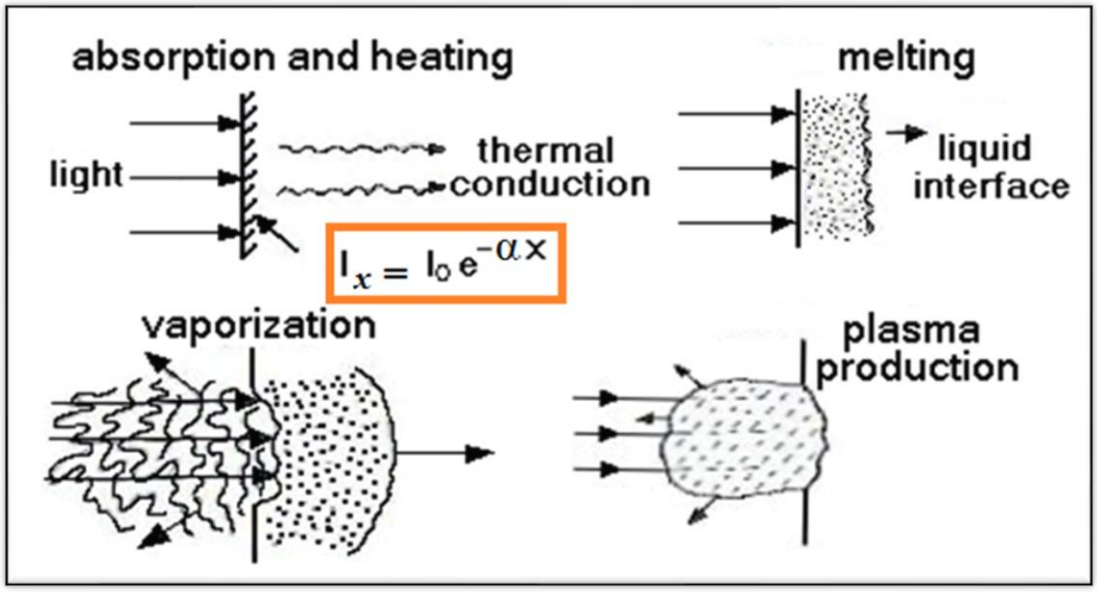

Figure (2-13): Physical phenomena occurring when a high power laser strikes an absorbing surface [53].

With the neglecting the fraction of the light that is reflected, the heat energy then penetrates into the target by thermal conduction. When the surface reaches the melting temperature, a liquid interface propagates into the material, as indicated at the right portion of Figure (2-13). With continued irradiation, the material begins to vaporize, as indicated in the button left portion, and a hole begins to be drilled. If the irradiance is high enough, absorption in the blow off material leads to hot opaque plasma. The shielding of target by hot opaque plasma leads to a phenomenon called a laser supported absorption (LSA) wave. The LSA wave is plasma that is generated above the target surface and propagates along the beam path

toward the laser; it is accompanied by a loud noise and a bright flash of light. Plasma can grow back toward the laser as an (LSA) wave, it absorbs the light and shields the surface and reduce the material removal as shown in the bottom right portion of the Figure (2-13). Absorption of laser energy can also produce large pressure pulses in the target. One mechanism by which pressure pulses are produced involves evaporation of material from the surface, with recoil of the surface in response to the momentum of the vaporized material. Larger pressure pulses are developed when the LSA wave is kindled. The hot plasma, as it expands, can drive a shock wave into the target [54].

2.13 Effect the Plasma in Laser Welding

Laser welding is accompanied by the phenomenon of the formation of the plasma plume, as shown in Figure (2.14). The plasma consists of the ionization of the surrounding covering gases and the plume consists of the interaction of laser rays with metal vapor resulting from heating the metal with a laser to a temperature higher than the melting point. The plasma formed on the surface of the workpiece is called (the plasma column) and inside the keyhole is called (keyhole plasma). The presence of plasma causes reflections, scattering and absorption of laser energy, which affects the penetration of welding [55]. In the case of using helium gas to cover, laser welding will be accompanied by the formation of metal plasma only because helium has high ionization energy. As for the use of nitrogen and argon gases, metal plasmas called metallic plasmas and the resulting plasma will be formed from the covering gases [49,56]. In the case of CO_2 laser welding, the effect of plasma formation is large on the depth of the weld when using the argon and nitrogen covering gases, due to its absorption of the energy of the laser beam, but in Nd:YAG and fiber laser welding, its effect is less [57,58].

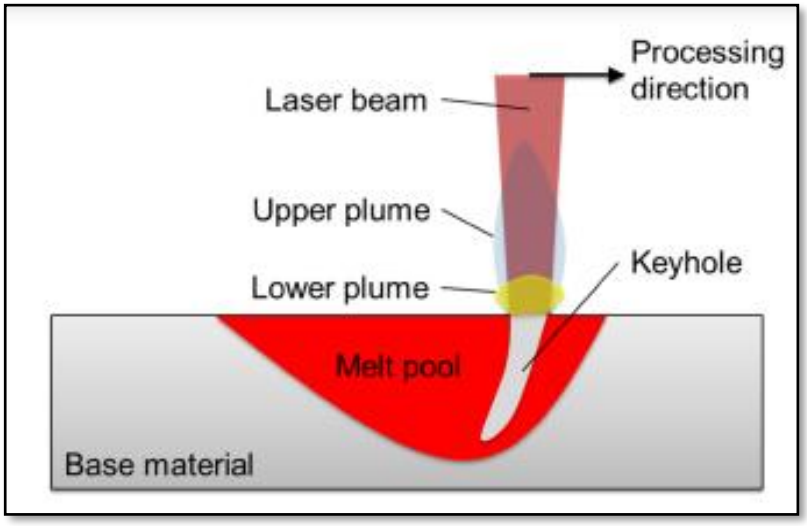

Figure (2.14): The plasma plume formation in laser welding [57].

2.13 Laser Welding Mechanisms

Materials are joined by melting during the fusion laser welding process. Two mechanisms can be used to perform the laser welding: [59].

- Conduction Limited mode.
- Keyhole Mode.

Conduction mode welding creates a semi-circular weld cross-section through absorption of the continuous laser beam by the material's surface, and thermal conduction heating the material under the surface. Thick materials cannot be joined with this technique. Larger heat generation is required due to the considerable thickness, which results in a larger weld zone (WZ) and significant distortion [59, 60], as shown in Figure (2.15a). Conduction welding is a reliable, low-energy method that can be carried out with a laser that doesn't require a high-quality beam. Therefore, a cheap, low-power laser can be employed. The characteristics of weldable materials are comparatively unimportant as long as fusion is possible; for example, their hardness has little influence on the process and they are not required to transmit electricity. Materials of wires, strips, thin sheets, or a combination of these in a variety of shapes can be connected.

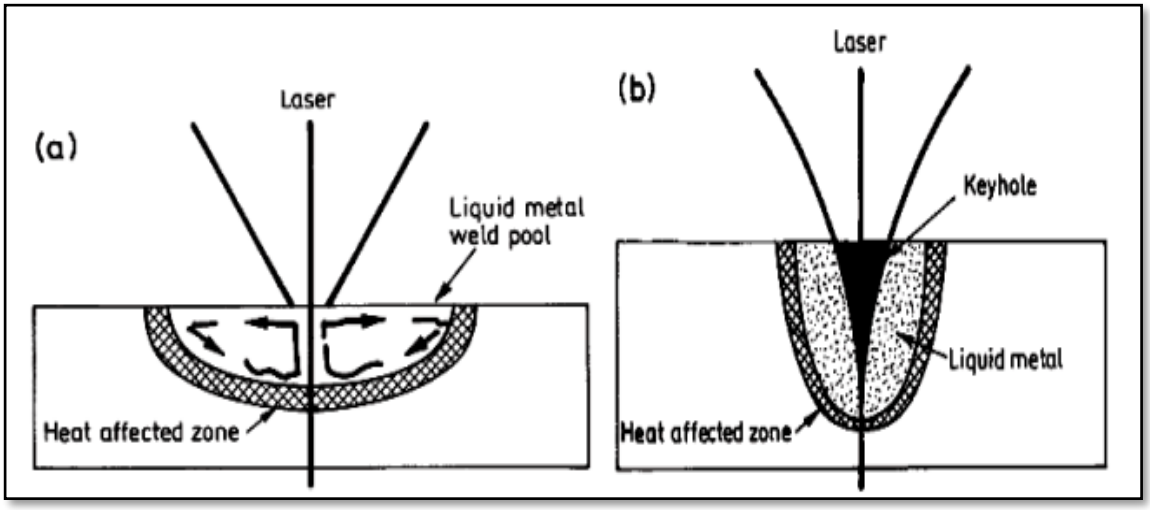

Figure (2.15): Modes of laser welding (a): conduction mode ;(b): key hole mode [60].

The alignment and fit-up tolerances may be quite wide due to the comparatively large beam size. Small component geometries with millimeter-sized weld beads are the perfect fit for the procedure. The weld bead has a superb visual appearance as a result of the consistent welding circumstances. However, the energy input per unit length of weld is relatively considerable when using conduction welding to join thicker parts, leading to a huge weld bead and significant distortion [61].

On the other hand, while welding with the keyhole mode (Figure2.15b), deep penetration is possible as the laser power surpasses 1 kW and the power density exceeds $10^6 W/cm^2$, and intense evaporation takes place on the melt surface. Figure (2.16) illustrates how the energetic evaporation-related rebound pressure is sufficient to create a deep, narrow depression in the molten material. Even when the beam strength and travel speed are constant, the keyhole, which is filled with a partially ionized plume of vapour and ambient gas, is known to be unstable and subject to dynamic changes [62, 63]. The equilibrium between the keyhole and the surrounding molten metal determines how stable the keyhole will be. The following equation can be used to represent this equilibrium:

$$Pv + PI = P\alpha + Pg + Ph \quad \ldots\ldots\ldots\ldots \quad (2.1)$$

Where:

Pv= Vaporization pressure

PI = Radiation pressure

Pα = Surface tension

Pg = Hydrostatic pressure

Ph = Hydrodynamic pressure

The equation can be reduced as follows because the values of PI, Pg, and Ph are small:

$$Pv = P\alpha \quad \ldots\ldots\ldots\ldots \quad (2.2)$$

This indicates that the equilibrium between the vapor pressure and the surface tension is what governs the stability of keyhole. The surface tension tends to close the keyhole while the vapor pressure tends to open it [64].

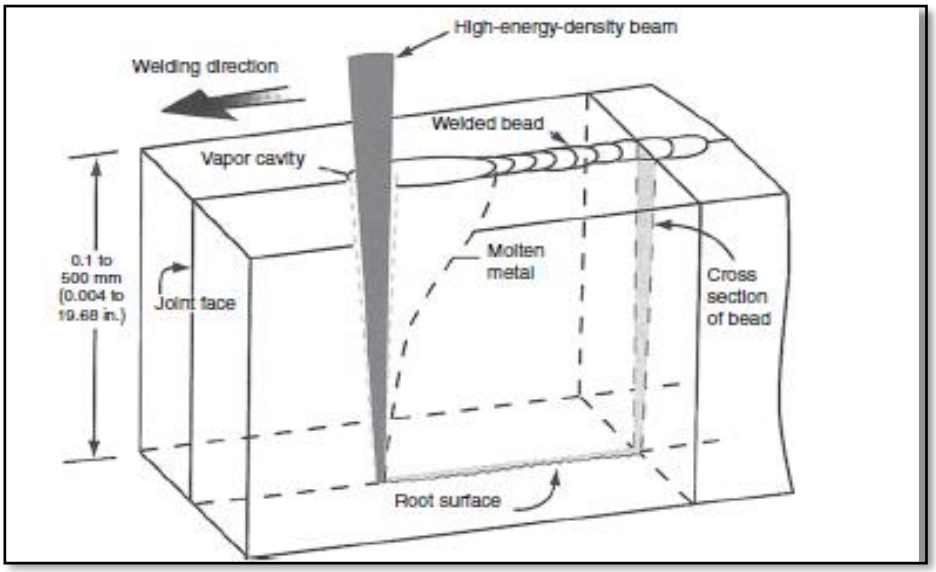

Figure (2.16): The weld pool using keyhole mode [23].

Due to numerous reflections within the keyhole, the rate of laser radiation absorption rises inside. A portion of the beam energy is absorbed by the material each time the beam strikes the wall of the keyhole. As a result, keyhole welding, also known as deep-penetration welding, enables very deep (>20mm) and narrow welds. Deep-penetration laser welding produces

temperatures in the keyhole that are so high that ionized metal vapor and temperatures well beyond 10,000K° (a plasma-like physical state) are reached. The plasma acts as an energy transmission medium by absorbing a portion of the laser beam. The plasma expands over the keyhole due to the keyhole's evaporation pressure. The plasma cloud then defocuses and scatters the CO_2 laser beam, increasing the focus diameter and altering the focus position and energy density. The plasma cloud also absorbs laser radiation. The weld's penetration depth is reduced by the enlarged plasma cloud. The energy absorption in the cloud causes the weld to take on a nail-head form. If there is a lot of plasma generation, the welding process can possibly stop. The plasma cloud, which emits bluish light and is distinguished by its composition, is often made up of a mixture of metal atoms, ions, electrons, and elements of the surrounding gas atmosphere. In some circumstances, the welding gas itself may potentially ignite the plasma, especially when argon is utilized as the welding gas [65]. As the laser power and pulse duration applied to the workpiece increase, the transition from conduction mode to deep penetration mode takes place. A power (or energy) transfer coefficient (η), which is the ratio between the incident laser power and the laser power absorbed by the workpiece, can be used to describe welding efficiency. η is typically quite tiny for conduction welding, but if a keyhole has been created, it can approach unity [66].

2.14 Parameters of CW FiberLaser Beam Welding

To increase success rates in laser welding, numerous process variables need to be carefully taken into account [67]. The keyhole shape of the laser weld bead is determined by the laser welding input parameters since their combination controls the heat input [11]. Correct selection of the output power, welding speed, focal location, shielding gas and position precision are necessary for a high-quality weld [68].

2.14.1 Parameters of Continuous Laser Beam Welding

- **Laser Power**

Laser welding can be carried out using one of the laser generation mechanism: continuous welding and pulse welding. Continuous wave (CW) welding (Figure 2.17a) supplies stable laser beam power, resulting in continuous generation of laser beam reflection among the resonator mirrors. Over time, a fraction of this radiation progressively leaves the resonator through the partially reflected mirror. Because the resonator can provide a continuous laser beam, thicker materials can be penetrated more deeply. In CW mode, it is possible to weld several metals. Long periods (a few minutes or even hours) are frequently needed for CW lasers to settle the beam intensity for highly steady output. Pulsed welding (Figure 2.17b) fundamentally involves quickly turning on and off the laser. Here, the workpiece's overall energy input decreases. Therefore, for very heat-sensitive materials, pulsed welding is utilized. Each cycle of this procedure lasts a millisecond. Pulsed welding can create ripple effects in welds. It is thus employed in seam welding. The frequencies of pulses range from 100Hz to 10kHz [11,51]. The weld penetration depth is directly affected by laser energy. Abdel-Monem and Abdel-Fattah [69] revealed in 2011 that the penetration depth increases dramatically as laser power increases. When the power increased from 4 to 8kW, the depth of penetration increased from 3.4 to 4.7mm. As laser power is increased, the interface's penetration depth and weld bead diameter increase too [70,72].

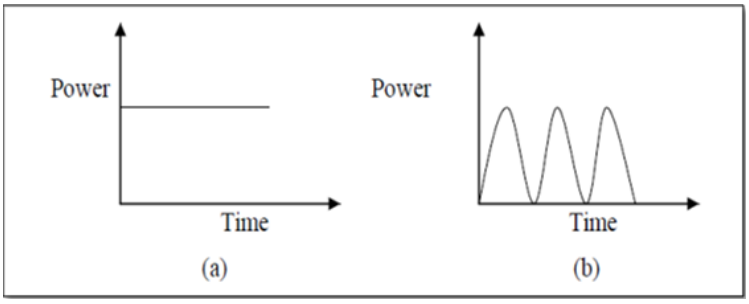

Figure (2.17): Time and laser power relationship during (a): continuous laser wave, (b): pulsed laser wave [11].

- **Welding Speed**

The two key factors that determine the weld geometry, including its depth and width, are laser power and welding speed. For instance, while other processing parameters are held constant, a slower welding speed can result in the melt pool expanding and becoming wider. A weld with dropout is typically created at a slower welding speed, as seen in Figure (2.18). A faster welding speed can create a significant flow in the melt pool's center and reduce the amount of redistribution in the keyhole. Due to the limited heat input brought on by fast welding speeds, there was a lack of penetration at these speeds. This suggested that it was important to carefully balance the amount of heat used and the welding speed. The weld quality drops as the welding speed rises, and the weld metal develops pores [73, 74].

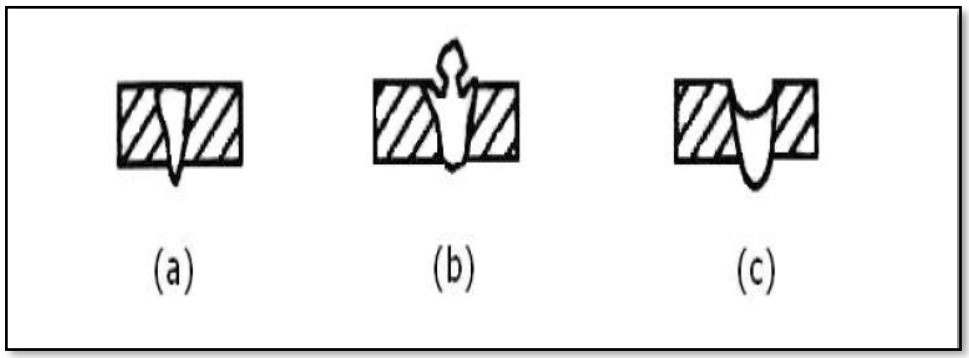

:

Figure (2.18): Weld geometry affected by welding speed: (a) at the suitable welding speed; (b) at high welding speed; (c) at low welding speed [71].

- **Focal Spot Size**

The diameter of the beam at the focal point can be used to define focal spot size [59]. It establishes the density, or energy per unit area of the focus point as well as the precision of the features that can be welded. Because laser-material interactions are dictated by the energy density at the site of contact, focal size is a crucial consideration. The smallest focusing point for a given laser power produces the largest power density, however the high power density is not necessarily ideal for welding because it may

result in significant metal evaporation, which would produce the underfill fault. The welding geometry will be extremely narrow for a small focal spot, which is sensitive to the joint's alignment precision [43]. The following equation can be used to calculate the focal spot size.

$$d = 2 \times \theta \times F \quad \text{..... (2.3)}$$

Where:

d = Focal spot diameter (mm)

θ = Beam convergence angle (radians)

F = Focal length (mm)

- **Power Density or Irradiance (I)**: The energy density of the beam or radiation is defined as the energy of the laser beam per unit area on the surface. Power density, is given by the equation:

$$I=P/A \quad \text{..... ..... (2.4)}$$

Where: A is the area of the laser beam that is targeted at the workpiece surface [59]. The amount of heat needed to be supplied for the fusion of the faying surfaces directly depends on the energy density associated with a specific welding procedure. Because the time period over which heat must be applied during welding for melting reduces with an increase in power density, less heat is needed for melting and welding of work components. The less time spent applying heat, the less heat is transferred from the faying surfaces to the base metal (BM), resulting in a situation where the majority of the heat delivered to the faying surfaces is only used for their fusion.

- **Shielding Gas**

Another important component that affects weld quality in laser welding is the shielding gas. In some cases, the shielding gas may have an

effect on the degree of scattering of the beam focus generated by the plasma column created above the keyhole. The shielding gas can also change the shape and size of the keyhole by changing the surface tension of the weld pool surface, interacting with the hot metal to release more energy, modifying the plasma conditions inside and on the surface of the keyhole. According to earlier research, helium is better suited for CO_2 lasers than argon. This is because He has a strong ionization potential appears to regulate the creation of plasma during CO_2 laser welding [56,75]. For high-power CO_2 laser welding, argon should not be utilized since it is thought to support the plasma. The Nd:YAG lasers can employ argon because they don't produce as much plasma. Because the wavelength of ytterbium-doped fiber lasers is similar to that of Nd:YAG lasers (1070 nm), pure argon might be the best shielding gas for high-power fiber laser welding. In contrast to Nd:YAG, disk and fiber laser welding, which only produces a laser-induced plume from a keyhole, CO_2 laser welding allows for the easy creation of Ar or N plasma (Figure 2.19). The absorption caused by Inverse Bremsstrahlung, whose effect is approximately 100 times greater than that of Nd:YAG, disk or fiber laser, is used to interpret the interaction between the CO_2 laser beam and the gas plasma [49,56].

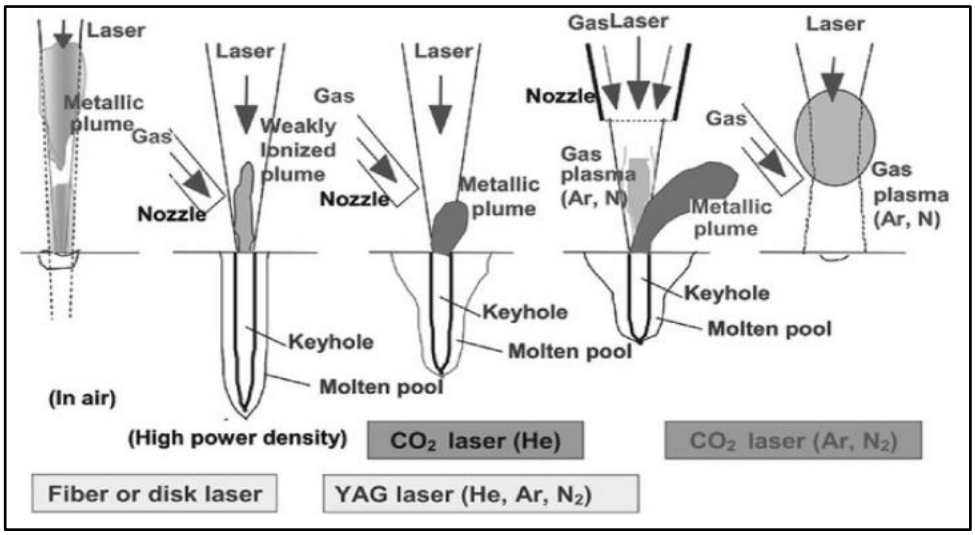

Figure (2.19): Effect of protective gases on welding penetration by using different laser welding methods [49].

- **Beam angle:** It can be defined as the angle of the laser beam at which welding occurs and greatly affects the penetration of the weld.
- **Nozzle design:** To improve the connection between the incident laser beam and the weld surface, and to stop the production of oxides, respectively, conical and ring nozzles are utilized [76].

2.14.2 Parameters of Pulsed Nd:YAG Laser Welding

- **Pulse width:** The duration of the laser pulse is its pulse width. Milliseconds are used as the units. It regulates the welding processes heat.
- **Pulse repetition rate:** It is the number of pulses of flash lights per second. In addition, it regulates the welding heat.
- **Pulse energy:** Peak power and pulse width combine to form pulse energy [76].

2.15 Laser Beam Welding Types

The simplest way to classify lasers is by their lasing mediums, which are divided into four major groups based on the condition of the lasing material: gas, liquid, solid and semiconductor lasers. Additionally, there are two temporal modes used by all laser types: continuous wave and pulsed modes. The laser beam is continuously emitted when in CW mode. The laser beam emits pulses while in pulsed mode [52].

2.15.1 Gas laser

Gas lasers use high voltage, low current power sources to excite the lasing medium (a gas mixture such as N, He, and CO_2) for CO_2 lasers. Gas lasers have the potential to produce substantially more power than solid-state lasers, and they can operate in both continuous and pulsed modes [49,51], as shown in Figure (2.20). Solid-state lasers have a wavelength of 1.06μm, while CO_2 lasers create wavelengths of 10.6μm. Because optical

fibers are damaged by the absorption of high wavelengths in this laser, a mirror and stiff lens delivery system are utilized instead. A gas laser can provide power outputs (up to 40kW), which is more than a solid laser. Similar to this, low-power laser beam applications use gas lasers like the He and Ne laser, which emits laser beams in the visible range [11]. The CO_2 laser is generally less expensive. Its employment with highly reflective metals like Al is constrained by its light's increased reflectivity. Compared to CO_2, solid-state lasers are smaller and require less maintenance [25].

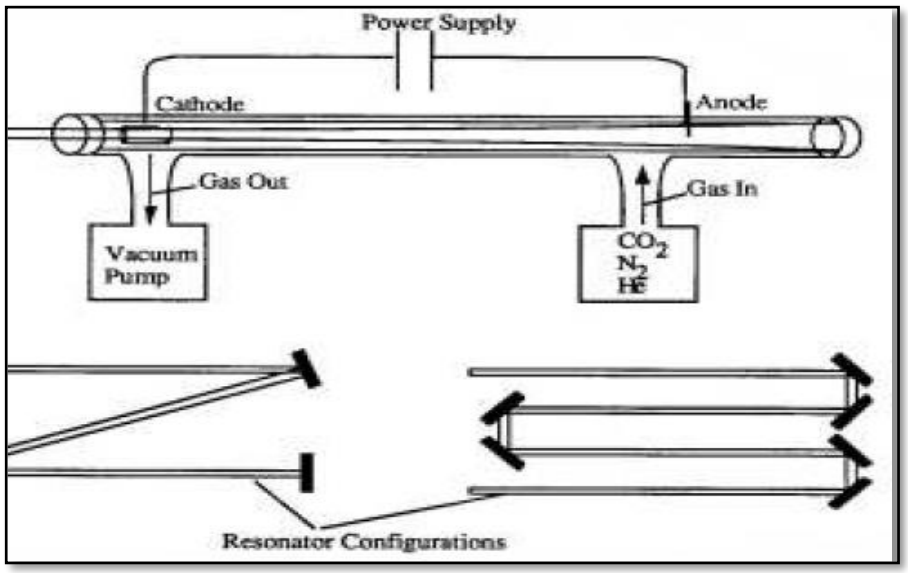

Figure (2.20): CO2 laser generation system [25].

2.15.2 Solid State Laser

Figure (2.21) illustrates how ions suspended in a crystalline matrix are used in solid lasers to produce laser light. The electrons for excitation are provided by the ions or dopants, and the crystalline matrix propagates the energy between the ions. Neodinium (Nd^{3+}) for Nd:YAG and Nd:glass lasers and Chromium (Cr^{3+}) for ruby lasers are the two main kinds of dopants in the laser medium [49]. Ruby lasers are generally no longer employed due to their low energy efficiency and limited application possibilities [52].

- **Nd:YAG Laser**

This laser's host lattice is a crystal of yttrium aluminum garnet (YAG), which has the chemical formula $Y_3\ Al_5\ O_{12}$ with some Nd^{3+}ions (between 0.1-2%) in place of Y^{3+} ions. Depending on whether pumping is constant or intermittent, the Nd:YAG laser can be operated in either the CW or pulsed modes. The rod size is comparable to that of the ruby laser, and the excitation source can be either a xenon flash lamp or a krypton lamp. The power output ranges from 150W to 6kW in CW mode, and it is in the range of 50MW with a pulse duration of around 20ps and a repetition rate of 1-100Hz in Q-switched pulsed mode. When three Nd:YAG rods are lined up as a single oscillator and each rod is arc lamp pumped, a high-power (up to 2kW) CW laser can be produced. Pumping with a diode laser results in the extremely high powers (up to 6kW). Both pulsed and CW Nd:YAG lasers typically have efficiencies between 1 and 3%. Laser surgery and material processing, such as welding, drilling and surface modifying, are two uses for Nd:YAG lasers [51].

Fiber Laser Welding

Another type of solid state laser is the fiber laser, which employs a silica glass optical fiber as the active medium with a core that has been minimally doped with rare earth elements like erbium (Er), neodymium

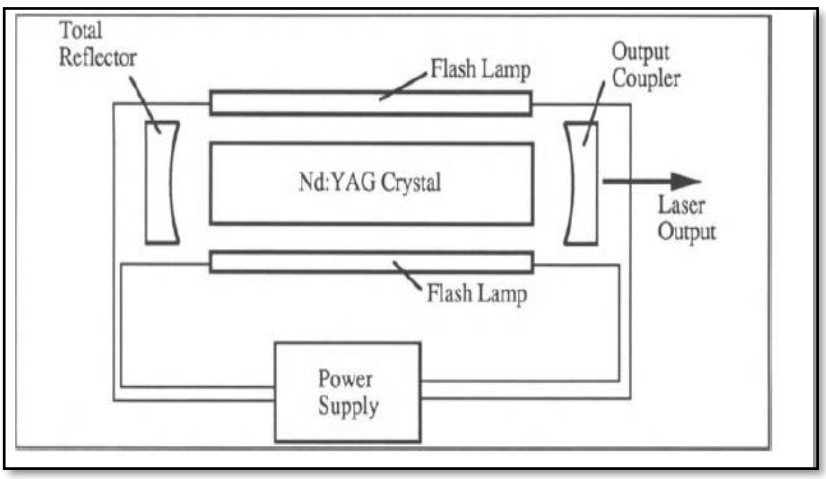

Figure (2.21): The Nd:YAG laser system [51].

(Nd), thulium (Tm) and ytterbium (Yb). The rare earth elements employed as a dopant determine the wavelength of the fiber laser light. Because other types of fiber lasers have lower wall plug efficiency, nowadays the majority of high power fiber lasers on the market use Yb. The wavelength of the Yb laser is 1.07μm, which is comparable to the Nd:YAG laser. High power diode bars, similar to those used in diode-pumped Nd:YAG lasers, or semiconductor single emitter diodes that are connected into the doped active fiber are utilized for pumping. The benefits of using a diode laser over a diode bar include higher output power, higher pumping efficiency and no need for alignment optics. This is because all other diode pumped lasers use water cooling or fiber cooling, which requires less cooling, a significantly longer lifetime of over 100,000 hours, less maintenance and downtime, and lower costs for diode replacement [5]**.** There are single-mode and multimode fiber lasers. Single-mode fiber lasers can currently be found with power ranging from a few watts to 5kW. A multi-mode fiber laser has a maximum output power of more than 50kW. Good beam quality, excellent energy efficiency, minimal maintenance costs, and compact size are properties of fiber lasers. They operate well for the majority of laser material processing applications. They have also been thought of as potential replacements for other laser systems (such Nd:YAG and CO_2 lasers) in the industrial setting. Table (2.2) provides comparisons between commercial laser systems. Fiber lasers are able to provide a deeper penetration weld by using a low laser power because of their superior properties. The military, telecommunications, and medical devices are some of the most common fields used with fiber lasers [71]. The 1.07μm wavelength of the fiber laser allows for long-distance transport over a fiber. In addition, fiber lasers have good beam quality, small and lightweight, simpler attainment of high-power, high-intensity and high efficiency, and need no maintenance. Commercially available fiber lasers include CW

multi-mode lasers with a maximum power of 100 or 120kW and CW single-mode fiber lasers with a maximum power of 10kW. A fiber with a diameter of 0.5mm and a length of 50mm is used to deliver a 100kW fiber laser, which is made up of 90 sets of 1.2kW lasers. On the other hand, a single-mode fiber laser's disadvantage is that its delivery lengths are often low and dependent on the laser power. Single-mode lasers now have a greater delivery range. For microprocessing (welding and cutting) of thin sheets, marking, 3D printing, etc., low-power lasers of less than 1kW are utilized. Commercially accessible pulsed fiber lasers with great efficiency can replace pulsed YAG lasers. For microprocessing of Cu sheets, ultra-short pulse lasers or green lasers are also developed [16,77].

Table (2.2): A Comparison of traditional laser systems [71].

	CO_2	Nd:YAG	HPDL	Fibre Laser
Wavelength (μm)	10.6	1.06	0.8-1.0	1.07-1.08 (Ytterbium) 1.8-2.0 (Erbium)
Efficiency (%)	5-15	1-3 (lamp pumped) 10-20 (diode pumped)	20-50	60-70
Output power (kW)	up to 45	up to 8	up to 8	50 (multi-mode) 5 (single-mode)
Average energy intensity (J/mm^2)	10^{6-8}	10^{5-9}	10^{3-5}	10^{8}
Maintenance periods (hour)	1000	200 (Lamps)	free	10000-100000

•Disk laser

Instead of being a rod, the solid-state laser medium of this type is an extremely thin disk. Since Yb:YAG is employed in this instance as the gain medium, the beam can be given via fiber, as illustrated in Figure (2.22). Never use an injected lamp and always use a diode-pumped disk laser [49]. The disc laser has a high degree of efficiency at high energy levels and a high level of beam quality. As a result, it is employed in microprocessing, and disc lasers can currently replace CO_2 lasers in multi-kilowatt thick plate applications [78].

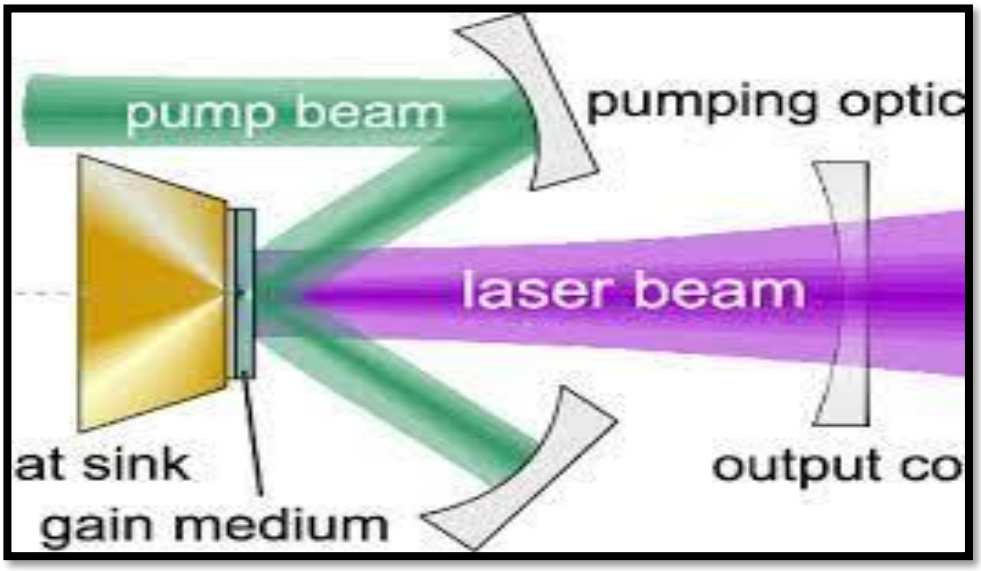

Figure (2.22): Disk laser system [78].

2.15.3 Liquid Laser

It is also known as a dye laser since the laser's medium is a dye that has been dissolved in ethanol, water, or another liquid solvent. Any wavelength between 320 and 1200nm can be produced coherently by carefully choosing the dye. There are numerous industrial uses for liquid lasers, such as the medical, defense, and scientific fields [79].

2.15.4 Semiconductors Laser

When voltage is placed across the p-n junction of the electrodes, a p-n type semiconductor serves as the active medium in this type of laser. When a voltage is supplied, the active layer's two mirror-like edges combine with holes at the p-n junction to produce light, as seen in Figure (2.23). Currently, this light is not a laser. Because the coated layers' refractive indices are lower than that of the active layer's, it is contained within the active layer. Additionally, during the exchange of light in the active layer, the ends of the active layer function as reflective mirrors. A laser oscillation is then produced once the light is intensified by the stimulated emission mechanism [80].

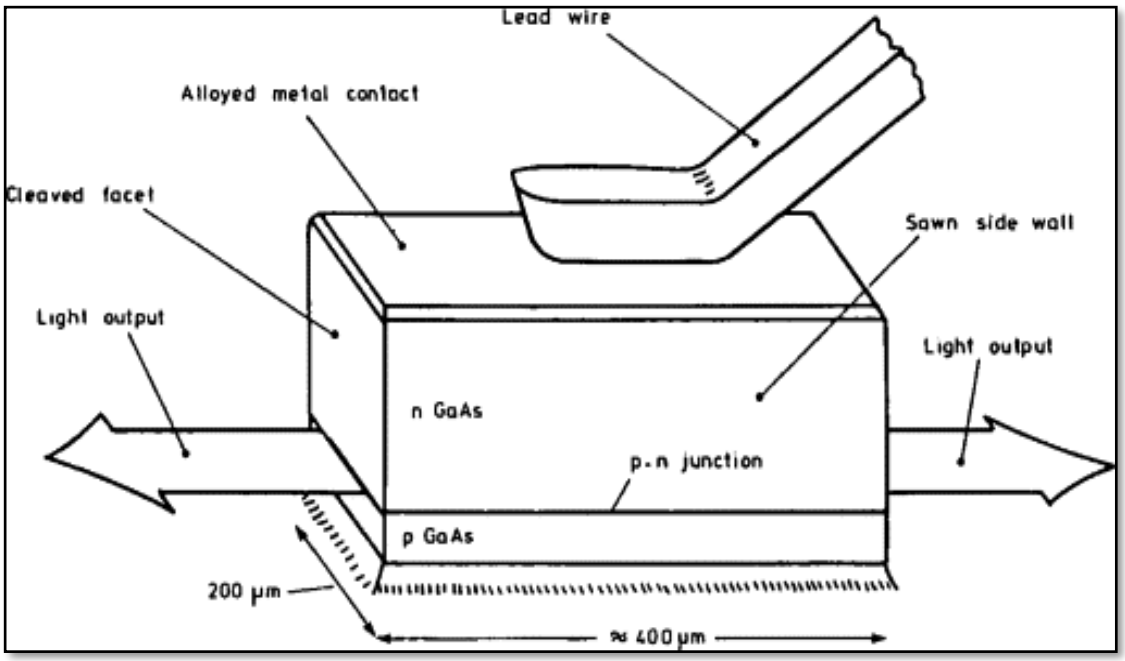

Figure (2.23): Semiconductor laser system [80].

2.16 Laser Welding Joint

The preferred joint for laser beam welding is one that promotes keyhole creation by absorption. Different thicknesses of the item to be joined have no effect on high-intensity welding operations. This enables a few novel sorts of joints, as depicted in Figure (2.24) [53].

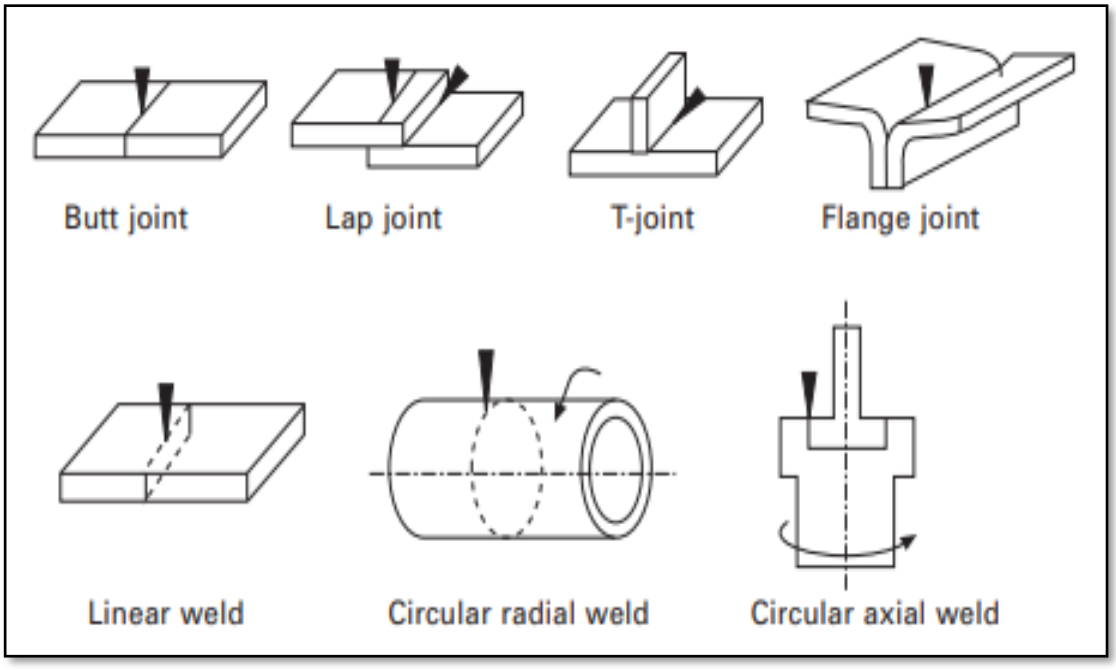

Figure (2.24): Various arrangements for welding joints [49].

Joint preparation is a crucial step in the laser welding process; with the right joint preparation, multi-pass laser welding can be used to join even very thick sections. Generally, the joint design depends on the application. Different joint designs, including single-pass V and T joints, butt joints, and lap joints, have been used while laser-welding titanium alloys. Butt joints are the most often used joint configuration. The alignment between the beam and the joint must be good when designing butt joints. The complexity of the connection fit-up is one disadvantage of butt-welding, which calls for the highest precision along the edges to be welded. However, the stringent butt joint fit-up requirement is lessened by the introduction of filler metals [49].

2.17 Laser Welding of Titanium and Its Alloys

Ti applications require superior chemical, thermophysical and mechanical qualities[20], such as a high mechanical resistance to weight ratio, excellent corrosion resistance, and favorable high temperature behavior. Additionally, these alloys are commonly employed for bio-medical applications due to their bio-compatibility [81]. Most of these applications require the use of joining procedures. Titanium welding technology offers unique characteristics. When heated to temperatures above 350°C, Ti aggressively interacts with ambient gases such oxygen, hydrogen and nitrogen; as a result, the mechanical characteristics of the weld joint significantly deteriorate. While exposing the titanium alloys to welding thermal cycles, a significant increase in grain size occurs. Therefore, welding should be performed with little heat input under an environment of inert gas. Various welding techniques, such as TIG welding, friction welding and EBW have been practiced to obtain joints from titanium and its alloys. Each of these methods has a significant drawback. TIG welding and friction welding have a limited range of

applications, due to the restricted dimensions of the weld pieces [23]. The overall dimensions of the weld workpieces can only be welded using an electron beam, and the process is labor-intensive since a vacuum must be created in the working chamber. The most promising method for welding Ti is laser. There has been a wide spectrum of study in this area. There are studies including the use of solid-state laser radiation in pulse mode to reduce residual welding distortion, and in continuous mode to weld thick Ti sheets of 16mm [82].

2.18 Advantages of Laser Welding

1- The ability to weld materials and thicknesses that are different [59].

2- The FZ is made narrower by the laser beam weld.

3- Geometries in three dimensions can be welded.

4- Small defects in the weld metal can be produced by laser welding along with a very narrow HAZ and low residual stresses.

5- High welding speeds.

6- Filler metal is not necessary.

7- Simple automation, especially with lasers suitable for fiber optic delivery.

8- The production of extremely small weld sizes, required for tiny and delicate components, is made possible by concentrated heat sources.

2.19 Limitations of Laser Welding

1- Equipment is extremely expensive.

2- Usually, portability is poor.

3- Requires precise joint location in relation to the beam and very tight joint fit-up.

4- Aluminum and other highly reflective metals can be challenging to weld with some laser beam welding techniques.

5- At welding some steels, high weld cooling rates may result in brittle microstructures.

6- Possible problems with laser plumes.

7- Certain lasers demand specialized (and expensive)eye protection [23,83].

2.20 Metallurgical Aspects of Laser Welding

The workpiece material undergoes heating, melting, solidification and formation of the FZ with different structures during laser welding. As it depends on the material compositions, solidification modes, cooling rates, etc., solidification is a very complex process. The quality and effectiveness of the laser-welded pieces are most strongly influenced by the structures that have developed in the FZ [45,61].

2.20.1 Solidification of the Weld Metal

Solidification behavior is affected by different parameters such as temperature gradient (G), solidification growth rate (R) and quenching rate. The solidification behavior affects on the grain size and shape of the welded microstructures and the extent of segregation, the distribution of impurities, the extent of defects such as porosity and hot cracks, and ultimately the properties of the solidified weld metal. When a liquid of metal is cooled below its melting temperature, there is a driving force for solidification. The initial solidification in a weld occurs epitaxially at the melt pool walls. Epitaxial solidification is a heterogenous process. After nucleation, growth of the solid occurs by the addition of atoms from the liquid to the solid at the solid/liquid interface [18]. The nature of the

solid/liquid interface will be determined by the G and R at the solid/liquid interface. The mode of solidification can be planar, cellular, or dendritic depending on the solidification condition. Figure (2.25) shows the variation of microstructure as a function of G and R, and the effect of these two variables. Ratio G/R is related to undercooling, and the product G*R is related to cooling rate. The high G/R ratio will generate a planar mode, while the low G/R will generate dendritic solidification. High cooling rates (G*R) will produce finer solidification structure than slow cooling rates. The solidification conditions may change during solidification. During welding the ratio G/R decreases while advancing from the fusion line toward the centerline. This suggests that the solidification mode may change from planar to cellular, columnar dendritic and equiaxed dendritic across the FZ [3]. There are various requirements for solidification. Firstly, it is requisite to nucleate solid species in the liquid phase. Once solidification begins and the liquid turns into a solid, it is necessary that heat of fusion created by the transformation be dissipated. This generally occurs by conduction through the solid away from the solidification front. The solidification of an alloy is also necessary to redistribute solute between liquid and solid, since the composition of the liquid and solid which in contact at the solidification front changes continuously as the temperature decreases within the solidification range. This redistribution will result in local variation in composition in the solidified structure if the solid does not have time to reach its equilibrium composition, which is common in most casting and welding processes [84].

During the solidification of alloys, constitutional super cooling occurs. The solute is detached into the liquid ahead of the solidification front. This causes a corresponding variation in the liquidus temperature-producing conditions, where the melting point of the liquid is higher than the temperature of the liquid. This allows small perturbations on the

solid/liquid interface to expand into the supercooled liquid. When the tip of any protuberance is at a higher temperature, the growth will be in planar mode. However, as long as the temperature of the tip is lower than the melting temperature, solidification can occur and the tip may grow in a cellular/dendritic manner. As shown in Figure (2.26), increasing constitutional supercooling favors dentritic growth [25].

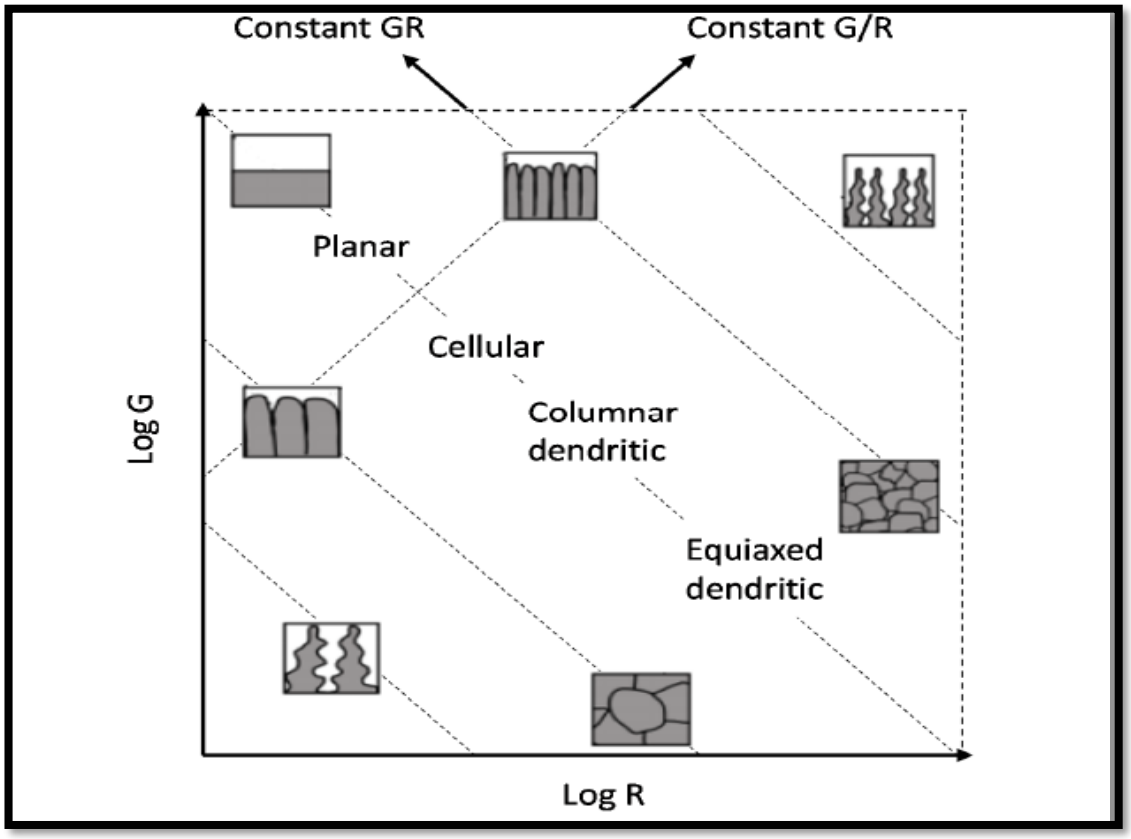

Figure (2.25): Difference in the solidification microstructures as a function of temperature gradient [84].

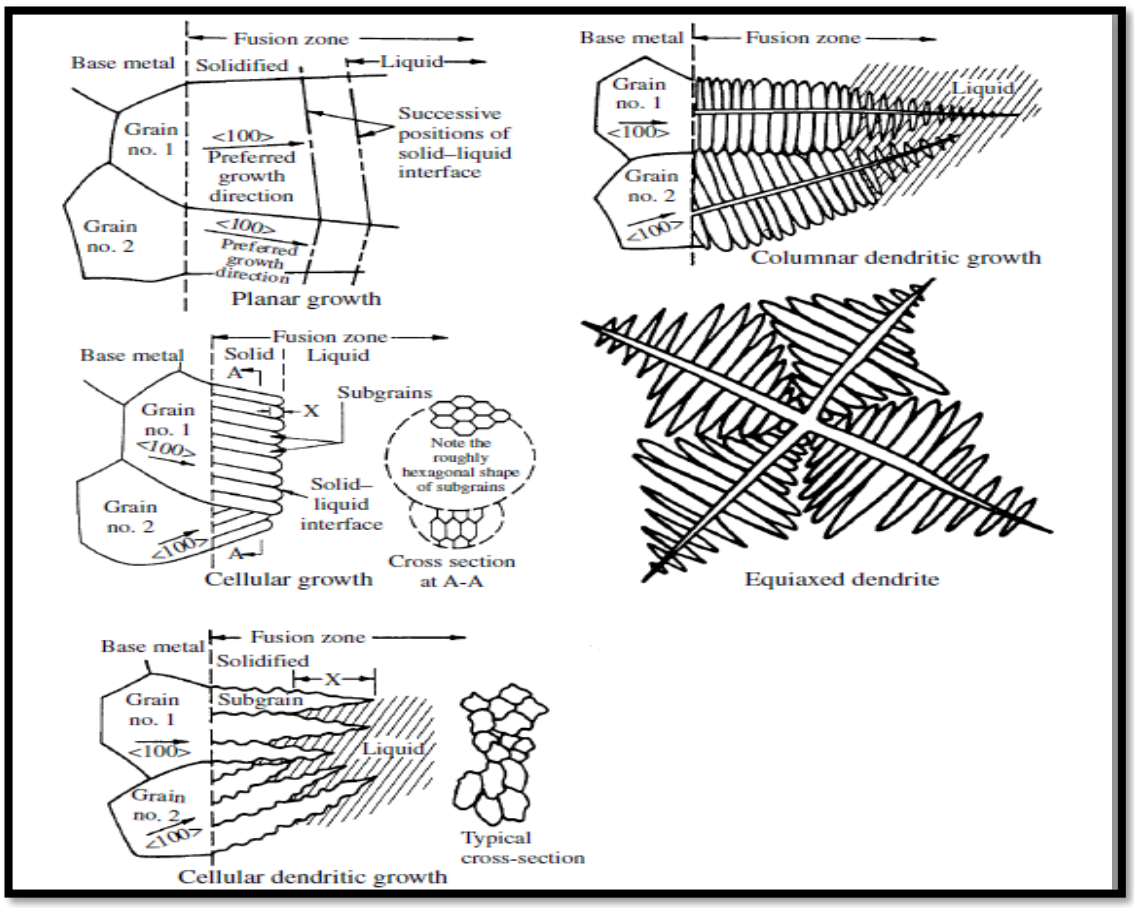

Figure (2.26): Different solidification modes as a result of the effect of constitutional supercooling [84].

During welding of titanium alloys, β grains nucleate epitaxially, and grow preferentially towards the maximum temperature gradient. The favored growth direction for the dendrites in metals with cubic crystal structure is in the <100> direction. Therefore, the nucleation sites with the <100> direction aligned with the temperature gradient will outgrow less favorably oriented grains. Large grains in the base material and the HAZ provide fewer epitaxial growth sites at the fusion boundary and dictate large prior β grains in the FZ [85,86]. The lack of segregating elements in Ti-6Al-4V also provides limited constitutional undercooling which leads to coarse prior-β grain structures in cast and welded alloys. The narrow freezing range, lack of segregating elements and low melting phases makes Ti-6Al-4V welds unsusceptible to solidification related cracking which may be a problem for other high strength structural metals [24].

2.20.2 Continuous Cooling of the Weld Metal

Depending on the cooling rate from β phase field, the transformation can be diffusionless (martensitic) or nucleation and diffusion controlled. For high cooling rates the transformation will be diffusionless forming martensite. In titanium alloys two martensite morphologies are observed, massive and acicular martensite. Massive martensite occurs only in pure titanium, very dilute alloys and in alloys with a high martensitic transformation temperature. Acicular martensite occurs in alloys with higher solute content (lower martensitic transformation temperature). The acicular martensite consists of individual α laths, each with a different crystal orientation. In Ti-6Al-4V alloys, the slow cooling rate leads to a diffusion controlled transformation. The α phase first nucleates preferentially at β grain boundaries forming a continuous α layer along β grain boundaries. During continued cooling, α plates nucleate at the β grain boundaries and grow into the β grains as parallel plates belonging to the same variant of the Burgers relationship forming a so-called α colony. The α colonies continue to grow until they meet another α colonies. With increasing cooling rate, the size of the α colonies as well as the thickness of the individual α plates becomes smaller. At higher cooling rates, α plates start to nucleate also at the α colony boundaries and start to grow perpendicular to the nucleation site forming a basket weave structure [17,35,86].

2.20.3 Microstructural Evolution during Laser Beam Welding of Titanium Alloys

It is pointed out that the weld pool geometry is greatly affected by focus/defocus beam which may create a surface tension, which is responsible for the metal flow, and hence, the WZ shape. The widening top and bottom surfaces, hence, hourglass-shaped is due to the presence of

Marangoni convective currents which drives away the molten metal from the location of the heat source [42]. The width of the FZ decreases with increasing welding speed and increases with increasing laser power [50].

Ti alloy welds consist of three distinct regions, i.e., the BM, HAZ and the FZ, depending on the temperature experienced during the welding operation**.** A clear boundary between the BM and HAZ is easily distinguished due to the microstructural differences. However, the fusion line is not accurately identified due to the similar microstructures formed in the HAZ and FZ, and thus it is approximately determined according to the location of weld root and weld toe [87]**.**

The microstructural analysis of a typical α titanium alloy (Ti-5Al-2.5Sn) conducted in 2018 by Auwal et.al. revealed that the BM structure contains fine equiaxed α-grains, as shown in Figure (2.27a). The microstructure of the FZ changed from granular-like to columnar-like (Figure 2.27b). The FZ consists of a very fine α′ martensite because of the low heat input and higher cooling rate in this zone. In contrast, no clear evidence of martensite has been observed in CP-Ti laser weld beads due to the relatively low content of the constituents promote martensitic formation. The microstructural evolution of the FZ of the pure Ti alloy depends significantly on the β→α phase transformation associated with the cooling rate. The HAZ (Figure 2.27c) contains a mixture of martensite, primary α phases, and transformed β phases.

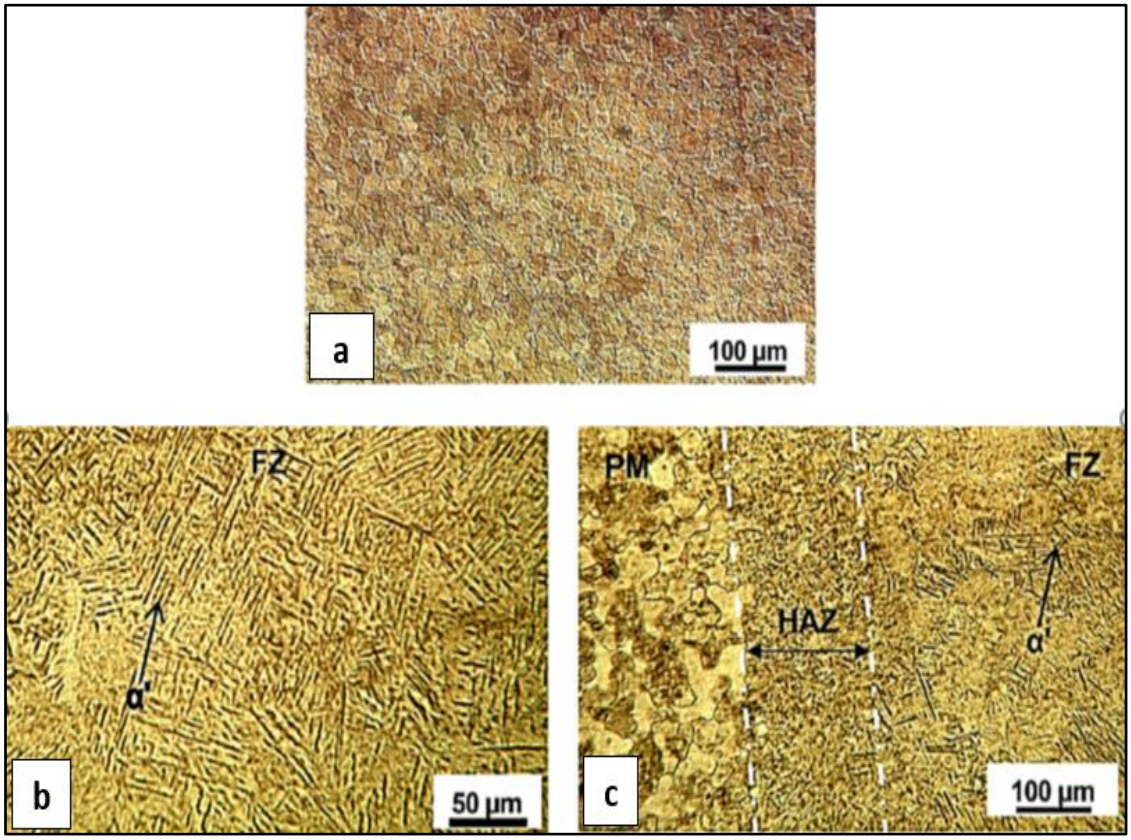

Figure (2.27): Microstructure of Ti-5Al-2.5Sn alloy (a): BM (b): FZ (α′ martensite formation) c): FZ/HAZ/ BM [26].

The BM of the Ti-6Al-4V alloy has been found to be composed of a dark β phase in a bright α matrix, which is the typical annealed structure of the base alloy. Namely, the BCC structured β phase distributes along the boundaries of the HCP structured α phase, as shown in Figure (2.28). The microstructure of the HAZ is a mixture of ά', acicular α and primary α phases. This structure arises when it is quenched below the β-transus ranging from 720 to 985°C. The FZ, instead, mainly consists of acicular $\acute{a}$ martensite. A similar structure is obtained when quenching the alloy from the β phase region above the β-transus, which is 985°C approximately. It has to be assumed that a value of 410°C/s required to obtain a completely martensitic microstructure for the Ti-6A1-4V alloy. The acicular martensitic structure is formed by columnar α and β grains in the FZ. This transformed microstructure exhibits high strength and hardness value at the expense of ductility and toughness [14,88].

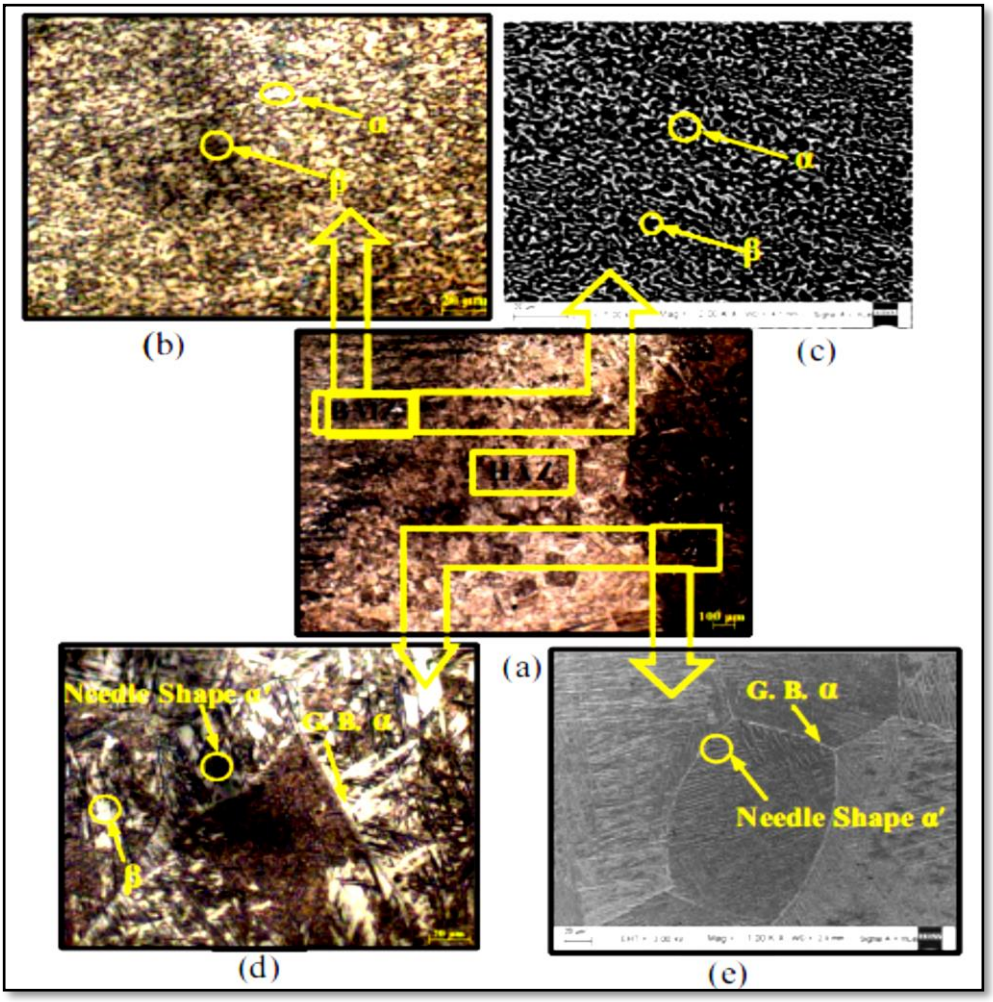

Figure (2.28): The microstructure of the Ti-6Al-4V alloy by using an: (a) optical image containing from three zones (BM, HAZ, and FZ); b) optical image, and (c) SEM image of BM; (d) optical image, and (e) FESEM image of FZ [88].

There is still some retained β available in the microstructure due to the presence of β-stabilizer (Vanadium). Vanadium brings the martensite formation temperature below room temperature, resulting in some remaining β always present. The α′ martensite is a supersaturated non-equilibrium hexagonal α-phase. The volume fraction of α′ increases with increasing cooling rate [76]. Addition of small amounts of boron to cast Ti alloys have shown to render a finer microstructure and improved mechanical properties. This boron enrichment causes a corresponding variation in the liquidus temperature, thereby leading to higher constitutional supercooling which provides an additional driving force for

the nucleation of more fine β-grains ahead of the solid/liquid interface. The presence of equiaxed grains in boron titanium alloy castings implies that constitutional supercooling is more important during solidification than thermal undercooling [25].

2.21 Mechanical Properties of Laser Titanium Alloys Welds

2.21.1 Microhardness

Hardness testing is often the best way of establishing component's survival and performance in their specific applications. The hardness values of the welded samples depend on the presence of different phases of the materials and developed microstructures during welding. The hardness values in the HAZ give indications of its susceptibility to cracks. The hardness values in the FZ are also commonly used to find out the less ductile phases which may be prone to cracking [22]. In general, the hardness of joints is closely related to their microstructure resulting in diversity of mechanical properties. For typical α-alloys and near-α alloys, the FZ is reported to have higher microhardness value than the BM. This is due to the formation of a fine acicular α′ martensitic structure associated with the higher cooling rate. Then, the microhardness drops rapidly in the adjacent HAZ, and the BM has the lowest microhardness values [89]. In the Ti-6Al-4V alloy, it is also observed variations of the microstructures occurring during laser welding, which are clearly reflected in the hardness distributions of the welded joints. The hardness values over the narrow HAZ vary significantly. Full martensitic structure is obtained near the fusion boundary and the amount of the martensite decreases gradually while advancing from the fusion boundary, and finally disappears at the HAZ/BM interface, as shown in Figure (2.29) [1,12,90].

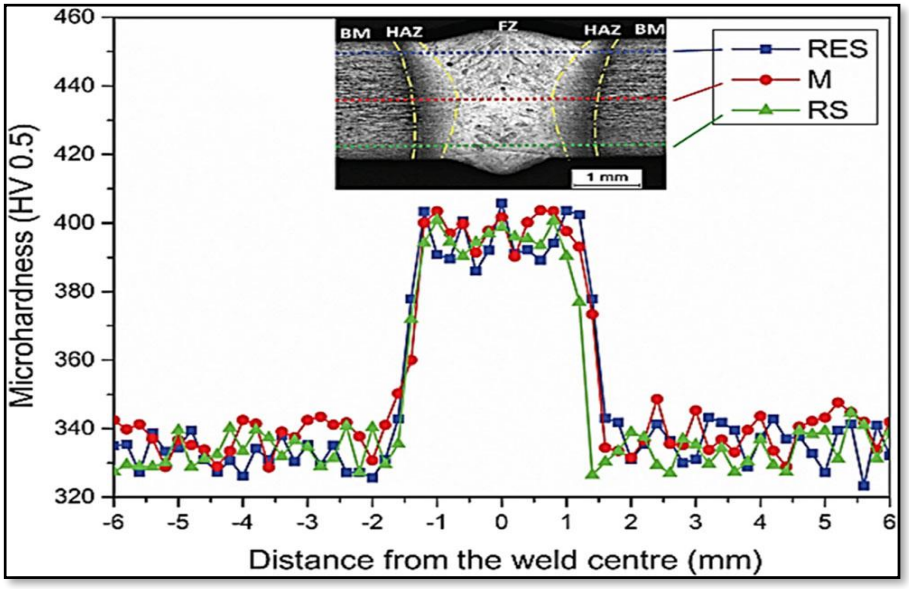

Figure (2.29): Microhardness distribution across the Ti6Al4Valloy laser weld [85].

2.22.2 Tensile Strength

Tensile test is typically used to analyze the ultimate tensile strength (UTS) and percentage elongation of the BM and laser-welded specimens. If the specimens fractured from the BM, this means that the tensile strength of the weld is higher indicating that defect free joints are obtained [11]. On the other hand, if pores in the FZ are formed, the tensile strength of the laser-welded specimens will be less than the BM. The stress concentration increases at pore locations during tensile loading, and crack propagation starts from the micro pores. The formation of a fine acicular martensite α′ in the weld bead during LBW reduces the ductility of the welded joint. It is known that the UTS firstly increases with the increase in heat input and becomes maximum, and thereafter decreases [91].

2.22 Main Metallurgical Defects of Laser Titanium Alloy Welds

2.22.1 Surface Oxidation

Ti is very reactive with ambient contaminants such as oxygen, nitrogen, hydrogen and carbon dioxide at high temperature. Therefore, one

of the most commonly encountered defects of Ti and its alloys is the formation of a hard and brittle Ti oxide surface layer. The formation of the oxide layer can be detected by visual inspection [48]. The degree of contamination is often determined by the color of the oxide that forms during welding. The oxide color is a function of its thickness. A light silver or bronze colored oxide indicates a mild contamination, while blue or purple oxides are an indication of more extensive atmospheric contamination, and may result in the rejection of the weld based on the suspicion of embrittlement. A white, flaky oxide indicates severe contamination. However, it is important to remember that the oxide can be easily removed by wire brushing after welding; so a complete reliance on the oxide color as a measurement of the weld quality is not always the best approach [23].

2.23.2 Embrittlement

Ti has an elevated affinity for elements such as hydrogen, nitrogen and oxygen at temperatures exceeding 500°C, which may result in embrittlement of the weld metal if they are absorbed. This discoloration is directly related to the degree of the weld metal embrittlement and hardness. To avoid embrittlement, Ti alloys are ordinarily shielded with a high-purity inert gas when they are keyhole laser welded. For reasons related to its ionisation energy and the formation of a beam attenuating plasma, helium is utilized when welding with a 10μm wavelength focused laser beam, whereas argon is used when welding with a 1μm wavelength focused laser beam. The shielding gas is often delivered through a trailing shield, which covers the weld face, and through an efflux channel covering the weld root. At sufficiently slow welding speeds, the shielding gas may be delivered through a co-axial or lateral nozzle. This approach is often employed when laser welding Ti alloys with a pulsed laser source [92].

2.22.3 Porosity

Porosity refers to the gas pockets or voids of any solid material, frequently found in welds. Porosity (Figure 2.30) is caused when gas is released as the weld metal cools and its solubility is reduced, and from gases formed by chemical reactions in the weld. Porosity may be distributed uniformly throughout the weld, isolated in small areas, or concentrated at the root. Though in many cases, porosity is spherical, in some it is wormhole shaped, and elongated in the solidification direction of the weld metal [93].

In laser welding, when the beam density exceeds a threshold, typically around $10^6 W/cm^2$, a small vapor cavity, frequently referred to the keyhole, filled with high temperature metallic vapor, or plasma will be formed due to the evaporation of the material. Typically, the keyhole periodically oscillates throughout the welding process and leads to porosity defects in the final welds, especially in the case of partial penetration laser welding. Large porosity defects can significantly deteriorate some of the mechanical properties of the welds, such as the tensile and fatigue strength. The process of keyhole instability and the formation process of keyhole-induced porosity have been studied by many researchers [94,95,96].

It was found that during deep penetration laser welding, gas bubbles intermittently form from the tip of the oscillating keyhole, and most of them are captured by the solidification front, and then become pores in a very short time [94]. The chemical content of the gas in the pores was also studied and these experiments proved that this gas was the shielding gas [95]. The average size and amount of porosity decreased for higher laser power, mainly due to the variation in power density. High power density is an important factor for achieving and maintaining the keyhole mode of welding. Therefore, during the laser welding, a relatively more stable keyhole formed, resulted in less and finer porosity [96].

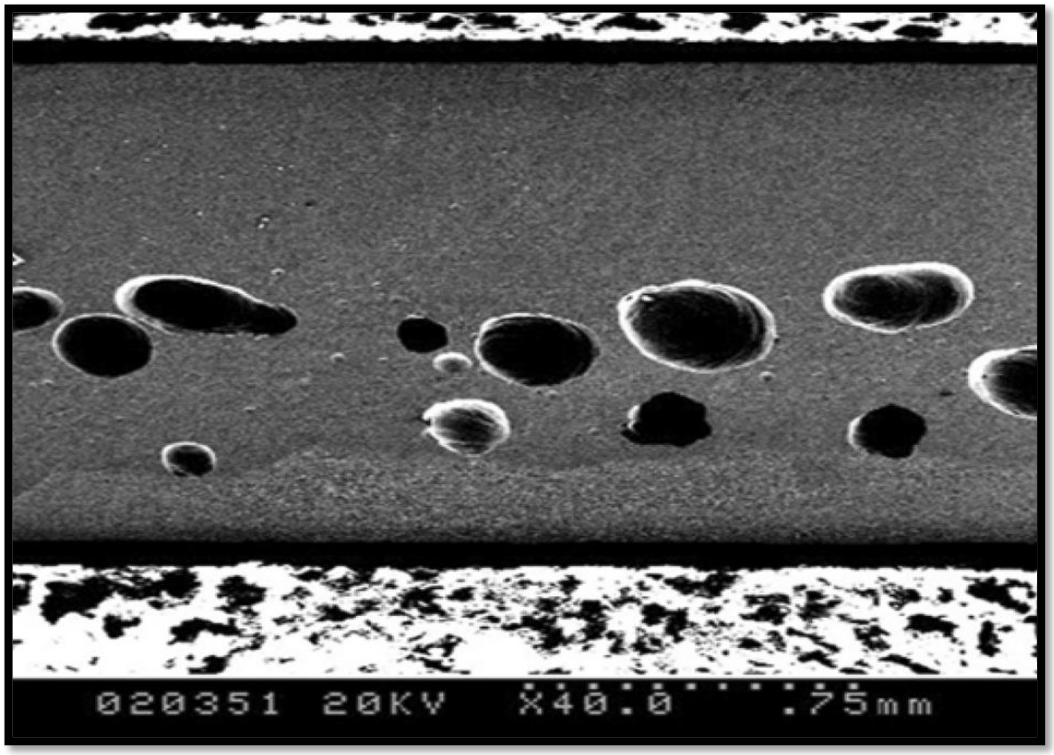

Figure (2.30): Pores in the Ti alloys welded by laser welding [94].

2.22.4 Undercut

Undercuts typically occur as a result of the displacement or expulsion of the metal from the weld pool due to the high welding energy density, which affect the quality of the weld and cause the concentration of stresses. It is a common welding defect that can appear continually or intermittently, specifically when welding at a high speed. In general, the welding speed is reduced, to reduce or avoid the undercut, which would greatly improve the fatigue properties of the welds. The undercut is one of the complex welding defects, which occurs for several reasons, and depends mainly on the metal flow mechanism and temperature. Figure (2.31) shows three types of undercut formed by the laser welding method. Due to reduced wetting, the curved undercut is increasingly created at faster welding rates [97,128], with the temperature gradients between the melt and solid being thought to be the determining factor.

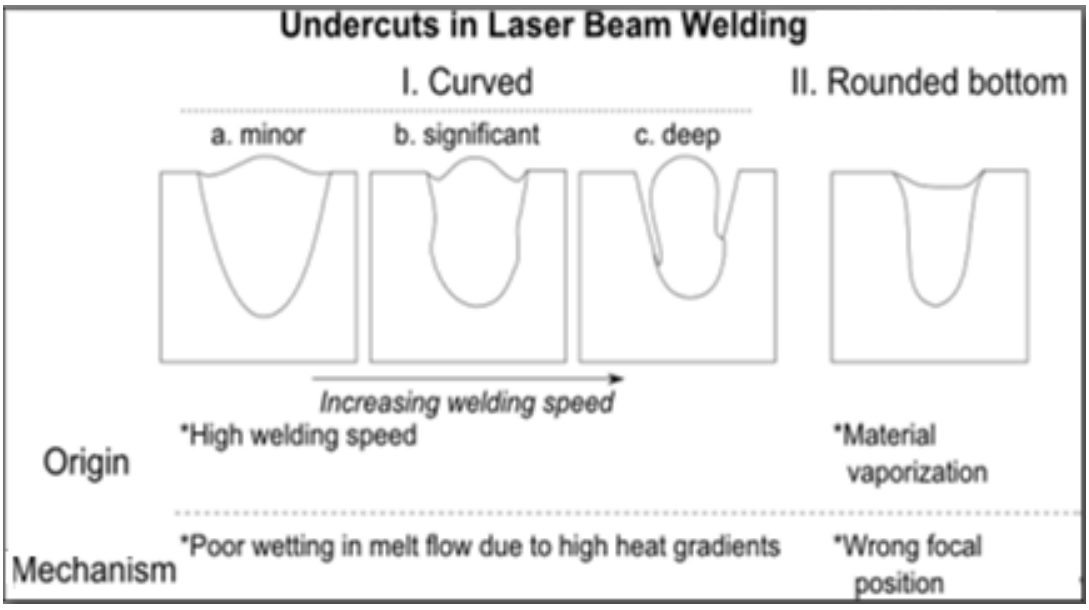

Figure (2.31): Different types of undercuts in laser beam welding [98].

2.23.5 Spatter

Spatter is a common defect in welding processes that affects the quality of the weld. It is defined as melt droplets scattered from the weld pool, adhered and hardened to the workpiece surfaces and along the weld joint [99]. In general, laser welding is a process of heating and cooling materials at a high speed, resulting in a narrow weld pool. The molten pool close to the keyhole wall has an upward slope due to the effect played by the recoil pressure. One of the variables that leads to the development of spatter is the low surface tension of the molten metal in the area around the keyhole. The melting upward around the keyhole is accelerated by the recoil pressure caused by evaporation and the shear tension caused by the movement of the metal vapor. Spatter decreases as welding speed is raised because of lower heat input, which reduces the downward upward momentum of the molten metal around the keyhole, as shown in Figure (2.32). Keyhole stability thus results in spatter suppression [100].

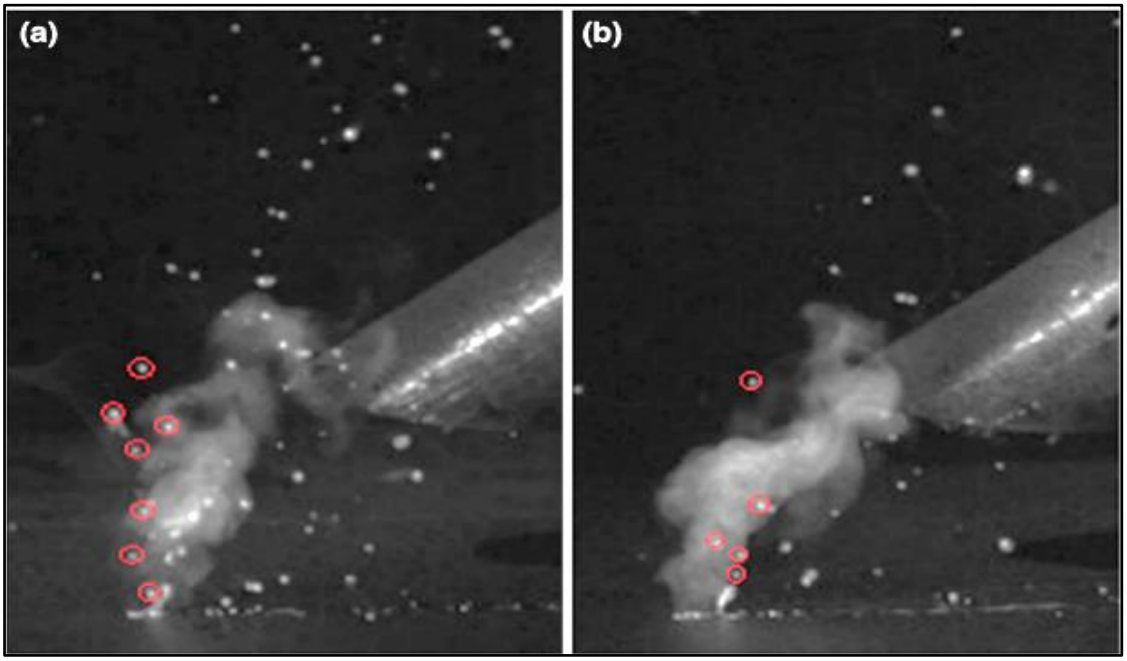

Figure (2.32): Spatter at different welding speeds (a): low and (b): high speed [101].

2.22.6 Cracks

Cracks are breakage-type discontinuities that may occur in the weld itself or in the base metal adjacent to the weld. Severe restriction during shrinkage along with embrittlement or insufficient ductility of the base metal causes cracks to occur in the weld. Usually, this defect must be repaired, because of its great impact on the mechanical properties of welds [102].

Hot cracking of the type known as "solidification cracking" takes place as the weld pool solidifies. Ti alloys sometimes exhibit solidification cracking. At the end of solidification, cracks occur at the beta (BCC) SGBs, but during cooling, these boundaries change into alpha (HCP) [85]. A solidification crack along a prior beta grain boundary in the α–β Ti alloy (Ti–6Al–6V) is shown in Figure (2.33).

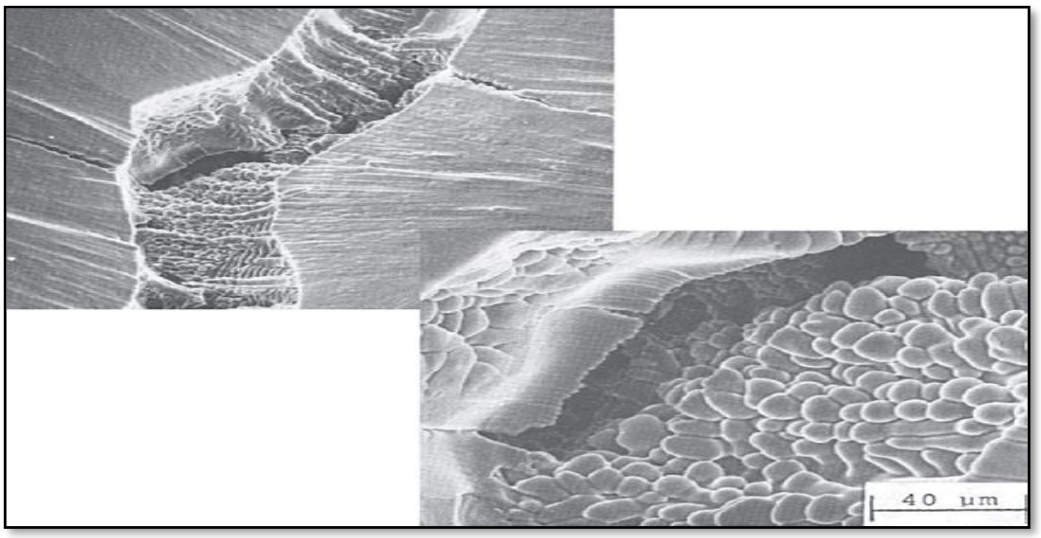

Figure (2.33): Solidification cracking generated in (Ti6Al-4V) alloy [85].

2.23 Literature Review

Various research studies have been conducted to determine if laser welding can be used to bond different grades of Ti alloys to each other, or to other materials. Industries nowadays are constantly competing to create goods that combine different types of minerals at the same time in order to take advantage of the composite qualities of the materials. By using this technology, the price of finished goods may also be reduced and the mechanical properties of welded joints improved.

- **Xinjin C. et al. (2009) [90],** studied the effect of welding speed on weld geometry, metallurgical characterization, mechanical properties and welding defects. The results found that the high-power Nd:YAG laser welding is a suitable approach for the Ti-6Al-4V alloy, with or without small cracks, porosity, and shape defects being generated. The main component of the FZ is acicular martensite, which results in an increase in hardness of about 20% when compared to that of the BM. It was also found that there is a gradient in the microstructure and hardness properties in the narrow HAZ because it contains a mixture of martensitic phases and primary α phases. The results also showed, compared with the BM, the

strength of laser-welded joints was close to or slightly greater, but the presence of fine pores and aluminum oxide impurities significantly reduced the ductility of the joints.

- **Duradundi S. et al. (2009) [104],** Investigated the effect of continuous Nd:YAG laser welding on the mechanical and metallurgical properties of the CP-Ti sheets of 1.6mm thick. The results showed that the decrease in the heat input led to a significant increase in the tensile strength, due to the increase in the cooling rate. It indicates that the increase in the cooling rate during welding with a decrease in heat input improves the relative elongation and thus increases the ductility of the weld, which improves the tensile properties.

- **In 2012, Mohammed J. T. el al. [105],** studied the effect of long-pulse Nd:YAG laser on the melt geometry of the CP-Ti with a thickness of 2.3mm. A welding machine used provides a 400watt pulsed laser for welding, a frequency of 15-45Hz, and a welding speed of 2-10mm/sec. Since the Ti metal tends to disperse when hot, the results showed that increasing the peak energy was not an effective way to increase the depth of penetration of Ti in keyhole cases. When welding Ti with a pulsed Nd:YAG laser, reducing welding speed leads to higher penetration due to a lower cooling rate, thus reducing scattering and porosity of the weld metal using the Nd:YAG pulsed laser method.

- **Squillace el al. (2012) [106],** analyzed the effect of welding process parameters on the metallurgical and mechanical properties of Ti6Al−4V sheets with a thickness of 1.6mm, using continuous Nd:YAG laser welding. The results proved that the hardness values graduated from the highest value in the weld area to the lowest value in the BM. The high

hardness of the WZ is due to presence of the martensite structure, which decreases while approaching the BM. The maximum hardness value was at the lowest heat input due to the high cooling rate. The tensile strength of the welds is close to or slightly lower than the BM, and this indicates the lack of defects and the high quality of the weld. The microstructure of the HAZ is a mixture of (ά) martensite, primary α and returned β.

- **Shailesh S. et al. (2014) [107],** investigated the effect of pulsed Nd:YAG laser welding process parameters for 3mm thick Ti6Al4V sheets. The results showed that the penetration depth depends mainly on the ratio between the pulse energy and the pulse width. Increasing the peak energy too much leads to form a crater, and higher hardness, but increasing the average power results in an increase in the total heat input and thus a decrease in the rate of cooling and hardness.

- **Giuseppe C. et al. (2015) [73],** studied the influence of different welding conditions (the power level was kept constant at 1.2kW, whereas the welding speed ranged between 1000 and 2500mm/min) on the bead morphology, metallurgy and mechanical properties. Full penetration welding of 2mm thick Ti6Al4V plates in butt configuration was performed by adopting a high brightness Yb fiber laser. Seam appearance and microstructures were assessed by optical microscopy, while the mechanical behavior was evaluated in terms of Vickers micro-hardness and tensile strength. Fracture surfaces were inspected by the SEM. The output showed that the higher linear energy promoted an X-shaped bead, whereas lower one promoted the formation of a V-shaped bead; the microstructural properties confirmed the formation of hard and brittle martensite structures in the FZ. The weld pool was efficiently shielded by adopting a reliable system of gas supply. Contaminations and oxidations were satisfactorily

prevented and ultimate tensile strength exceeded 80% of that of the BM. The formation of a hard and brittle phase reduced the elongation to 4–5%. The results account for a good weldability of Ti6Al4V alloy using a fiber laser.

- **Ahn J. et al. (2016) [74],** investigated the effect the fiber laser welding parameters on the weld geometry of the Ti6Al4V sheet, welding quality and the microstructure. The results showed that the weld penetration increases with the laser power or a decrease in welding speed. Low heat input resulted in fine acicular α` (martensite) in the FZ. The HAZ however, consists of acicular α`, primary α and intergrainular β due to the relatively lower cooling rate, whereas, increasing the heat input resulted in a coarse acicular α` in the FZ. The crater increases with increasing laser power or decreasing welding speed.

- **Chandan K. et al. (2017) [14]**, studied the effect of laser welding parameters on the weld geometry and the mechanical properties of the Ti-6Al-4V alloy having thickness of 5mm welded in butt configuration. The equipment used a 2kW fiber laser in CW mode integrated with computerized numerical control (CNC) workstation. It is observed that welding power and speed plays a major role for full penetration welding. In addition, welding power showed a direct effect whereas welding speed showed an inverse effect on the output responses. It is noticed that the hardness value of the FZ is higher than the HAZ and BM due to the difference in cooling rate during welding, which promotes the formation of α′ martensitic phase in the FZ.

- **Köse C. et al. (2017) [109],** studied the effect of the different welding speeds on the mechanical properties and microstructure of the (Ti-6Al-4V)

sheet by using the fiber laser method**.** It was observed that the tensile strength of the BM was higher than laser welded joints. Tensile strength of joints using low heat input was lower than using high heat input. The martensite phase formed in the FZ. Porosity was observed in the weld metal. The hardness increased with decreasing heat input.

- **Pramod K. et al. (2018) [84]**, investigated the effect of heat input in pulsed Nd:YAG laser welding of (Ti6Al4V) titanium alloy on microstructure and mechanical properties. The range of heat input various heat inputs (43.7–103.5 J/mm) have also been investigated. Microstructures of the fusion zone, HAZ and base material have been compared at various heat inputs using optical microscope and field emission scanning electron microscope (FESEM). The mechanical properties such as micro hardness and tensile strength of the welded joints at various heat inputs have been studied. Tensile tests of the welded specimen and base metal have been conducted for analyzing ultimate tensile strength and percentage elongation. Surface topography of the tensile fractured specimen of the welded joints and base metal has been examined to analyze the ductile and brittle behavior. EDS analyses of base metal and fusion zone of the welded specimen have been studied. XRD of the as-received base metal and welded specimen have been measured in the range of 30 to 85° to study the crystallographic structure. It was found that the increasing the heat input will increase the width of the FZ and the HAZ. The shape of the weld bead profile is T-shaped at low heat input and becomes approximately X-shaped at high heat input. The hardness of the FZ is higher than HAZ and the BM, due to the formation of ά martensite and increase in the size of the micropore.

- **Fedor F. et al. (2018) [111]**, investigated the microstructural variation of fiber laser beam-welded T-junctions between Ti-6Al-4V alloys and CP-Ti.

The results showed that the cooling rate was sufficient to produce martensite in the Ti-6Al4V part of the FZ. In contrast, the presence of martensite was not observed in the CP-Ti part due to the lower solute content and thus the much higher critical cooling rate.

- **Ruifeng Li et al. (2019) [110]**, analyzed the effect of the laser beam and laser-MIG hybrid welding processes on the strengthening mechanism of 4.2mm thick CP-Ti plates. The results found that the FZ and the HAZ contain coarsened and elongated α grains, acicular α phase and twined grains in both welded joints. The laser beam welded joints featured a higher tensile strength than the laser-MIG hybrid welding process.

- **Muralimohan C. et al (2019) [12],** investigated the effect of process parameters and heat input on weld bead geometry of laser welded Ti-6Al-4V alloy. The laser power of (1 to 1.5kW) and (5 to 9m/min) welding speed were used. The results showed that the width and depth of the FZ varied with welding conditions. The sizes and widths of the grains in the FZ and HAZ varied greatly with the change in welding speed and laser power. The best mechanical properties and the optimum weld bead geometry of the weld joint were produced by controlling the welding conditions.

- **Ahmad C. et al. (2020) [112],** analyzed the microstructure, microhardness, tensile properties and fracture characteristics of the laser welded Ti–10V–2Fe–3Al (Ti1023) titanium alloy. A CW fiber laser was used for the butt-welding of 1.6mm thick sheets. Welding was performed at a power of 1.2kW, a constant welding speed of 150cm/min. Beam diameter at the focus spot was 0.28mm, and the focal point was situated 2mm below the top surface of the sheets to obtain an adequate power density. Results indicated that the mechanical properties were related to the microstructure

development across the weld. In the BM, the primary α phase with spherical and lath morphologies appeared. The volume fraction of the α phase in the HAZ decreased to some extent compared to the BM as a result of its partial dissolution and/or transformation to the β phase. In the FZ, primary α phase was completely transformed to the β phase. The BM exhibited a higher hardness than the HAZ and FZ due to a higher volume fraction of the primary α phase, which is harder than β phase. For the same reason, the yield strength (YS) and UTS of the weldments were somewhat lower than those of the BM. In addition, the presence of porosity, undercut, concavity and coarse columnar β grains in the FZ contributed to lower YS, UTS and total elongation in the weldments in comparison to the BM. Examination of the fracture surface of the weldment tensile samples indicated a mixed brittle and ductile fracture mode.

- **Na Qi et al. (2020) [114],** analyzed the effect of laser power on tensile performance of Ti-6Al-2Zr-1Mo-1V (TA15) laser-welded bottom locked joint. The laser welding speed was constant and the laser power was (1000W, 1300W and 1600W) respectively. Significantly, increasing the laser power leads to an increase in FZ and HAZ width. The HAZ microstructure was relatively complicated, mainly composed of martensite ά, acicular α structure and β. The amount of martensite formed at the highest laser power was small, while the lowest laser power produced a large amount of martensite ά, due to the higher cooling rate. All the specimens fractured near the HAZ, and the fracture was ductile in the shape of dimples. The tensile strength of the welded joint decreased with the increase of laser power. When the laser power was 1.0kW, 1.3kW and 1.6kW, the tensile strength was 723MPa, 705MPa and 695MPa respectively, which was 64.55%, 62.95% and 62.05% of the BM strength.

- **Alireza A. et al. (2020) [115],** investigated the effect of the Nd:YAG laser welding on the microstructure and mechanical properties of the Ti-6Al-4Vand CP-Ti dissimilar and similar joints of 3mm thick. The defects found were porosity and lack of filling, whereas indications of lack of penetration or cracks were not observed in all weld joints. The fracture in all welds of the Ti6Al4V was from the FZ.

2.23.1 Studies Closer to the Current Research

I	Author and (Year)	Experimental Range	Results
1	Xianguo Li .et al. (2005)	The BM used is CP-Ti sheets with a thickness of 0.5mm, and the welding parameters are the pulse width of 4.5ms, pulse frequency of 5Hz, welding speed of 0.4mm/s and average power of 22-23W. Weld surface discoloration is verified by visual inspection.	The results showed that the color of the weld surface changed from silver to blue due to increasing the oxygen percentage in the covering gases, and led to an increase in hardness. The welding strength increased first and then decreased due to the presence of an acicular α microstructure.
2	Mohammed J. et al. (2012)	The metal used is CP-Ti plates with a thickness of 2.3mm, pulse welded by Nd:YAG laser at peak power of 1.5kW and various welding speeds (4- 5.7mm/s)	The results showed that increasing the penetration depth by increasing the peak power is not suitable in the case of keyhole due to the increased scattering of Ti in the molten state. The use of welding speed is better to improve welding penetration and reduce scattering and porosity.
3	Giuseppe C. et al. (2015)	Ti-6Al-4V of 2mm thick plates were welded with a high Yb fiber laser. Welding speed varied at 1, 2, 2.5 and 5m/min, with a laser power of 1.2kW.	The development of an X-shaped bead was favored by higher linear energy, while the production of a V-shaped bead was favored by lower linear energy. The production of hard and brittle martensitic structures in the FZ was confirmed. The mean UTS of the FZ exceeded 80% of the BM. Elongation reduced to 4-5% after the creation of a brittle phase.

4	Fedor F. et al. (2018)	Various Ti alloys have been fiber laser welded in 0.8mm thick dissimilar T joints. The skin material was CP-Ti, while the stringer material was Ti-6Al-4V alloy. The welding power was 650W and the welding speed was 3.5m/min.	The results showed that the cooling rate was sufficient to produce martensite in the Ti-6Al4V part of the FZ. In contrast, the presence of martensite was not observed in the CP-Ti due to the lower solute content and thus the much higher critical cooling rate.
5	Ahmad C. et al. (2020)	A CW fiber was used for butt-welding of 1.6mm thick plates of the Ti–10V–2Fe–3Al beta alloy. Laser power of 1.2kW and a constant welding speed of 150cm/min were used. The diameter of the beam at the focus point was 0.28mm.	The structure of FZ was of coarse and columnar beta grains. The martensite phase or the α phase was not observed due to the high cooling rate and the high percentage of beta phase stabilizers such as V and Fe. Hardness in the BM was higher than the HAZ and FZ due to a larger amount of the α phase in the BM. Porosity and crater were observed in all samples; the fracture occurred in the FZ.
6	Na Qi et al. (2020)	The metal used was TA15 alloy. The bottom locked joint was welded with fiber laser of variable thicknesses (1.5 and 2mm). The welding speed was constant and the laser power was 1.0, 1.3 and 1.6kW.	Significantly, increasing the laser power led to an increase in FZ and HAZ width. The HAZ microstructure was mainly composed of martensite, acicular α and β structure. The amount of martensite formed at the highest laser power was small, while the lowest laser power produced a larger amount of martensite due to the high cooling rate. All the specimens fractured near the HAZ, and the fracture was a dimple ductile. The tensile strength of welded joint decreased with increasing the laser power. Samples welded with low laser energy had higher tensile strength due to high cooling rate.
7	Alireza A. et al. (2020)	3mm thick CP-Ti and Ti-6Al-4V alloy plates were welded by fiber laser method. The welding parameters used were the laser power of (3-4kW) and welding speed of (1.69-2.25m/min).	The defects observed in the weld joints were porosity and underfill; there were no indications of a lack of penetration. The place of failure of the asymmetric samples was in the FZ, while the identical samples of the CP-Ti fractured from the BM.

After reviewing the previous literature, it was found that some researches were confined to the use of certain laser welding methods, some of which are outdated, and some are not automated. Other literature has dealt with the use of variables with limited ranges, due to the limitations of the laser

machines used. Moreover, some studies were confined to a limited thickness of the base metal as a result of the limited laser power available.

As of the time of this writing, no comprehensive study has been found by the researcher to investigate the effect of using efficient and diverse laser welding methods on various types of industrially common Ti alloys. Additionally, no research has been novated to analyze the influence of the most effective variables of these methods with wide ranges on the Ti alloy welds with relatively thick plates, and compare them in terms of the microstructure, mechanical properties, weld geometry, penetration, joint efficiency and potentially defects, using several examinations.

Chapter Tree

Experimental Part

CHAPTER THREE: EXPERIMENTAL PART

3.1 Introduction

This chapter gives a detailed picture of the experimental work and explains all of the conditions under which the tests were conducted. It comprises the materials, equipment and experimental techniques utilized in this work, which include Nd:YAG laser and fiber laser welding of CP-Ti and Ti-6Al-4V alloy plates. Microhardness and tensile tests were used to study the mechanical properties of the weld joints. The changes in microstructure of the weld joint were evaluated by the optical microscope (OM), scanning electron microscope (SEM) and energy dispersive spectrometer (EDS). X-ray radiography was used to detect internal flaws in the weld joints, in addition to visual examination of tensile test specimens after fracture.

3.2 Program of the Current Study

The general program structure employed in this study is shown in Figure (3.1).

3.3 Workpiece Materials

The materials used are grade 5 (Ti-6Al-4V) and grade 2 (CP-Ti) alloy sheets with the dimensions of (50×35×3)mm. Tables (3.1) and (3.2) show the chemical composition and mechanical properties of the materials respectively according to American Society for Testing and Materials (ASTM). The chemical composition analysis for materials was achieved by Niko Pajohan Tafsir in Tehran-Iran. The EDS test was carried out to validate the chemical composition of the alloys used in Al-Razi Labs/Iran.

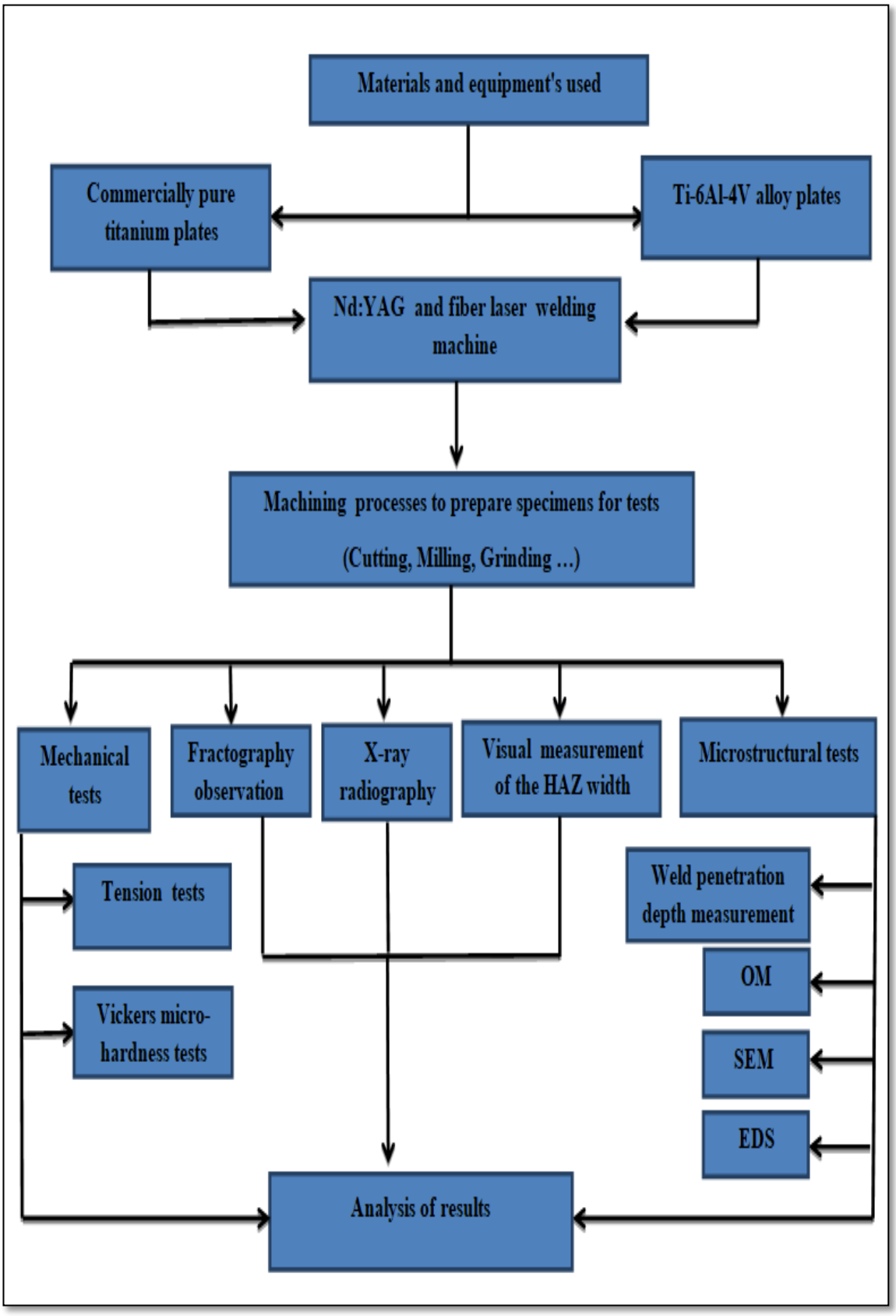

Figure (3.1): Flow Chart of the present work.

Table (3.1): Chemical composition of the CP-Ti (grade 2) and Ti6Al-4V (grade 5) alloy plates used in this study.

Materials	Chemical Composition-wt%								Residual Elements
	Ti	Al	Fe	C	O	H	N	V	
Grade 2-CP-Ti (Nominal)	R	-	Max-0.3	Max-0.08	Max-0.25	Max-0.015	Max-0.03	-	Total Max-0.4
Actual	R	-	0.05	0.012	0.092	0.001	0.018	-	Total <0.4
Grade 5 Ti-6Al-4V (Nominal)	R	5.5-6.7	0.4	0.08	-	-	-	3.5-4.5	Total ≤0.4
Actual	R	5.8	0.05	0.01	0.06	0.001	0.009	4.13	Total <0.4

* R-Remainder

Table (3.2): Mechanical properties of Ti alloy plates used in this study.

Materials	Yield strength 0.2% (Mpa)	Tensile Strength (Mpa)	Elongation %	Vickers Hardness Kg/mm^2
CP-Ti (Nominal)	275 Min.	345 Min.	20 Min.	145
Actual	592	750	-	149
Ti-6Al-4V (Nominal)	830 Min.	950 Min.	11 Min.	396
Actual	1593	1840	-	339

3.4 Laser Welding Machines

An IQL-10, Nd:YAG pulsed laser with a maximum average power of 400W (Figure 3.2) was employed in this investigation, along with high-speed imaging. The laser's standard output was square-shaped pulses. The laser parameters have ranges of 1–999Hz for pulse frequency, 0.2–20ms for pulse duration, and 0–40J for pulse energy. The pulse energy and repetition rate have to be chosen in such a way that the average power does not surpass the laser's maximum capability (400W). The studies were carried out with 10Hz frequencies and 3–6mm/s workpiece speeds. Two lenses with a focal length of 150mm and a minimum spot size of 250µm

made up the focusing optical system. YFL-1500, a single mode CW fiber laser (Figure 3.3), with a maximum power of 1500W, a wave length of 1080nm, workpiece speeds of 2–30mm/s and a Gaussian beam profile was also used. The focusing optical system has a focal length of 150mm and a minimum laser spot size of 200μm. In this experiment, the laser power should be between 600 and 1500W. Table (3.3) shows the capacity of the welding machines and welding parameters used in the current study. All experiments were carried out in the Iranian National Laser Center-Tehran.

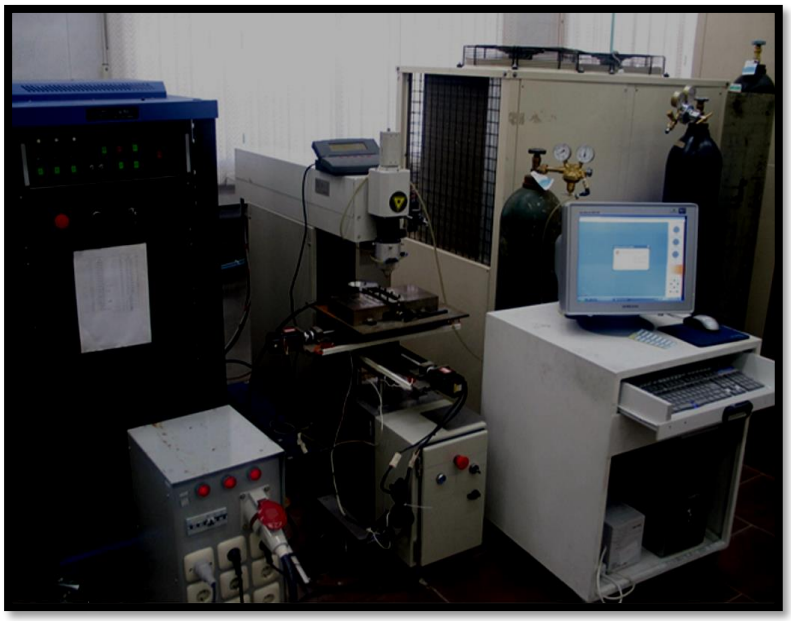

Figure (3.2): Nd:YAG laser welding systems.

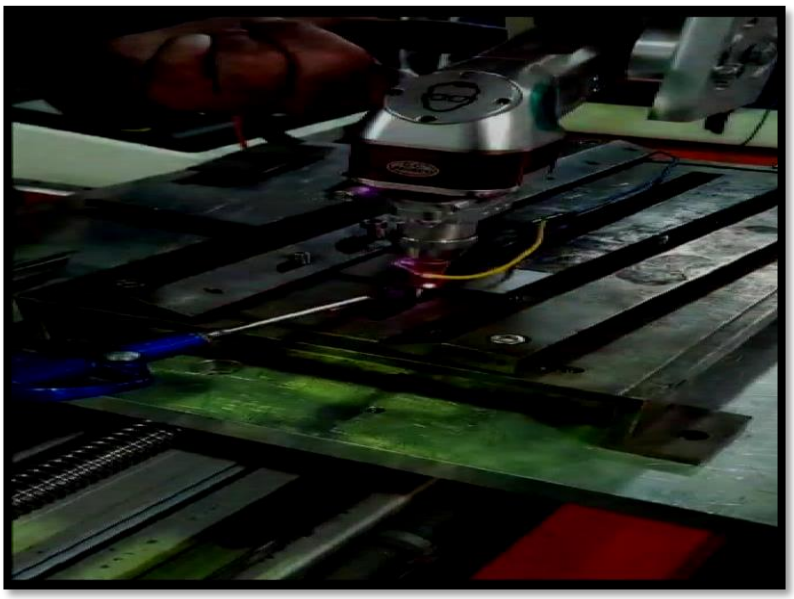

Figure (3.3): Fiber laser machine

Table (3.3): The capacity of welding machines and parameters used in laser welding of the (CP-Ti) and (Ti-6Al-4V) alloy plates.

Type of welding Machine	Machine parameters		Welding parameters used in the study
Nd:YAG Pulsed laser machine (IQL-10)	**Pulse energy**	0-40J	15, 17, 18.5 and 19.7J
	Pulse frequency	1-999Hz	10Hz
	Pulse duration	0.2-20ms	8ms
	Focal length	150mm	150mm
	Welding speed	-	3, 4, 5 and 6mm/s
Fiber laser machine (YFL-1500)	**Power laser**	1500W	600, 900, 1200 and 1500W
	Welding speed	2-30mm/s	10, 15, 20 and 25mm/s
	Focal length	150mm	150mm

3.5 Laser Welding of Titanium Alloys

The joint design used in laser welding for both types of base material (CP-Ti and Ti-6Al-4V) was a square butt. To prevent oxidation, an incidence angle of 45° with a 99.9% purity argon as a shielding gas with a flow rate of 10 lit/min was used for all welds. Moreover, the laser beam was fired at an angle of 90° relative to the weld line. Figure (3.4) shows the design and fit-up of the weld joint.

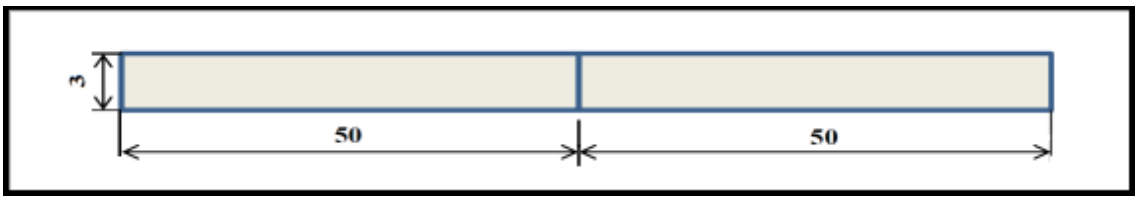

Figure (3.4): Dimensions of plates to be joined (in millimeters).

Before welding process, the following steps were carefully performed.

1- Removing oils, grease and others contaminants from the surfaces of the plates to be welded using ethanol alcohol.

2- Fixing the plates on the laser welding machine, and adjusting the spacing between them to 0mm.
3- Fiber laser and Nd:YAG laser welding the set-up along 35mm in a subsidiary of the Iranian National Center, according to the conditions described in Tables (3.4) and (3.5) below.

Figure (3.5) shows the samples joined by fiber and Nd:YAG laser welding processes.

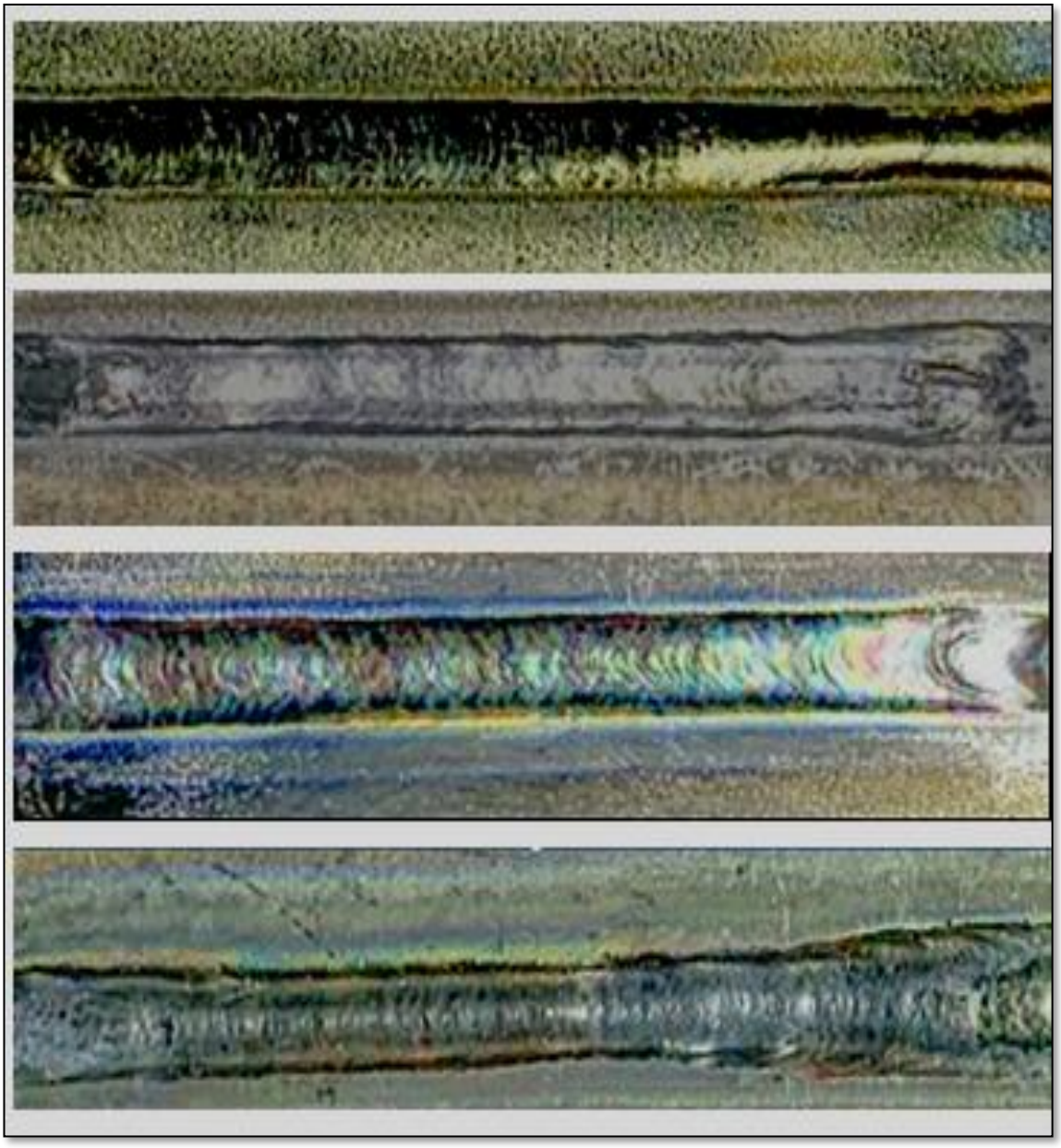

Figure (3.5): Some of the Ti alloy welds before manufacturing of test specimens.

Table (3.4): Conditions for fiber laser welding.

Sample	Laser power (kW)	Welding speed (mm/s)	Heat input (kJ/mm)
A1,B1	0.6	10	0.06
A2,B2	0.9		0.09
A3,B3	1.2		0.12
A4,B4	1.5		0.15
A5,B5	0.6	15	0.04
A6,B6	0.9		0.06
A7,B7	1.2		0.08
A8,B8	1.5		0.1
A9, B9	0.6	20	0.03
A10,B10	0.9		0.045
A11,B11	1.2		0.06
A12,B12	1.5		0.075
A13,B13	0.6	25	0.024
A14,B14	0.9		0.036
A15,B15	1.2		0.048
A16,B16	1.5		0.06

A: for Grade 2, B: for Grade 5.

Table (3.5): Conditions for the Nd:YAG Laser Welding.

Sample	Peak power (kW)	Welding speed (mm/s)	Heat input (KJ/mm)
A17,B17	1.9	3	0.51
A18,B18	2.12		0.54
A19,B19	2.3		0.61
A20,B20	2.5		0.67
A21,B21	1.9	4	0.38
A22,B22	2.12		0.42
A23,B23	2.3		0.46
A24,B24	2.5		0.50

A25,B25	1.9	5	0.304
A26,B26	2.12		0.34
A27,B27	2.3		0.37
A28,B28	2.5		0.40
A29,B29	1.9	6	0.253
A30,B30	2.12		0.28
A31,B31	2.3		0.31
A32, B32	2.5		0.33

A: for Grade 2, B: for Grade 5.

3.6 X-ray Radiography

X-ray radiography is one of the significant non-destructive tests employed for welded parts to detect internal defects formed in welds that affect the quality of the welds such as cracks, pores and inclusions. This test was performed on the welded samples before manufacturing of the test specimens. Defects can be easily distinguished by the contrast in the image formed on the film. Areas that do not absorb radiation energy are dark, but those that absorb a small part of the radiation appear less dark. This inspection must be done by specialists in this field. Figure (3.6) presents the device used for inspection in Niko Pajohan Tafsir labs in Tehran/Iran..

Figure (3.6): Portable X-Ray inspection machine.

3.7 Measuring the Heat Affected Zone Width

For fiber and Nd:YAG laser butt weld samples, the HAZ widths and profiles were determined by measuring the distance between the visible HAZ edge and the weld centerline by a 5mm intervals. The measurements were made on the welded samples before manufacturing specimens for tests.

3.8 Preparation of Test Specimens

After the non–destructive examinations, specimens were manufactured from the welded samples shown in Figure (3.5) for microhardness, tensile, micrography (OM and SEM) tests, based on the ASTM specifications. Below are the most important procedures followed for manufacturing the test specimens.

1- To make weldments easier to process on the milling machine, a fixed head grinding machine was used to roughly straighten the weld zone (weld line) with the weldment surfaces.
2- The top and bottom surfaces of the weldments were slightly milled.
3- On one of the two weldment surfaces, the dimensions of the required specimens were marked.
4- A wire electro-discharge machining (W-EDM) was used to precisely cut the weldments according to the marking (Figure 3.7).

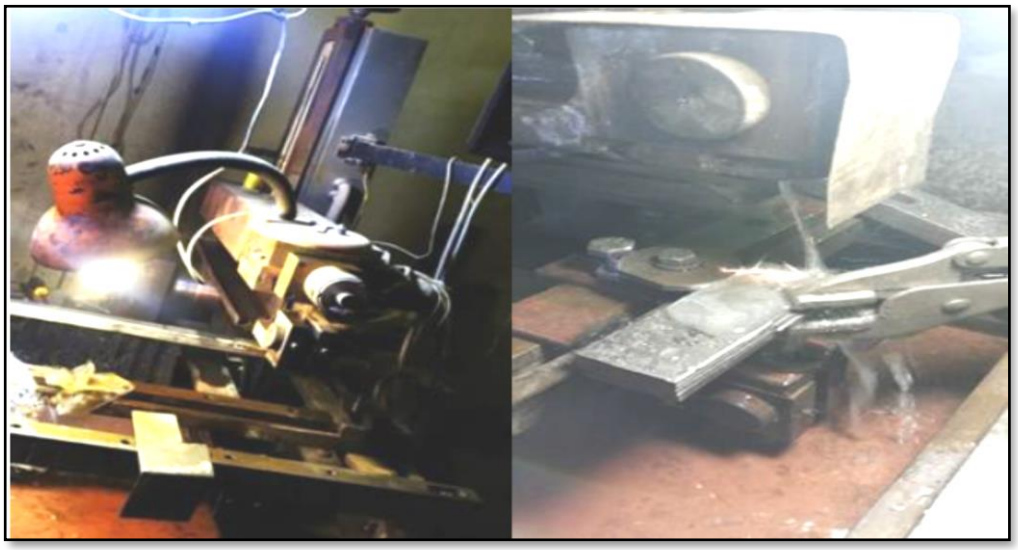

Figure (3.7): Wire electro-discharge machining cut.

3.9 Microscopy Test

3.9.1 Weld Penetration Depth Measurement

The purpose of this test is to know the effect of welding parameters such as laser power and speed on the depth of the weld penetration. The test was performed according to ASTM E 883-2017 within the scope of the ISO/IEC 17025 standard using the optical microscope (Figure 3.8). This test was permormed at Al-Razi Metallurgical Research Center in Tehran.

Figure (3.8): Optical microscope.

3.9.2 Metallurgical Examination

Standard metallographic techniques were used to prepare specimens for microstructural examination, which included the following steps.

1- To enable handling and thus reveal microstructural changes in different zones, specimens were W-EDM cut to a suitable size.

2- The wet grinding was carried out by exposing the specimen surface to an electrically powered rotary disk while using (SiC) emery sheets of various grades in a sequential order (400, 600, 800, 1000, 1200, 1500 and 2000). After that, the specimen was washed with water and dried with hot air.

3- Mechanical polishing was utilized to remove the new finer scratches generated by the grinding process, using diamond particle pastes. Polishing was accomplished by sequentially applying 6, 1, and 0.25µm pastes to specific clothes mounted on the rotating disk.

4- Etching with Keller's reagent (85ml H_2O+10ml HNO_3+5ml HF) was used as an etchant to reveal the phases by its chemical effect on the different phases in variable levels. Following the etching, the prepared surface to be examined was cleaned with alcohol.

The microstructure and topography of several zones on the prepared specimen surfaces across the centerline of the welds (FZ, HAZ and BM) were then defined using an OM. It was also utilized to identify the kind, size, and location of any surface flaws throughout the welds. This test was carried out at Tehran's Al-Razi Metallurgical Research Center.

3.9.3 Scanning Electron Microscopy (SEM)

Microstructural exams and chemical composition analyses were carried out at Al-Razi Metallurgical Research Center in Tehran utilizing an SEM and an EDS. For all prepared specimens, SEM images were collected in order to clearly analyze the microstructure with higher accuracy. The specimens were prepared with appropriate grinding papers, polished, and then etched with Keller's reagent solution in the same way that welds were inspected optically. The FZ, HAZ, and BM were all investigated across the weld centerline. The EDS was used to analyze the chemical composition of the BM. Figure (3.9) shows the SEM device.

Figure (3.9): Scanning electron microscopic device.

3.10 Mechanical Tests

3.10.1 Microhardness Test

Microhardness test was achieved using digital Vickers microhardness tester (Figure 3.10) according to ASTM E 384-17. The indenter is a square-based pyramidal shape diamond with face angles of 136º. Measurements were done across the weld centerline on both sides of the welds (FZ, HAZ and unaffected BM) after grinding process of the surfaces to be measured. This test was done with a load of 300g and a loading time of 10-15sec. The measurement point distribution was by 0.25mm intervals across the welds, with an average of two lines located at the top and bottom of the surfaces to be measured shown in Figure (3.11). This test was done at Al-Razi Metallurgical Research Center in Tehran.

Figure (3.10): Vickers microhardness device.

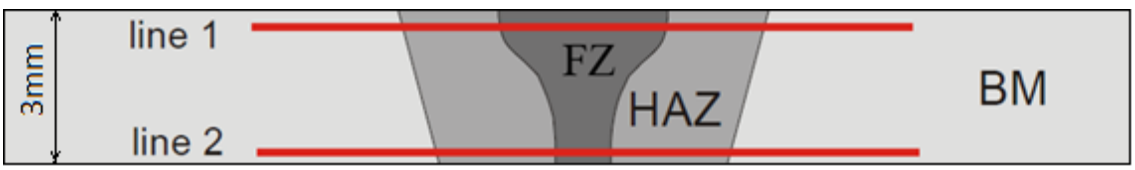

Figure (3.11): Locations of hardness measuring along the cross-section of the weld.

3.10.2 Tension Test

The shape and dimensions of the tensile test specimen employed are shown in Figure (3.12). The W-EDM cut was used to manufacture the specimens as shown in Figure (3.13). The weld's centerline was in the middle of the specimen, and the tensile strength was an average of two. The test was performed at the labs of the Material Department-Faculty of Engineering-University of Kufa using a universal type device WAW-200 (Figure 3.14) according to ATSM E8/E8M13a at a speed of 1 mm/min.

G=50, W=6, L=100, C=10, R=6, B=30, A=32, T=3

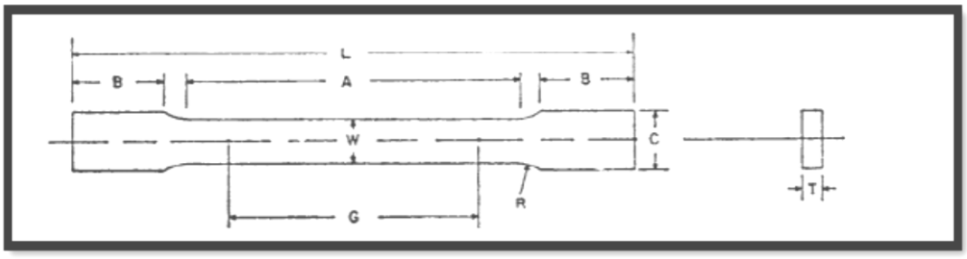

Figure (3.12): Shape and dimensions of the tensile test specimen (dimensions in mm).

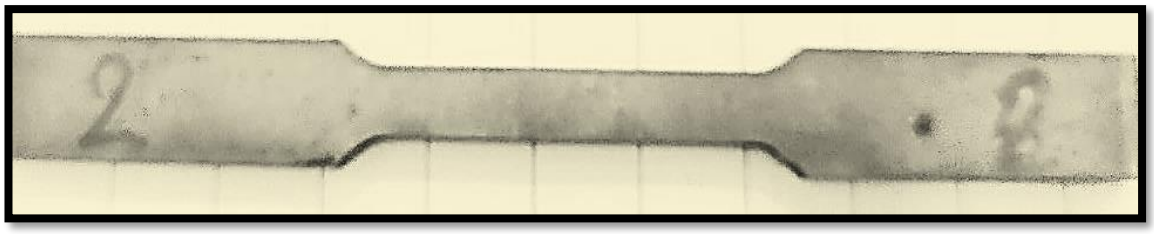

Figure (3.13): One of the manufactured tensile test specimens.

3.11 Fractography Observation

This test was carried out on the tensile specimens after fracture. The purpose of this test is to determine the kind, size and position of probable flaws such as inclusions, pores and cracks that are visible to the human eye. The fracture mode was also specified by this test before photographed.

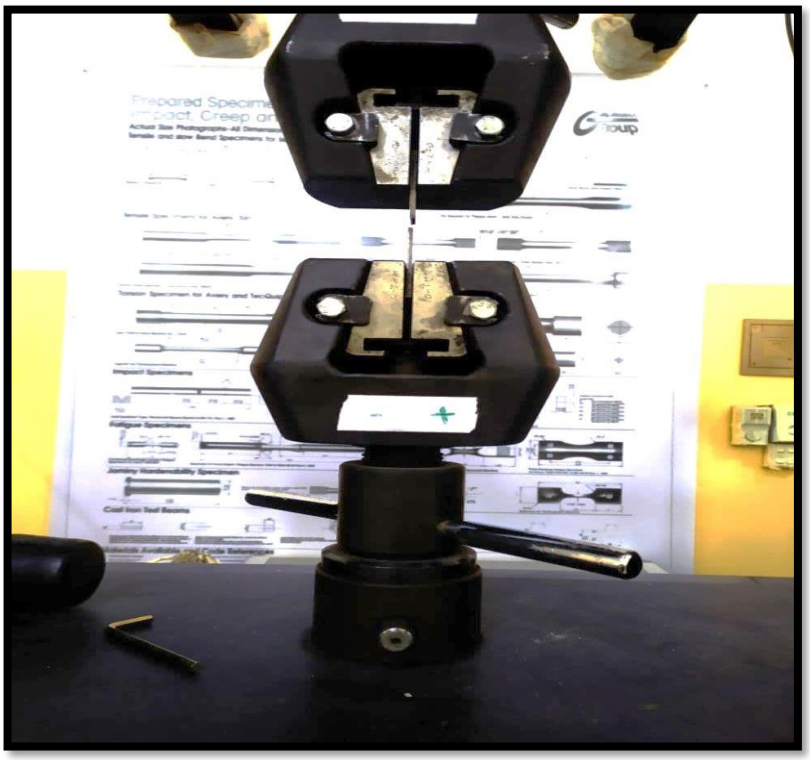

Figure (3.14): Tensile test device.

Chapter Four

Results and Discussion

CHAPTER FOUR: RESULTS and DISCUSSION

4.1 Introduction

This chapter shows results of the practical part tests, including the results of measuring the depth of weld penetration and the microstructure using OM with the help of SEM. In addition, the results of mechanical tests (hardness test and tensile) for similar joints welded by fiber and Nd:YAG laser welding have been presented and discussed. The fracture surface, and internal defects of the welds revealed by X-ray radiography were also discussed.

4.2 X-Ray Radiography

An X-ray inspection was performed on 64 samples welded using fiber and Nd:YAG laser processes of CP-Ti and Ti-6Al-4V plates before cutting and preparing the specimens for future tests.

Figure (4.1a) displays X-ray radiographs of CP-Ti samples welded using a fiber laser. It was noted from the figure that there is a lack of weld penetration in A1 and A2 samples due to the lower laser power used with these samples. The laser power of (0.6 and 0.9kW) was not high enough for obtaining complete penetration at the welding speed of 10mm/s, due to the low heat input induced from the laser power and welding speed used. When the laser power was increased to (1.2 and 1.5kW), and the welding speed was fixed at 10mm/s, an increase in the weld penetration depth was observed as a result of the increased heat input, as for A3 and A4 samples. Figure (4.1a) also shows a lack in the weld penetration depth when the welding speed was increased from 10 mm/s to 15, 20, and 25mm/s at laser power of 1.5kW as in A8, A12 and A16 samples respectively. As well

known, increasing the welding speed reduces heat input, and is therefore insufficient to obtain complete penetration. It was also observed that A4 sample exhibited the best penetration over the welds; A12 sample, despite using higher welding speed, presented good penetration. This is due to the high laser power utilized with these samples; this agrees with [116]. Moreover, it can be seen from the figure that some samples contain a number of pores at the FZ or near the FZ (FZ/HAZ interface). Low laser powers cause the gases to remain trapped in the molten metal, and not be able to escape to the surface before the metal solidifies. This is due to the high cooling rates caused by the low heat input. Porosity was also observed when the laser power was increased to 1.2 and 1.5kW due to the turbulence in the flow of molten metal which leads to keyhole breakdown [117], as in A3 and A4 samples joined at a welding speed of 10mm/sec. Porosity in A7, A8 and A12 samples, probably formed due to the increase in the welding speed from 10 to 15 and 20mm/s. Increasing the welding speed reduces the heat input, and thus leads to an increase in the cooling rate, and the lack of sufficient time for the gases to escape [117]. It was also noted that there are no cracks in the welded samples. This could be attributed to the nature of the crack-resistant metal.

Figure (4.1b) shows X-ray radiographs of the Ti-6Al-4V samples welded using a fiber laser. It was noticed that there is a decrease in welding penetration in samples B1 and B2 joined at a relatively low laser power of 0.6 and 0.9kW respectively, and at a welding speed of 10mm/s. The weld penetration increased with increasing the laser power to 1.2 and 1.5kW, and welding speed of 10mm/s as in B3, B4 samples respectively.

Figure (4.1b) also shows that the weld penetration depth decreased with increasing welding speed to 15, 20 and 25mm/s, due to decreasing the heat input, as in samples B5 up to B16. Better weld penetration was obtained in samples B4 and B12 having a laser power of 1.5kW and a welding speed

of 10 and 20mm/s respectively. Porosity was also observed in some samples at the FZ and FZ/HAZ interface, for the same reasons mentioned previously with fiber laser welding of the CP-Ti.

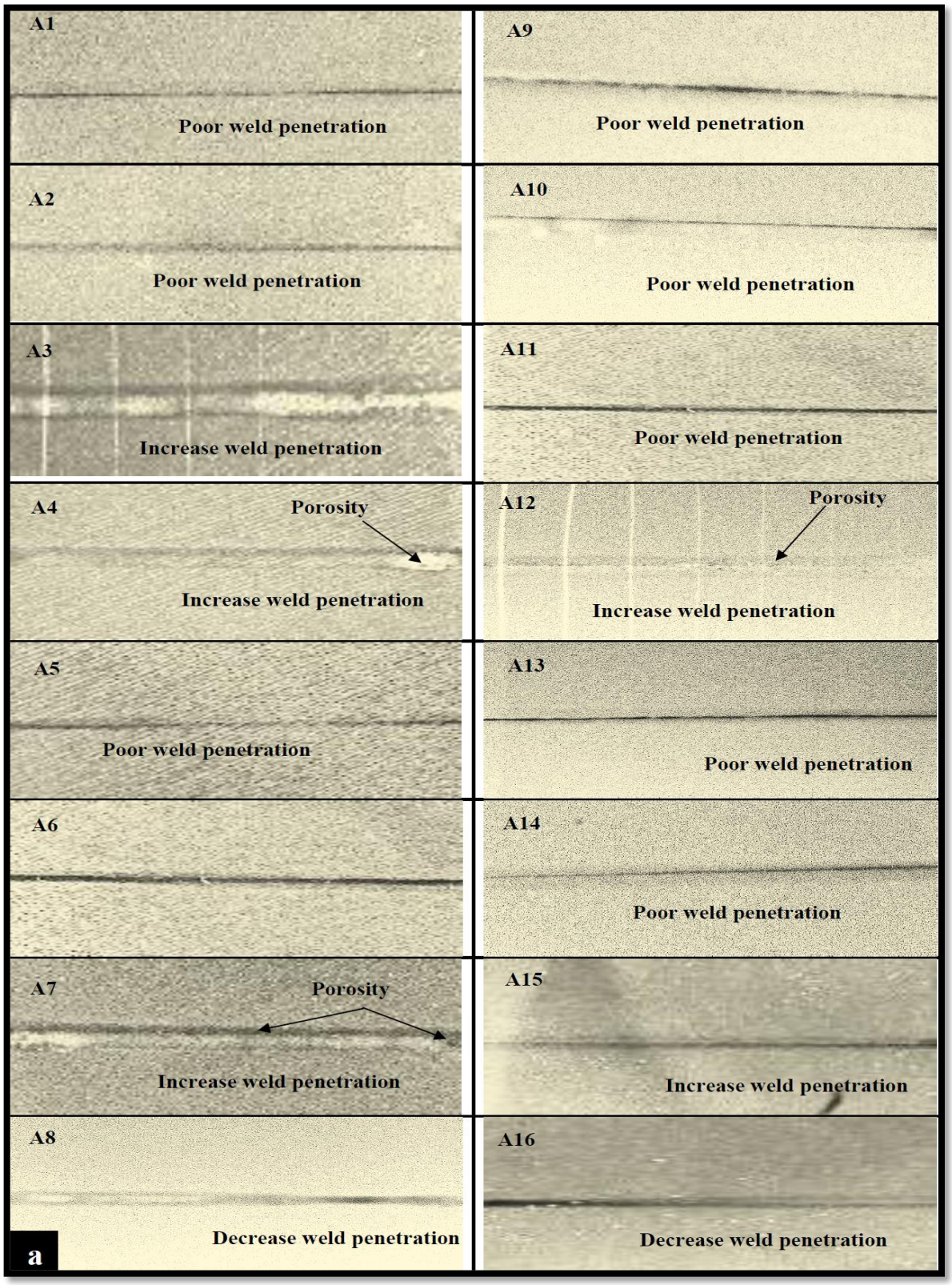

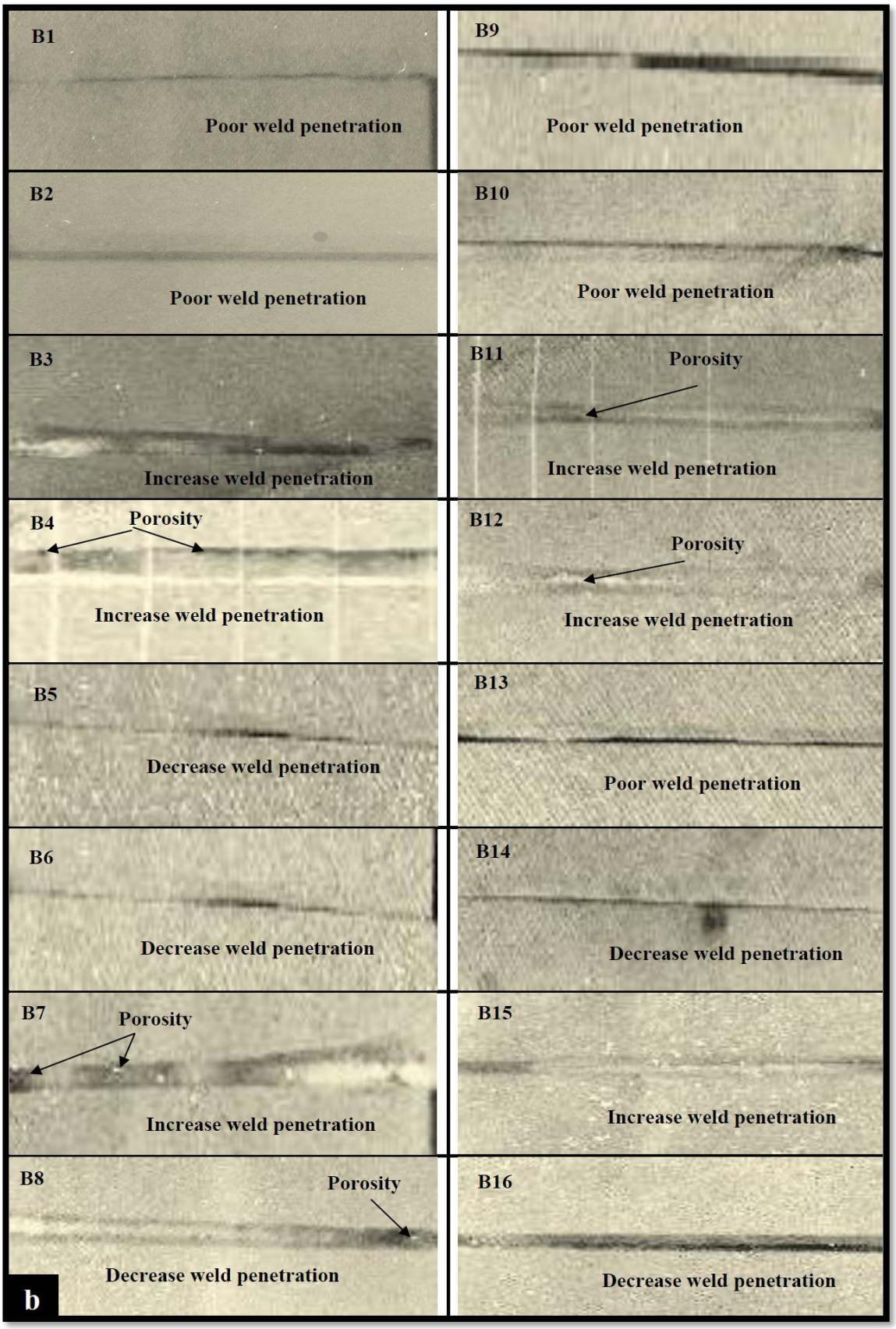

Figure (4.1): X-Ray radiographic inspection for (a): CP-Ti and (b): Ti-6Al-4V welds joined by the fiber laser method.

Figure (4.2a) shows CP-Ti samples welded with an Nd:YAG laser. It can be seen from the figure that there is incomplete penetration in samples A17, A18 and A19 welded at peak power of 1.9, 2.12 and 2.3kW respectively and 3mm/s welding speed. The highest weld penetration was however in A20 sample with increasing peak power to 2.5kW, due to the increase in heat input. A decrease in weld penetration was also observed in samples A21 up to A32, as a result of increasing the welding speed to 4, 5, 6 mm/s, and this corresponds to [12]. Good welding penetration at A24 and A28 samples was when the speeds were 4 and 5mm/sec, and the peak power was 2.5kW.

Figure (4.2b) shows Ti-6Al-4V samples welded by using the Nd:YAG laser. The figure reveals that there is a lack of welding penetration in samples B17, B18 and B19. The welding penetration increased in B20 sample due to the increase in heat input (2.5kW peak power and 3mm/s welding speed). It was also noted that the samples B21 up to B32 have less welding penetration due to the increase in welding speed from 3 to 4, 5, 6mm/s. From Figure (4.2b), it was noted that better welding penetration was in samples B20, B24, B28 when the peak power was 2.5kW and the welding speed was 3, 4 and 5 mm/s respectively, because these parameters provide sufficient heat input to obtain good penetration. Consequently, B20 sample had the best penetration. Porosity was also observed in some welds, and it decreased with increasing laser power and decreasing welding speed as a result of lower cooling rates.

No cracks were observed in these welds, because the Ti-6Al-4V alloy is not sensitive to FZ solidification and HAZ liquation cracks due to the lack of segregation of impurities and secondary phases on the grain boundaries [85].

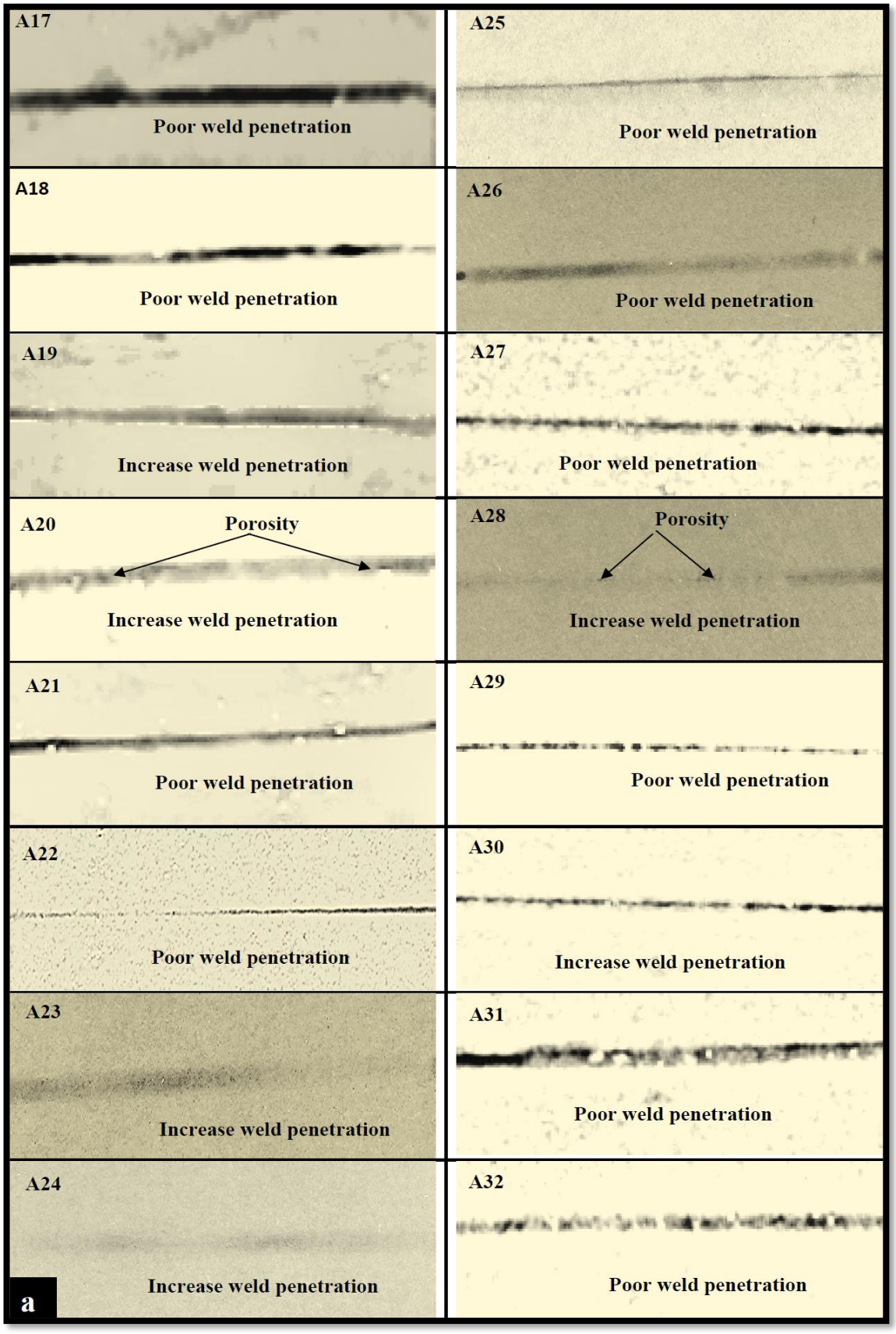
A17
Poor weld penetration
A25
Poor weld penetration
A18
Poor weld penetration
A26
Poor weld penetration
A19
Increase weld penetration
A27
Poor weld penetration
A20
Porosity
Increase weld penetration
A28
Porosity
Increase weld penetration
A21
Poor weld penetration
A29
Poor weld penetration
A22
Poor weld penetration
A30
Increase weld penetration
A23
Increase weld penetration
A31
Poor weld penetration
A24
Increase weld penetration
A32
Poor weld penetration
a

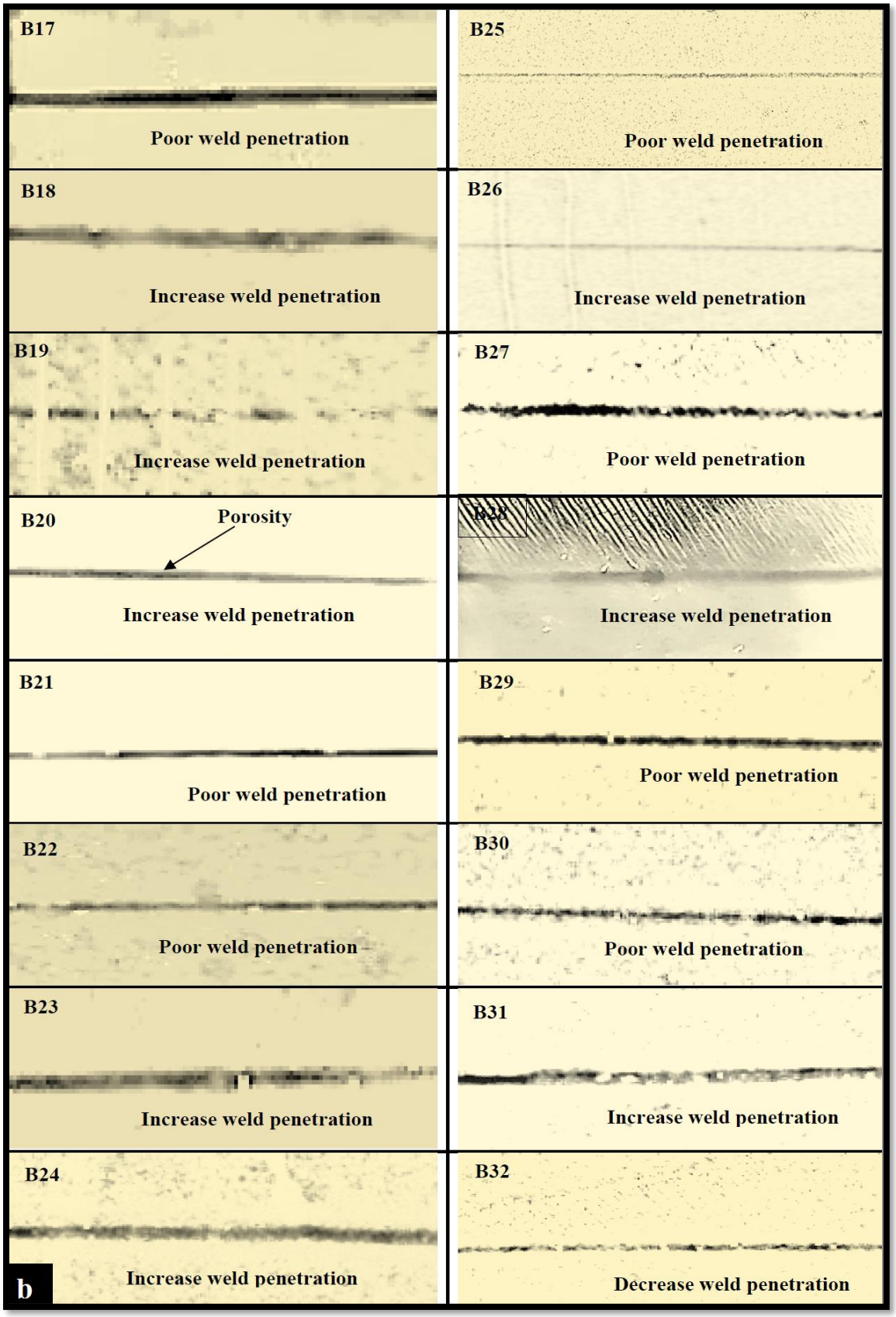

Figure (4.2): X-Ray radiographic inspection for (a): CP-Ti and (b): Ti-6Al-4V welds joined by the Nd:YAG laser method.

4.3 Measuring Visual Heat Affected Zone Width

The width of the HAZ was measured from the edge to the edge with 5mm intervals along the CP-Ti and Ti6Al4V welds as shown in Figure (4.3).

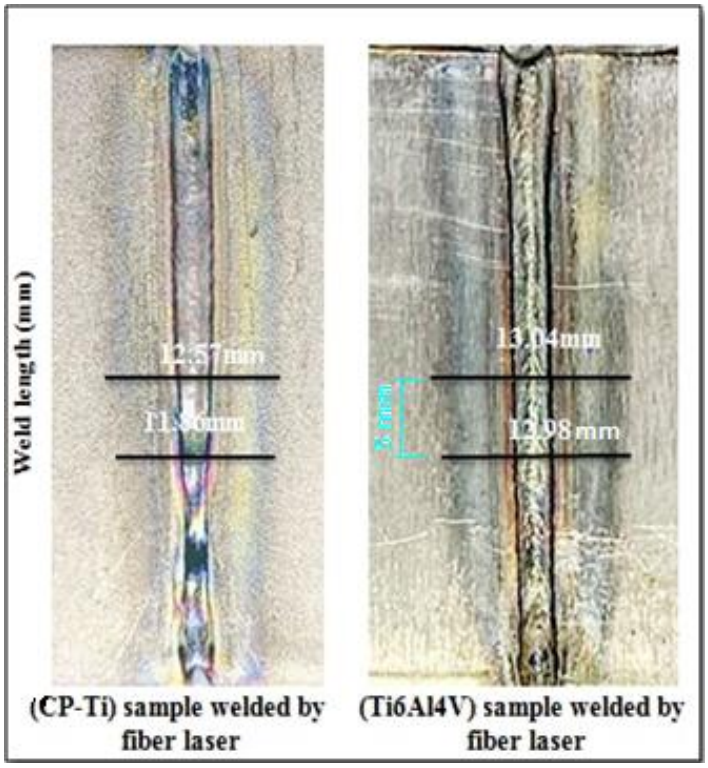

Figure (4.3): Measuring the width of the HAZ of the CP-Ti and Ti-6AL-4V welds joined by the fiber laser process.

It was clearly noted from the figure that the HAZ had less width at the ends of the samples, and increased in the middle because the ends dissipate heat faster than the middle [118].

The HAZ extent of each of the fiber laser welded samples were plotted by measuring the distance from the visible edge of the HAZ to the centerline of the weld, at 5mm intervals along the weld length of the sample. Figure (4.4) shows the measurement of the visible HAZ half-width of the samples welded using the fiber laser.

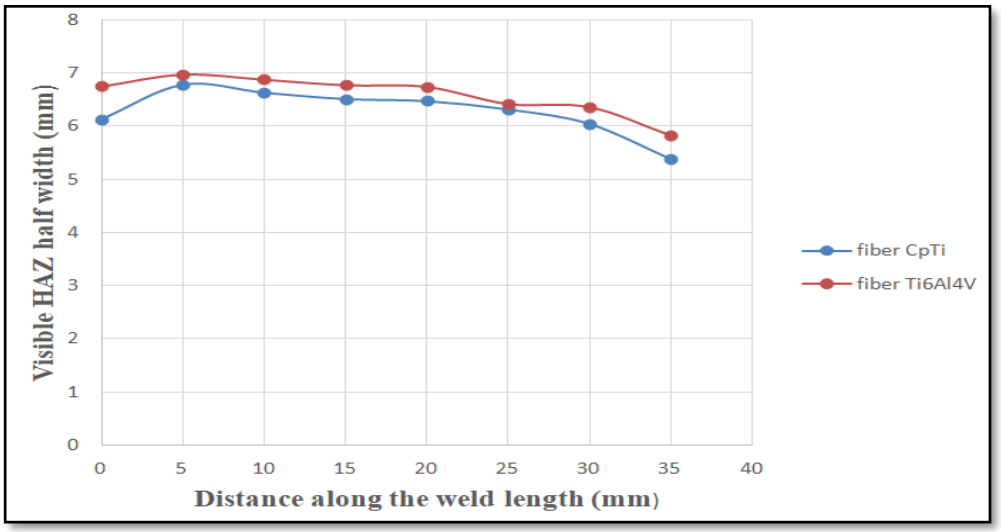

Figure (4.4): Visible HAZ half-width measured along the weld length of the (a): CP-Ti (A4) weld and (b): Ti-6Al-4V (B4) welded by the fiber laser.

Figure (4.4) demonstrates that the HAZ of B4 sample is wider than that of A4 sample, although both of them were welded under the same conditions with a laser power of 1.5kW and a welding speed of 10mm/s. Therefore, the amount of heat input was 150J/mm, which is the highest heat input for all over the samples. The Ti-6Al-4V alloy has thermal conductivity (6.7W/mm.K^{o}) lower than that of the CP-Ti (21W/mm.K^{o}). As a result, thermal energy in the molten zone is stored rather than lost for a long time [14, 96].

Figures (4.5) and (4.6) show the effect of laser power and welding speed on the average width of the HAZ for CP-Ti and Ti-6Al-4V welds. It is observed from the figures that the width of the HAZ increased by increasing the laser power from 0.6 to 1.5kW at a welding speed of 10mm/s, due to the increase in heat input, and thus the decrease in the cooling rate, as in A1, A2, A3, A4, B1, B2, B3 and B4 samples. The figures also show that increasing the welding speed to 15, 20 and 25mm/s reduces the average width of the HAZ, as a result of reducing heat input. This is in agreement with that revealed by [90,106].

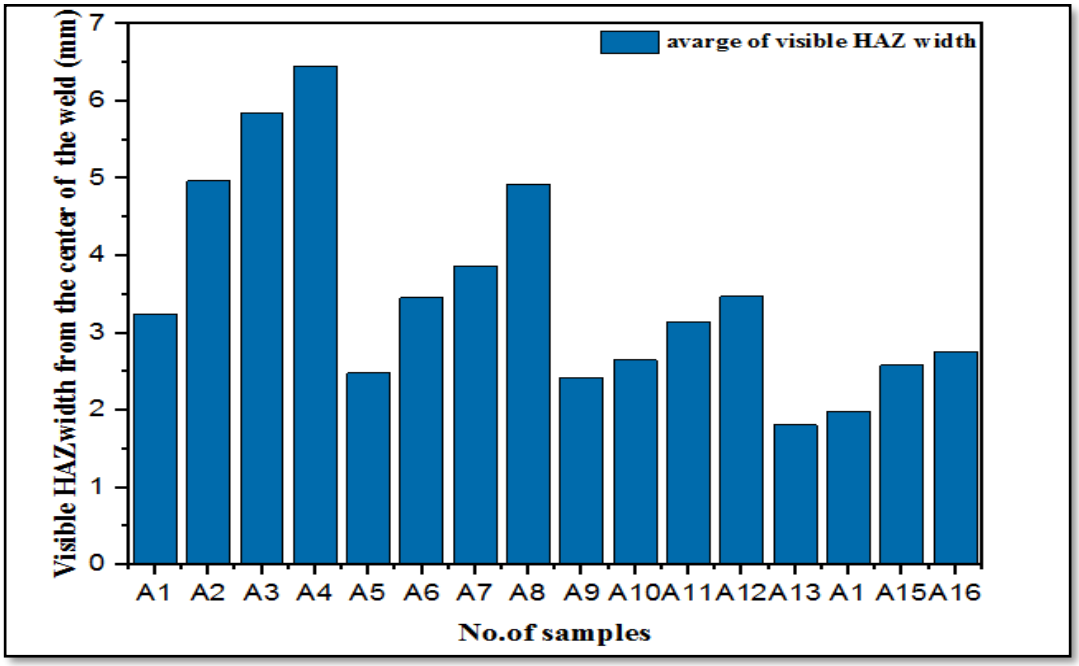

Figure (4.5): Effect of welding parameters on the HAZ width of CP-Ti samples welded by the fiber laser method.

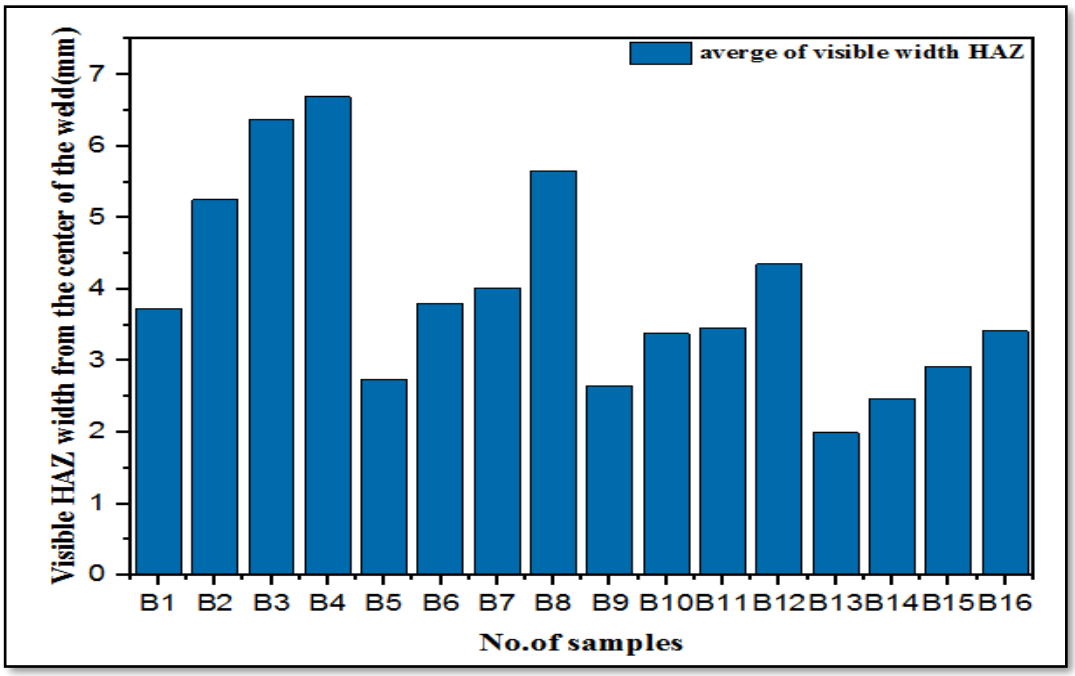

Figure (4.6): Effect of welding parameters on HAZ width of the Ti-6Al-4V samples welded by the fiber laser method.

Figure (4.7) demonstrates the effect of the amount of heat input on the HAZ width of the CP-Ti and Ti-6Al-4V samples welded by the fiber laser. It appears from the figure that the average width of the HAZ increased with

the increase in heat input, and its highest average value was 6.45mm in the A4 sample and 6.69mm in the B4 sample, where the heat input was 150J/mm, which depends largely on the laser power and welding speed. It was also noted that the width of the HAZ decreased with the increase in the welding speed. It is well known that the HAZ width is inversely proportional to the welding speed [73, 104].

Figure (4.8) exhibits a comparison of the effect of fiber laser welding parameters on the average width of the HAZ for both CP-Ti and Ti-6Al-4V samples. It can be seen from the figure that the HAZ for the Ti6Al-4V samples was wider than that of the CP-Ti samples depending on the thermal conductivity of the materials.

As for the samples welded using the Nd:YAG laser method, HAZ was indistinguishable, so it was not measured.

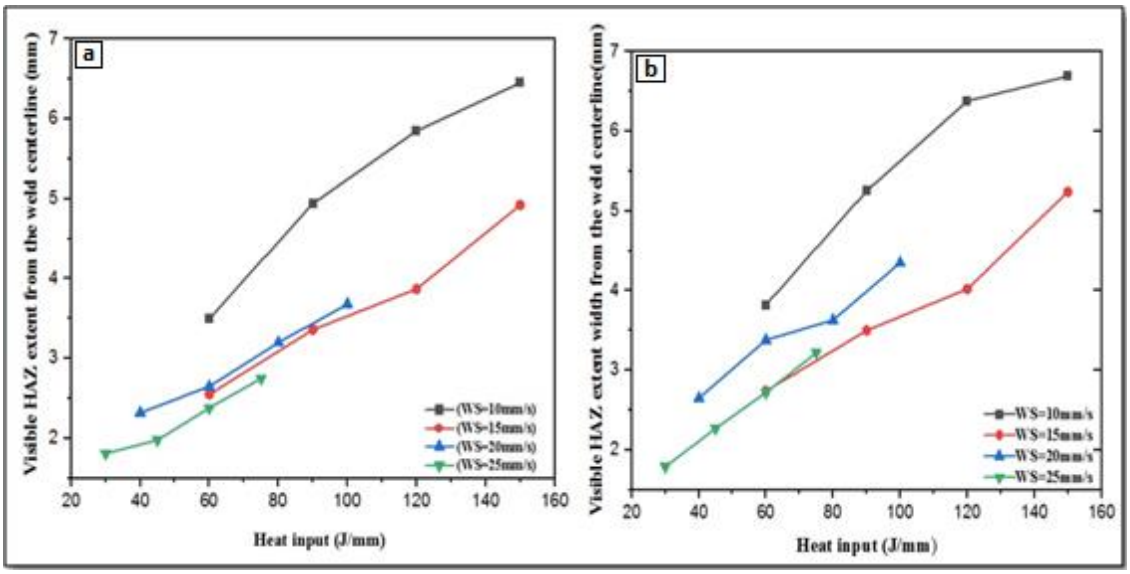

Figure (4.7): Effect of heat input on the extent of the HAZ width of the (a): CP-Ti and (b): Ti-6Al-4V samples.

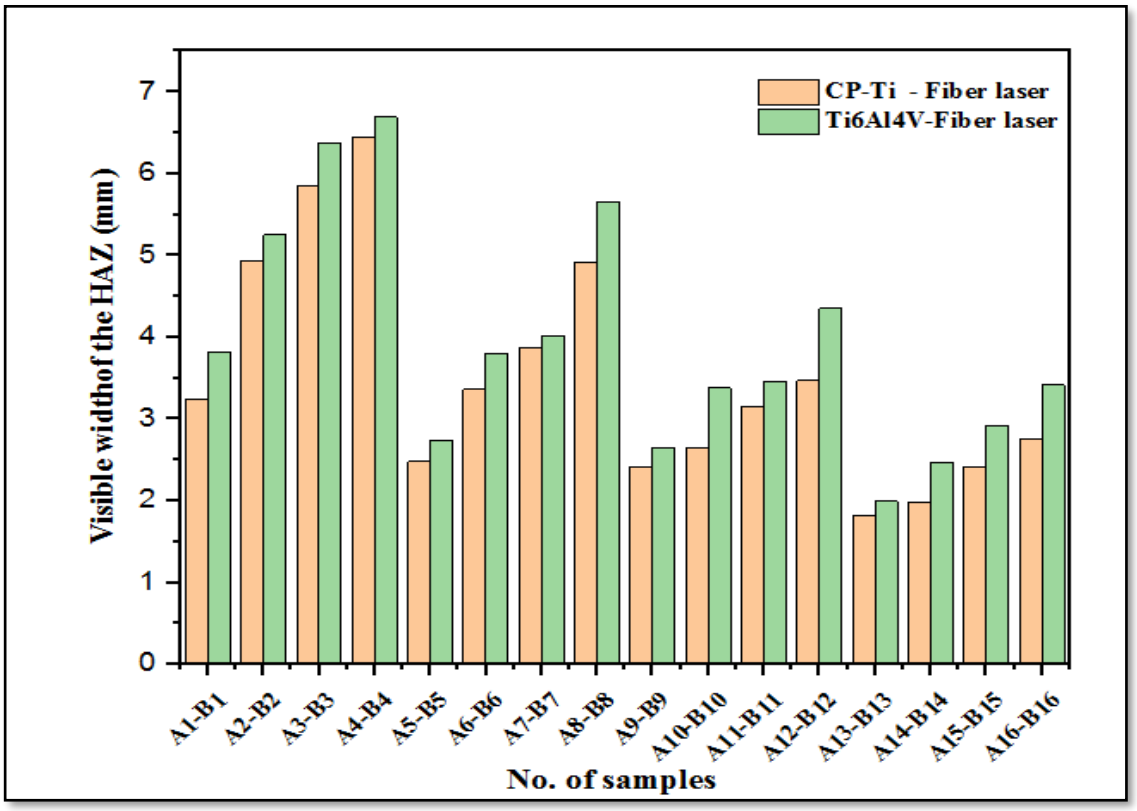

Figure (4.8): Effect of heat input on the HAZ width of the CP-Ti and Ti-6Al-4V samples welded by the fiber laser method.

4.4 Measuring the Weld Penetration Depth and Weld Zone Width

This test was carried out after cutting the samples into specimens with a cross-section of (3x20)mm, and making molds to easily handle them in the grinding, polishing and etching processes, before inspecting them with OM and SEM described in chapter three. Welding cross-sections are usually characterized by three zones (FZ, HAZ and BM) as shown in Figure (4.9).

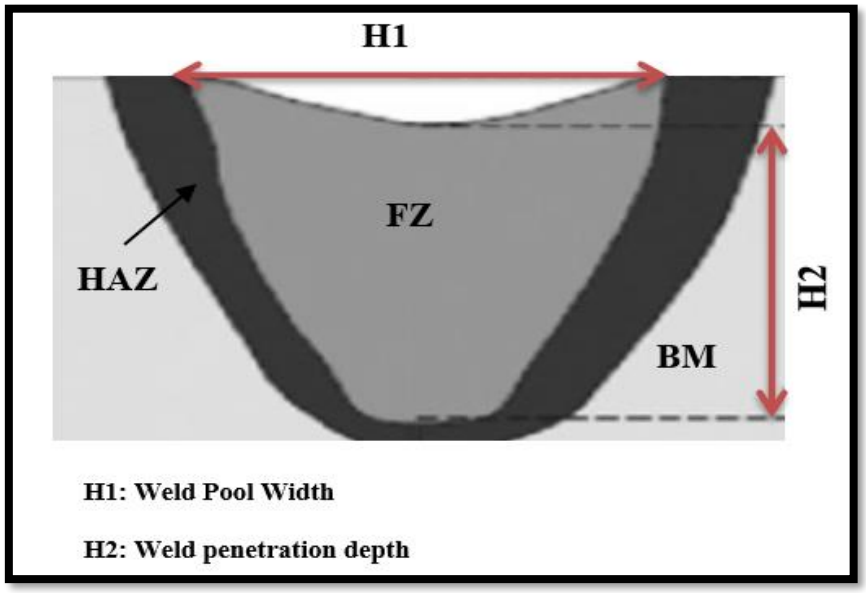

Figure (4.9): Weld cross-section characterization[12].

Figure (4.10) illustrates the effect of changing the laser power at low welding speed of 10mm/s on the weld penetration depth for the CP-Ti specimens welded by using a fiber laser method. It shows the presence of an incomplete penetration when the laser power was 0.6kW. As a result of insufficient heat input supplied to the samples, the weld pool was V shape. When the laser power increased, the weld penetration and weld pool width increased. The shape of the weld pool also changed from the V shape to an hourglass shape, as a result of the increase in heat input transferred to the material. Increasing the laser power will make the laser beam absorption high by the metal surface, which will increase the width of the upper and lower surfaces of the FZ. This was in agreement with [81,106,119]. On the other hand, a crater was observed with all samples, but its depth increased with increasing the laser power. The main reason is that the high power or high heat input encourages evaporation and expulsion of the molten metal from both sides of the weld into the weld center, which agrees with [120]. Porosity was also observed at low laser powers, as in A1 and A2 samples, because the heat input was low. So the weld pool was V-shaped, and the cooling rate was high. The gas bubbles near the surface can escape easily,

while the bubbles far from the surface (as in the V-shaped weld pool) remain confined during the weld metal solidification. The porosity decreases with the increase in laser power due to the decrease in cooling rate, and the shape of the weld pool transforms into an hourglass, as in A3 and A4 samples. So, there is an enough time for gas bubbles to escape through the upper and lower surfaces [74]. These results are consistent with those of the X-ray radiography.

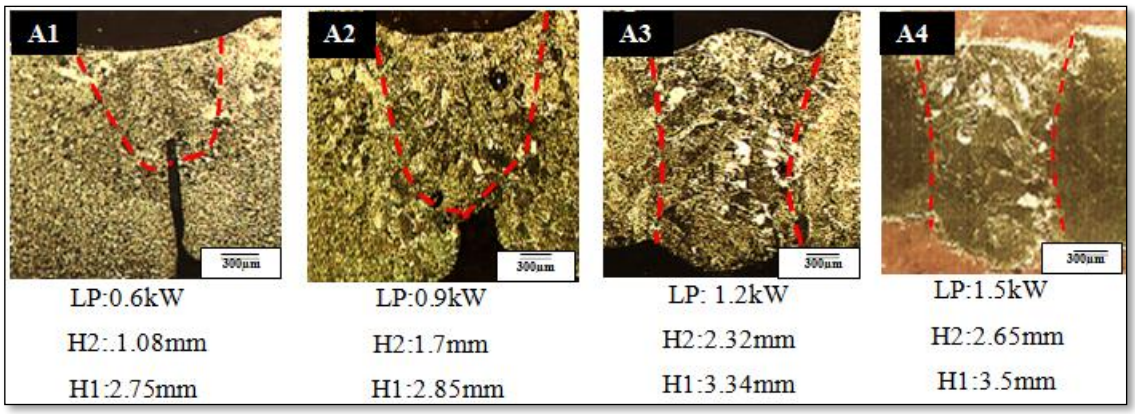

Figure (4.10): Effect of increasing laser power on the weld penetration depth, WZ width and shape of the weld pool at welding speed of 10mm/s of CP-Ti samples.

Figure (4.11) depicts the effect of welding speed on the welding penetration at 1.5kW laser power. It was observed to decrease the depth of the weld penetration with the increase in the welding speed as well as a decrease in the weld width. This was due to the decrease in heat input as a result of insufficient time for the laser beam to interact with the metal surface. The shape of the weld pool turned from the hourglass to a nail head and V shape, as in A12 and A16 samples respectively. It also caused a decrease in the width of the weld pool and the HAZ. This is in agreement with that revealed by [121]. It was also found that the crater depth decreased with increasing the welding speed.

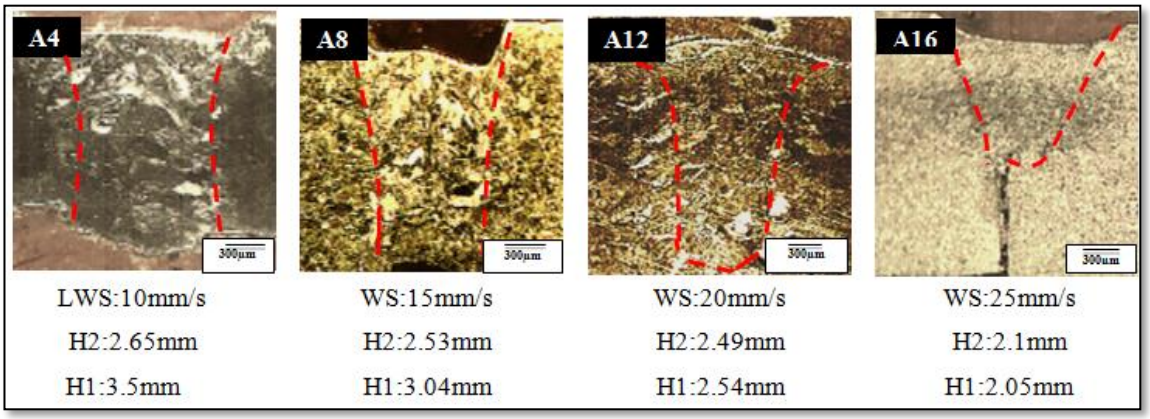

Figure (4.11): Effect of increasing the welding speed on the penetration depth and WZ width at laser power of 1.5kW of CP-Ti samples.

On the other hand, Figure (4.12) indicates the effect of laser power on the weld penetration depth at a welding speed of 10mm/s of Ti-6Al-4V samples welded by a fiber laser. It shows a lack of the weld penetration depth and the weld pool was V-shaped at low laser powers (0.6 and 0.9kW) due to the low heat input, as in the samples (B1and B2). It is also noted that the increase in laser power (B4 sample) led to an increase in the depth of the weld penetration (2.75mm), and the width of the weld pool (4.01mm). The weld pool shape also changed to an hourglass, as in the (B3 and B4). The porosity was less at high laser power, and the crater depth increased. These results are consistent with those found by [24]. It is also clearly noted that the HAZ was wider than that appeared in the CP-Ti samples, which is consistent with the results of the visual examination of the HAZ.

Figure (4.13) indicates the effect of increasing the welding speed on the depth of the welding penetration with a laser power of 1.5kW. It is observed that the penetration depth decreased with the increase in the welding speed due to the reduction of heat input. In addition, the top and bottom weld width decreased too. The depth of the crater decreased with increasing the welding speed, or with the low laser power, as shown in (B1, B2, B12 and B16 samples).

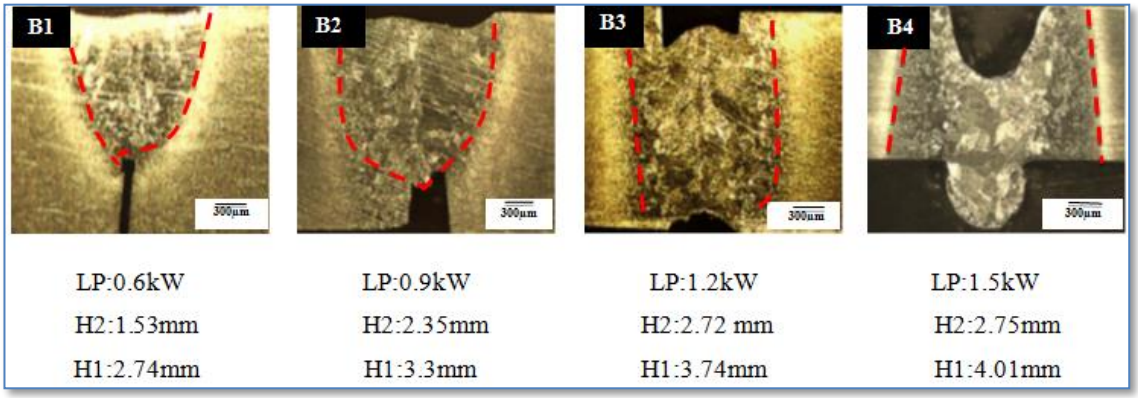

Figure (4.12): Effect of increasing the laser power on the depth of penetration and WZ width at a welding speed of 10mm/s of Ti6Al4V samples.

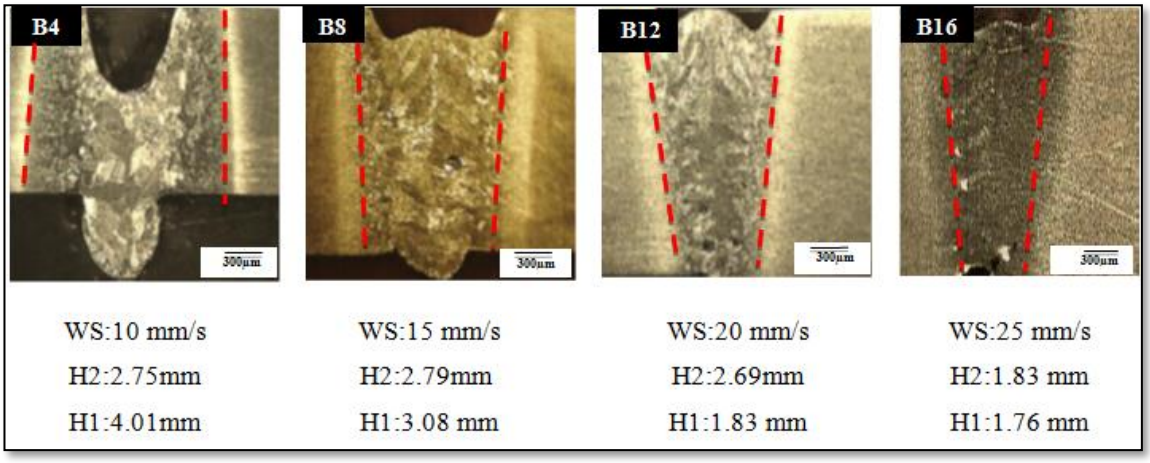

Figure (4.13): Effect of increasing the welding speed on the depth of penetration and WZ width at laser power of 1.5kW of Ti6Al4V samples.

Figure (4.14) exhibits the depth of the weld penetration for CP-Ti and Ti-6Al-4V samples using the fiber laser under the same conditions. It was found that the Ti-6Al-4V samples have more penetration than the CP-Ti samples, because the thermal conductivity of the Ti-6Al-4V alloy is lower, which makes the heat concentrates in the WZ and adjacent areas for a long time before dissipating.

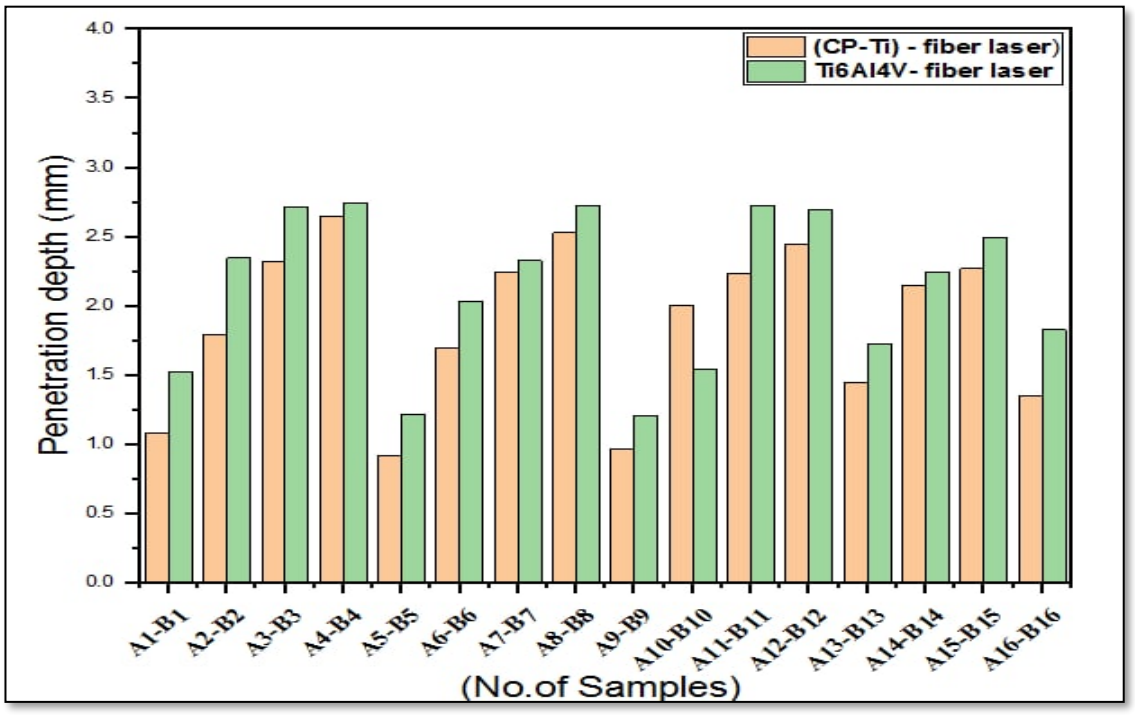

Figure (4.14): Effect of laser power and welding speed on the weld penetration depth for the CP-Ti and Ti-6Al-4V alloys welded by the fiber laser method.

When using the pulsed Nd:YAG laser welding method, welding was two-sided to obtain better penetration through the thickness of the welds, because the pulsed welding has less penetration than the CW [22]. The weld pool will therefore contain upper and lower keyholes.

Figure (4.15) illustrates the effect of changing the peak power on the weld penetration depth and weld width at a speed of 3mm/sec. It is observed that at a low peak power value, the depth of the weld penetration was low. The weld width was also narrow. The porosity was observed at lower peak energy due to the high cooling rates, because there was insufficient time for gases to escape, and decreased when the peak power was increased, as shown in samples (A17 and A18). It was also found that the depth of the weld penetration increased by increasing the peak power to 2.5kW at a speed of 3mm/s; the highest value was 2.75mm in A20 sample. Welding speed has an inverse relationship with the weld penetration depth due to the decrease in heat input, as shown in Figure (4.16).

When the welding speed was increased to 4mm/s, a decrease in the weld penetration depth and FZ width was observed, and the same results were obtained when the welding speed was increased to 5mm/s and 6mm/s, as shown in Figure (4.17). This is in agreement with the results revealed by [23].

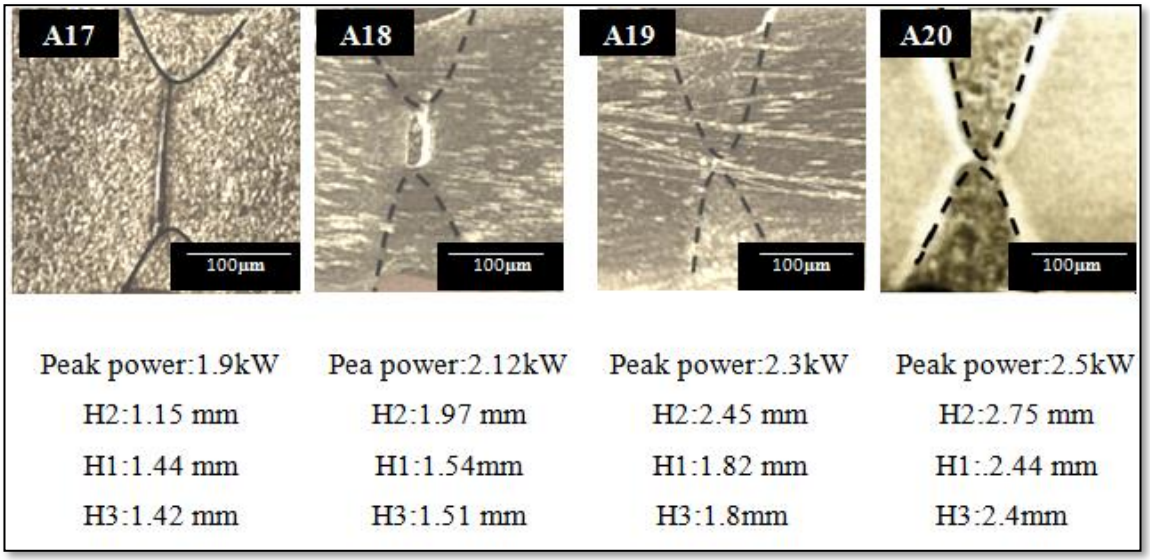

***H3: Weld pool bottom width.**

Figure (4.15): Effect of increasing peak power on the weld penetration depth and WZ width at welding speed of 3mm/s of the CP-Ti samples welded by the Nd:YAG laser.

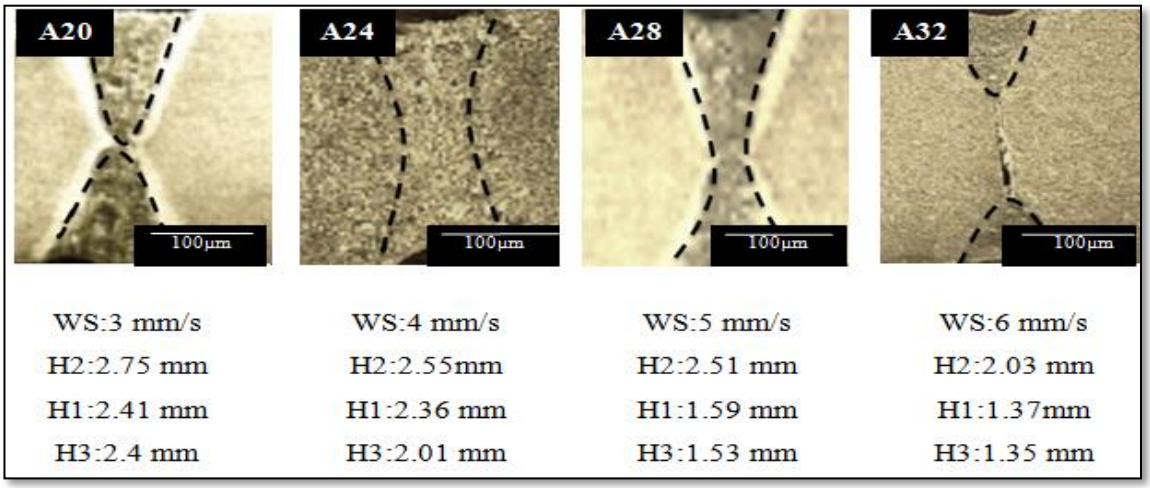

Figure (4.16): Effect of increasing the welding speed on the weld penetration depth and WZ width at peak power of 2.5kW of the CP-Ti samples welded using the Nd:YAG laser welding method.

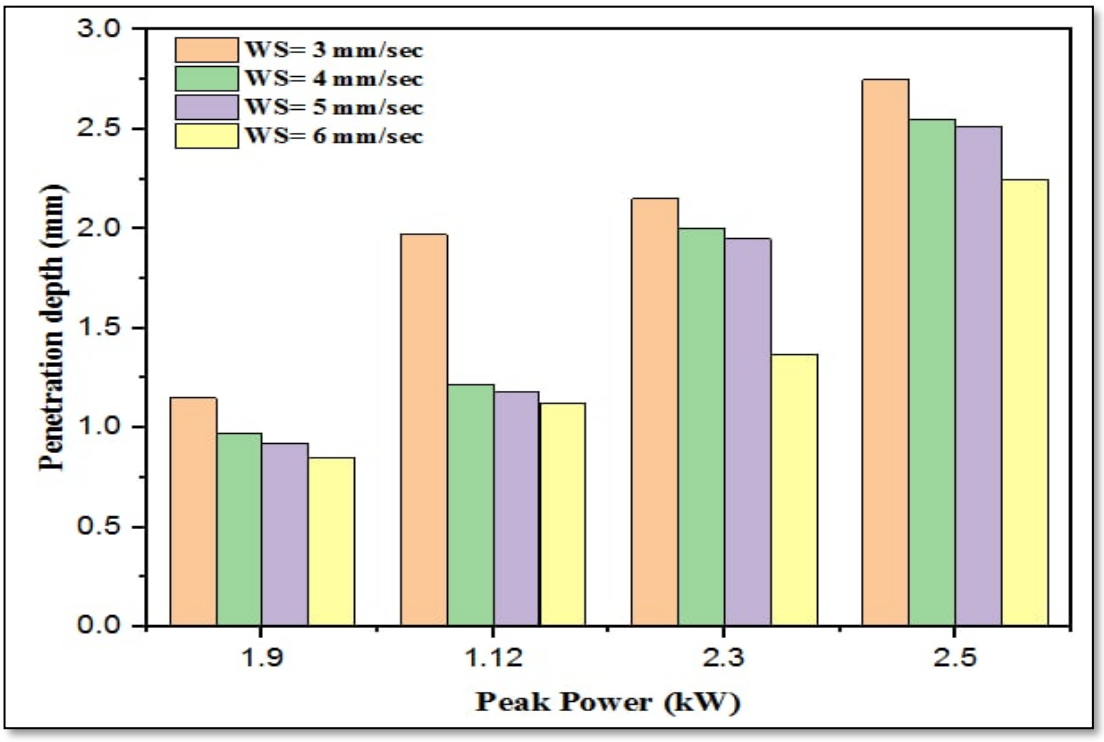

Figure (4.17): Effect of peak power and welding speed on the weld penetration depth of the CP-Ti samples welded by the Nd:YAG laser welding method.

For the Ti-6Al-4V samples, Figure (4.18) depicts the effect of the peak power change on the weld penetration depth and WZ width at a welding speed of 3mm/s. As for the CP-Ti samples welded using the Nd:YAG laser, the weld penetration increased while increasing the peak power, where the highest value was 2.83mm at 2.5kW laser power (B20 sample). It was also found that the depth of the weld penetration decreased to 2.75, 2.67 and 2.25mm when the welding speed was increased to 4, 5 and 6mm/s respectively. A decrease in the width of the WZ was also observed, as shown in Figure (4.19). Figure (4.20) shows the effect of laser power and welding speed on the weld penetration depth. It is noted from the figure that the highest penetration was at the peak power of 2.5kW and the welding speed of 3mm/s, because the heat input provided by these parameters was sufficient to obtain better penetration. Figure (4.21) exhibits a comparison for the weld penetration depth between the CP-Ti and Ti-6Al-4V alloys welded by the Nd:YAG laser method.

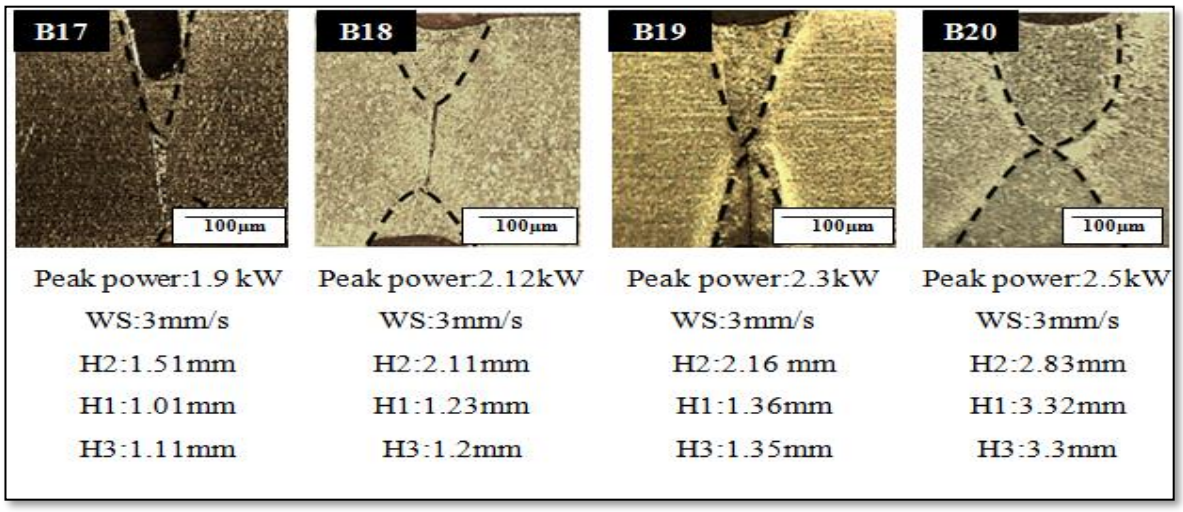

Figure (4.18): Effect of peak power on the weld penetration depth and WZ width at a welding speed of 3mm/s of the Ti6Al4V samples welded by the Nd:YAG laser welding method.

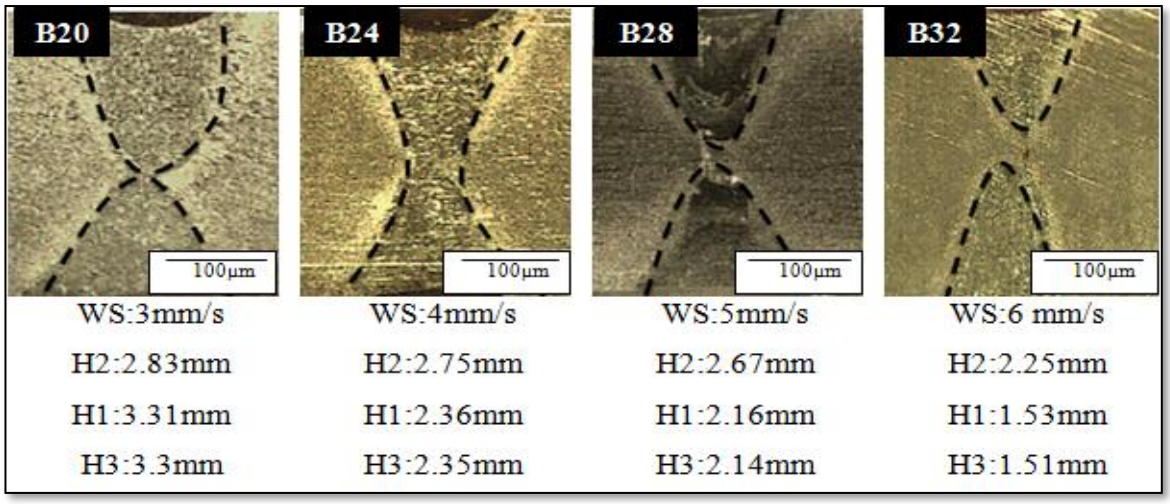

Figure (4.19): Effect of welding speed on the weld penetration depth and WZ width at peak power of 2.5kW of the Ti-6Al-4V samples welded by the Nd:YAG laser welding method.

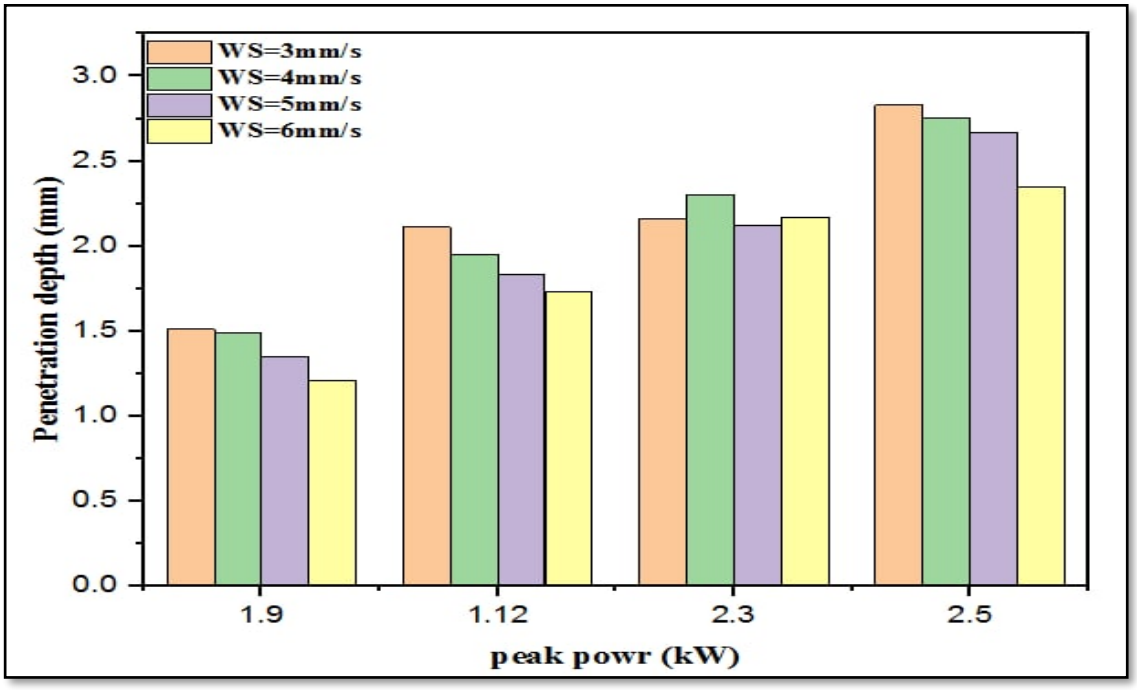

Figure (4.20): Effect of peak power and welding speed on the weld penetration depth of the Ti-6Al-4V samples welded by the Nd:YAG laser method.

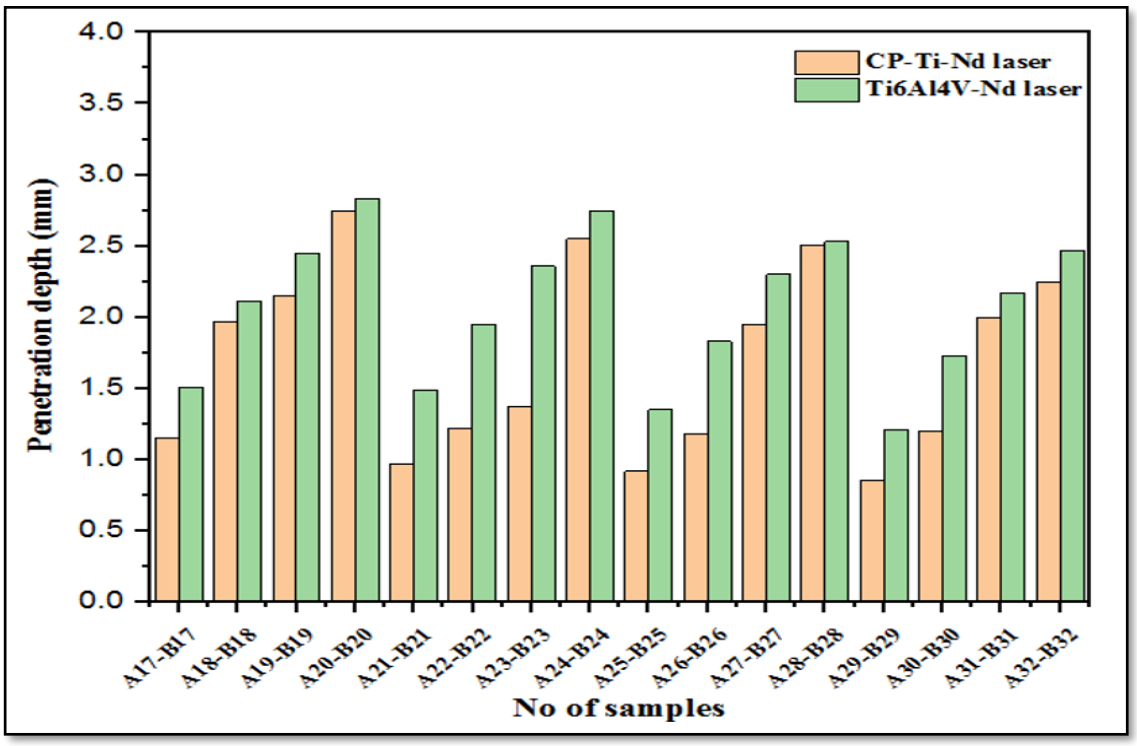

Figure (4.21): Comparison for the weld penetration depth between the CP-Ti and Ti-6Al-4V alloys welded by the Nd:YAG laser method.

4.5 Microstructural Observation

In the current study, 64 welds of the CP-Ti and Ti-6Al-4V alloys were similarly joined by using the fiber and pulsed Nd:YAG laser methods in different welding conditions, which consequently lead to various heat inputs. Higher heat inputs are typically achieved with higher laser power or/and lower welding speed, and vice versa [112]. The microstructure, and thus the mechanical properties of the welds are directly related to the heat input during welding. Therefore, the microstructure of the welds joined with the lowest heat input, highest heat input and the heat input resulting in highest tensile strength (highest weld joint efficiency) was studied.

4.5.1 Fiber Laser Welds Joined with the Lowest Heat Input

Microscopic examination for similar CP-Ti and Ti-6Al-4V welds joined by a fiber laser at a power of 0.6kW and a welding speed of 25mm/s (A13 and B13) respectively was achieved. These welding conditions resulted in the lowest heat input (24J/mm) all over the fiber laser welds. During laser welding, the laser beam is ordinarily focused on a specific area of the workpiece. Hence, the weldment is exposed to a large thermal gradient starting from the temperature of the FZ to that of the BM. Consequently, three regions can be easily distinguished, namely the BM unaffected by heat, the HAZ and the FZ, as shown in Figure (4.22). It was noted from the figure that the weld pool was a V–shaped for both welds, because the heat input was insufficient to form an hourglass shape. For the same reason, the penetration was incomplete. It was also observed that the penetration of the B13 weld was deeper than that of the A13. The reason behind this is the low thermal conductivity of the Ti-6Al-4V alloy (6.7W/m.K) comparing to that of the CP-Ti (21W/m.K). This corresponds with that proved by [14]. The HAZ was more clear and wider too.

The figure also shows that relatively fine grains were formed in the FZ center of both welds, due to lower heat input resulting in higher cooling rate, and thus insufficient time for the grains to grow. This is consistent with the [122].

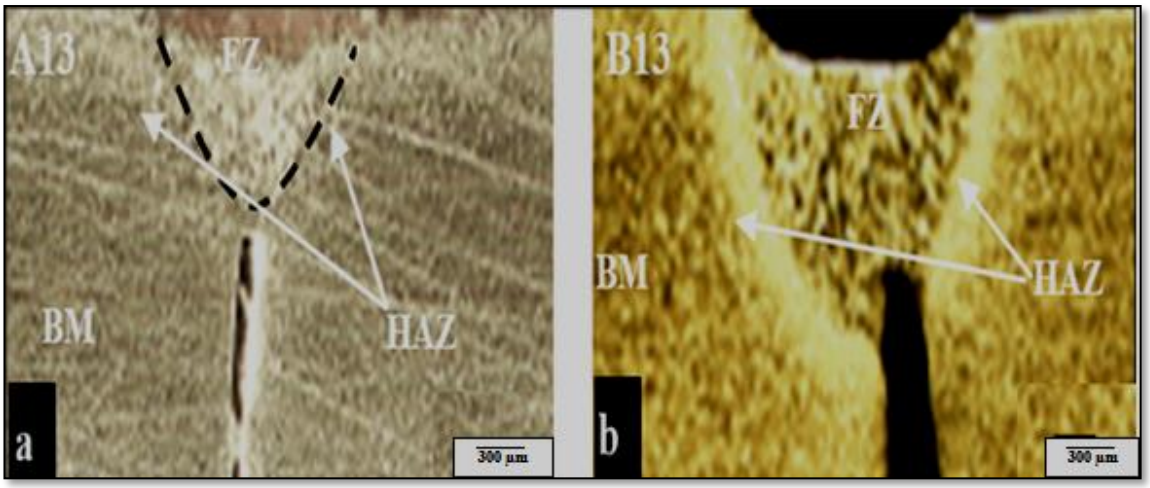

Figure (4.22): Cross-section of the (a): CP-Ti and (b): Ti-6Al-4V fiber laser welds joined with a 0.6kW and a 25mm/s welding speed.

Figure (4.23) shows that the microstructure of the CP-Ti BM consists of equiaxed grains of an alpha phase with a small amount of beta on the grain boundaries, this corresponds to [110,122,123].

Figure (4.24) illustrates the optical microstructure of the HAZ of the (A13) weld. HAZ is typically exposed to sufficient heat to undergo changes in the microstructure without melting. It is observed that the HAZ consists mostly of an acicular α phase, and this is consistent with that confirmed by [85]. The boundary between the HAZ and the BM can easily be distinguished due to their different structures, this corresponds to [110,124].

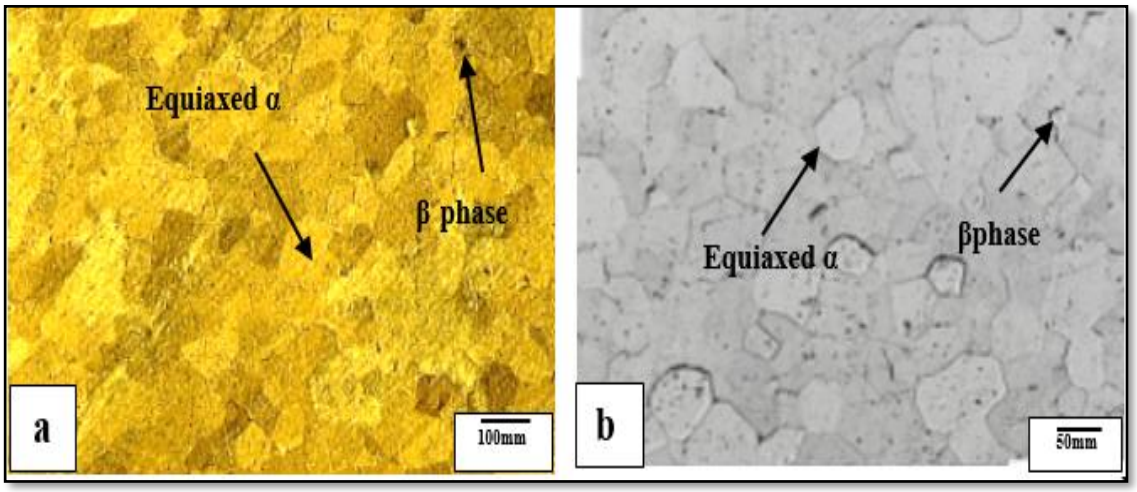

Figure (4.23): Microstructure of the (a): CP-Ti BM of the current study, (b): BM of the CP-Ti in the [122] article.

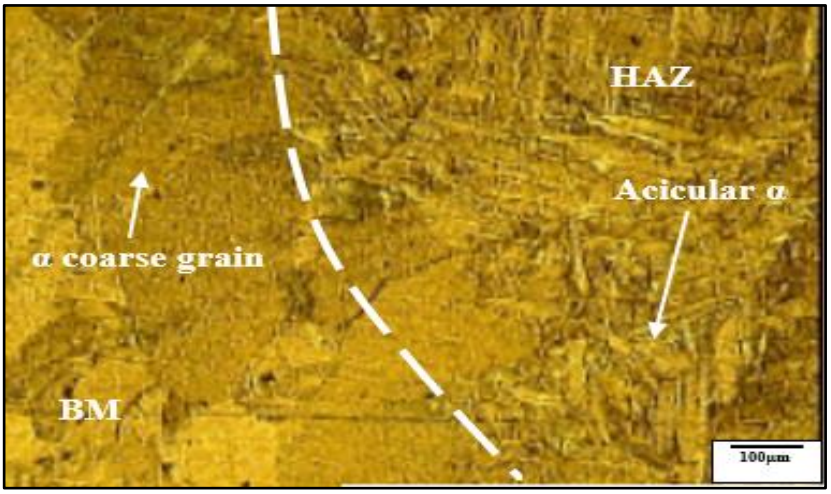

Figure (4.24): Optical microstructure of the HAZ of the A13 weld.

The FZ is ordinarily exposed to sufficient heat for melting. The resulting microstructure depends on the behavior of solidification. Figure (4.25) shows the FZ microstructure of the A13 weld which consists of an acicular α phase. It is difficult to distinguish between the HAZ and the FZ as a result of their similar structures. It is also observed that there was no martensite in the FZ. Because the alloying elements are very few in the CP-Ti, the nucleation and growth of equiaxed grains are highly challenging; only acicular structure could form; this corresponds to [125]. It is also noted that when the heat input is low, the resulting acicular α structure is thin due to the high cooling rate, this corresponds with [104].

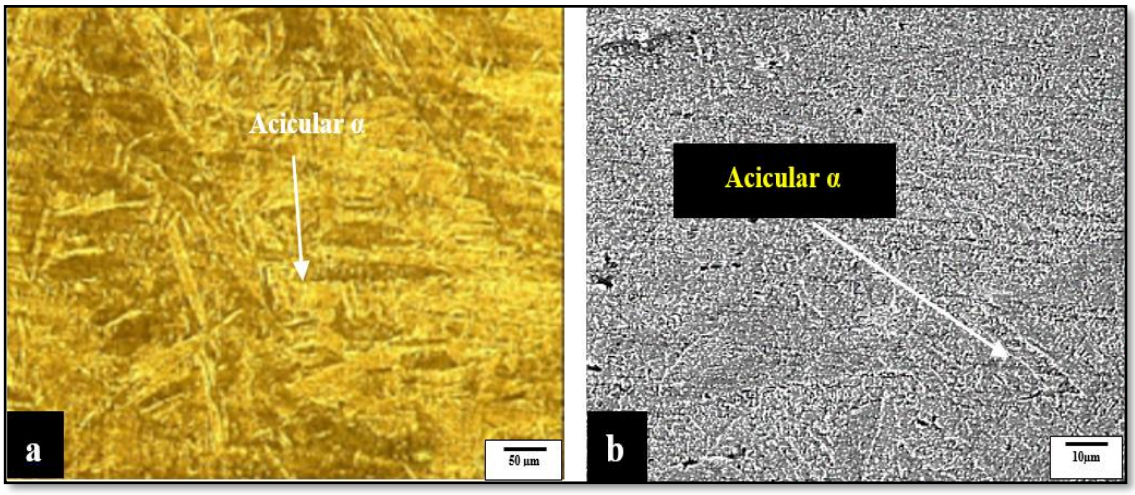

Figure (4.25): Microstructure of FZ of the A13 sample laser welded at lowest heat input using an (a): OM and (b): SEM.

As for the Ti-6Al-4V samples, the BM contains two phases, α (HCP structure) and intergranular β phase (BCC structure), as shown in Figure (4.26). Figure (4.27) exhibits the HAZ microstructures of the B13 weld. It is observed that the HAZ region near the BM consists mainly of a primary α and β phase with a small amount of acicular α` (martensite), as shown in Figure (4.27a and c). The acicular α` amount decreased while moving towards the BM due to the decrease in the cooling rate. It is also observed that the HAZ microstructure near the FZ consists mainly of a fine acicular α` and a small amount of the primary α and β phases due to the higher cooling rate, as shown in Figure (4.27b), this agrees with [106,96].

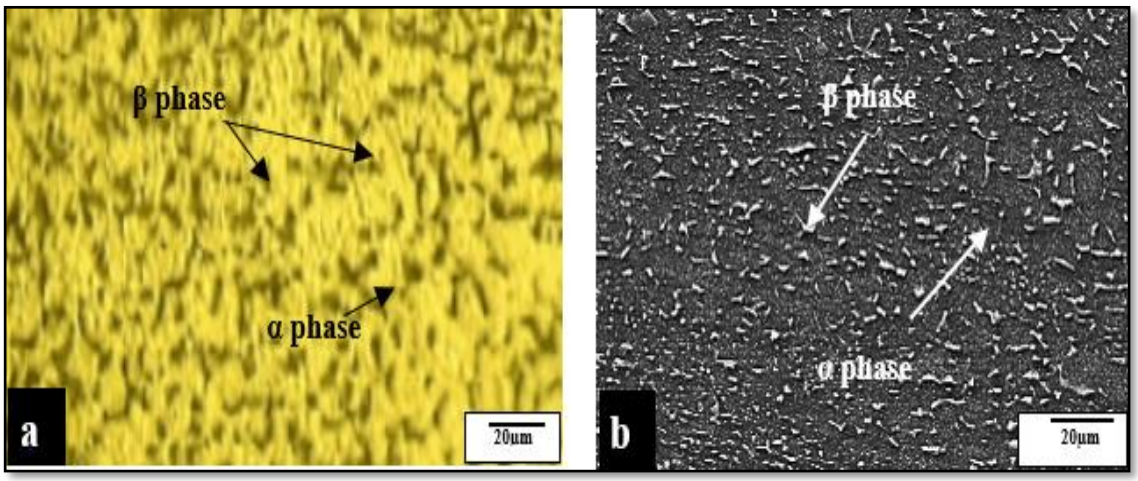

Figure (4.26): (a) Optical microstructure and (b): scanning electron microstructure of the Ti-6Al-4V BM.

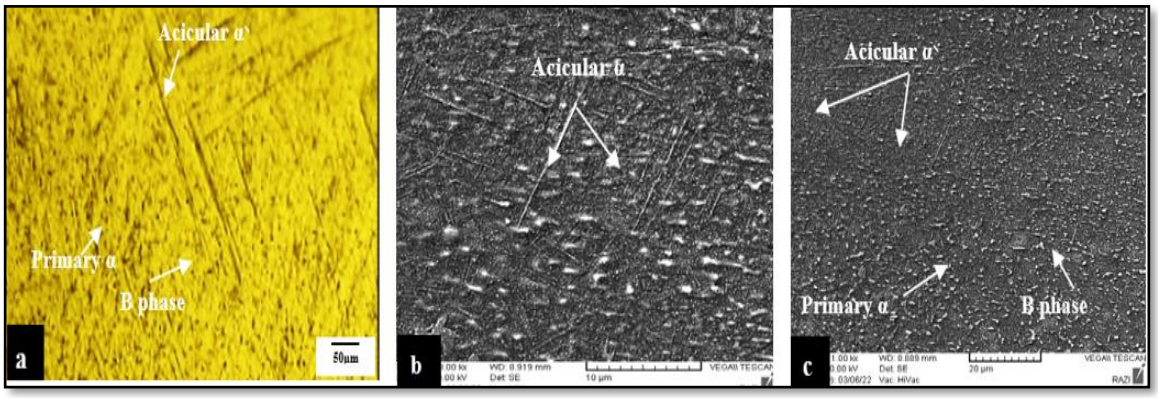

Figure (4.27): The HAZ microstructures of the B13 weld using an (a): OM, (b): SEM near the FZ and (c): SEM near the BM.

Figure (4.28) shows that the FZ microstructure of the B13 weld consisted mainly of needle martensite (acicular α`), due to the effect of alloying elements. It is also noted a β retained along the grain boundaries due to the presence of vanadium in the Ti-6Al-4V alloy, which prevents the transformation of the acicular α` at room temperature [14].

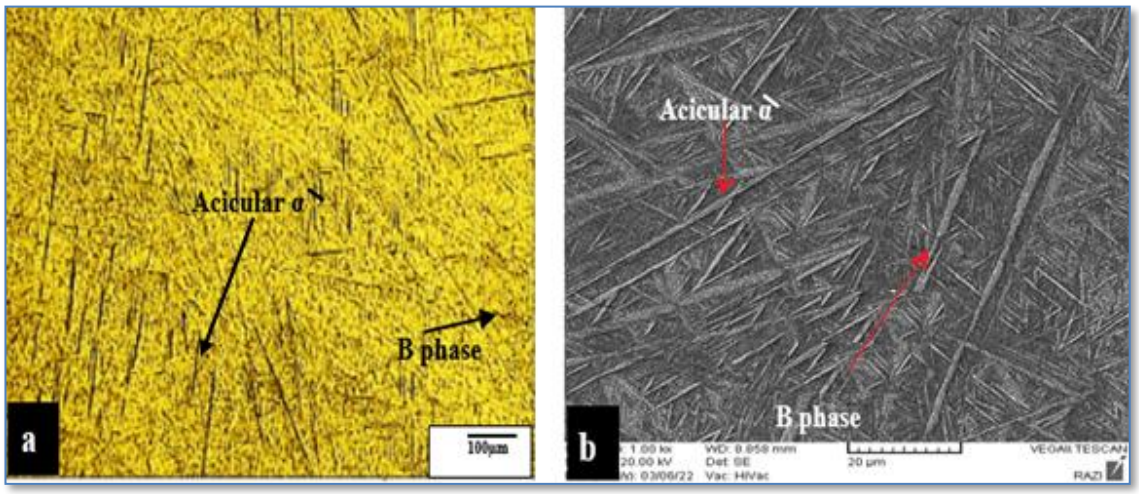

Figure (4.28): The FZ microstructure of the B13 weld using an (a) OM and (b): SEM.

4.5.2 Fiber Laser Welds Joined with the Highest Heat Input

Figure (4.29) exhibits micrographs of the A4 and B4 welds joined by using a fiber laser at a power of 1.5kW and welding speed of 10mm/s. These conditions resulted in the highest heat input (150J/mm) all over the fiber laser welds. Therefore, the shape of the weld pool changed from a V-

shape to an hourglass for both welds, this is compatible with [74]. It is observed that the grain size in the FZ and the HAZ of the A4 and B4 welds were coarser than that of the A13 and B13 welds, due to the relatively higher heat input and lower cooling rate. Therefore, grain growth occurs, this agrees with the [74,104,126]. For the same reason, the undercuts formed were deeper; this agrees with the [90]. Figure (4.30) shows that the HAZ microstructure of the A4 weld consists mainly of an acicular α and α grains near the BM, but it is coarser than those of the A13 weld due to the increase in heat input; this is compatible with the [25,11].

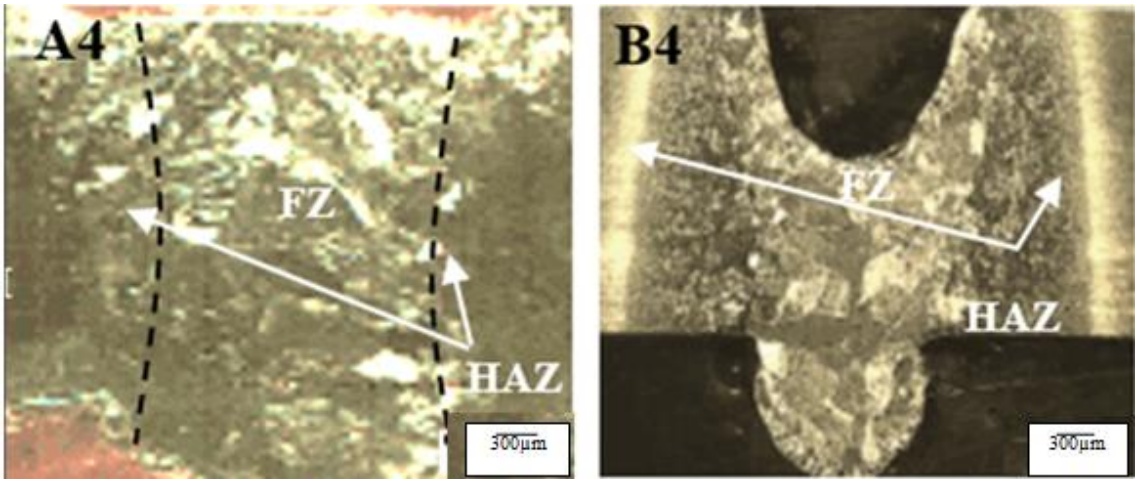

Figure (4.29): Cross–section of the A4 and B4 welds.

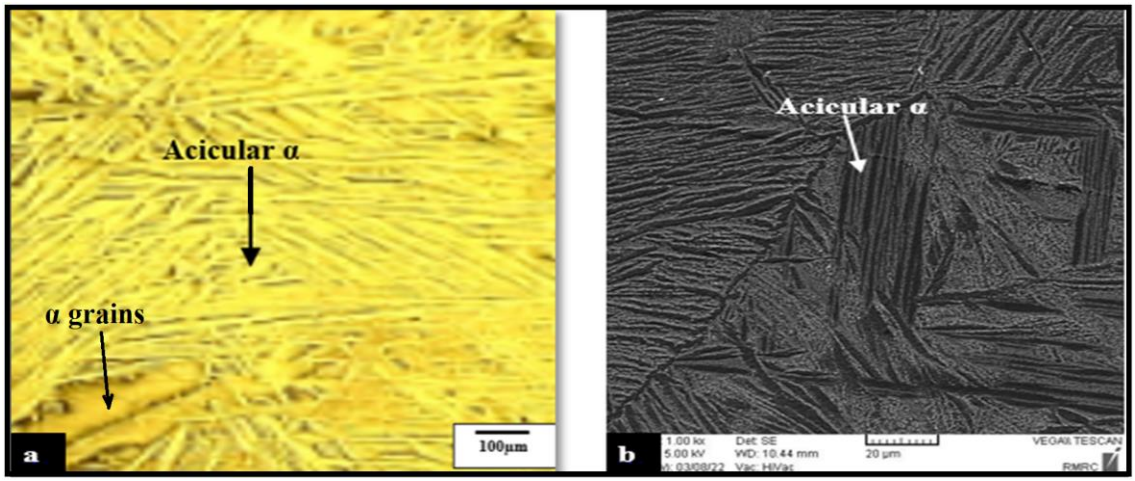

Figure (4.30): (a) Optical and (b) SEM microstructure of the HAZ of the A4 weld.

Figure (4.31) shows that the microstructure of the FZ of the A4 weld consists of an acicular α coarser than that of the A13 weld. The higher heat input led to a lower cooling rate allowing the grains to grow.

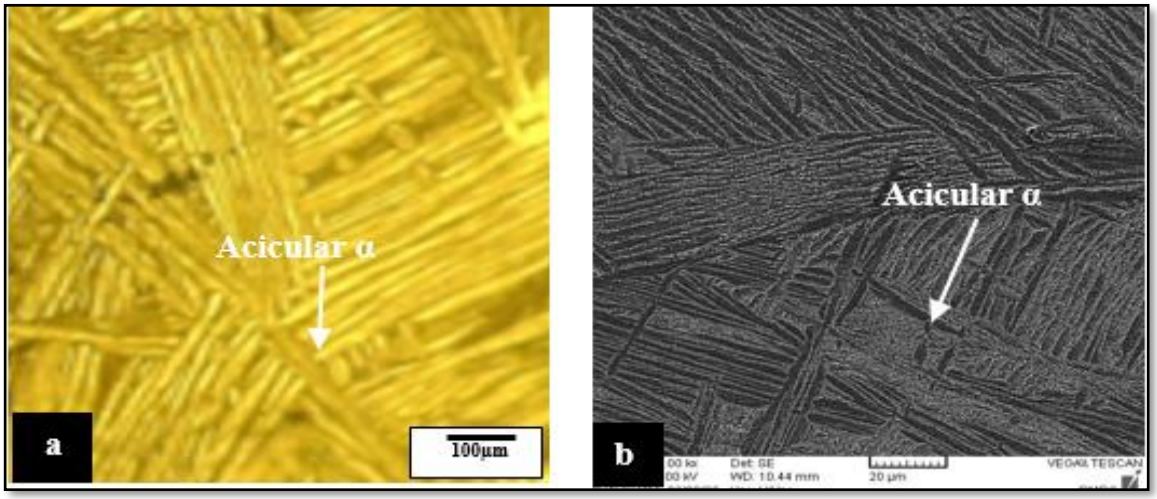

Figure (4.31): (a): Optical and (b): SEM microstructure of the FZ of the A4 weld.

Figure (4.32) shows that the HAZ microstructure of the B4 weld consists of acicular α`, primary α and β phases near the BM, while the microstructure near the FZ consists of acicular α` and a small amount from β phase, this agrees with the [113].

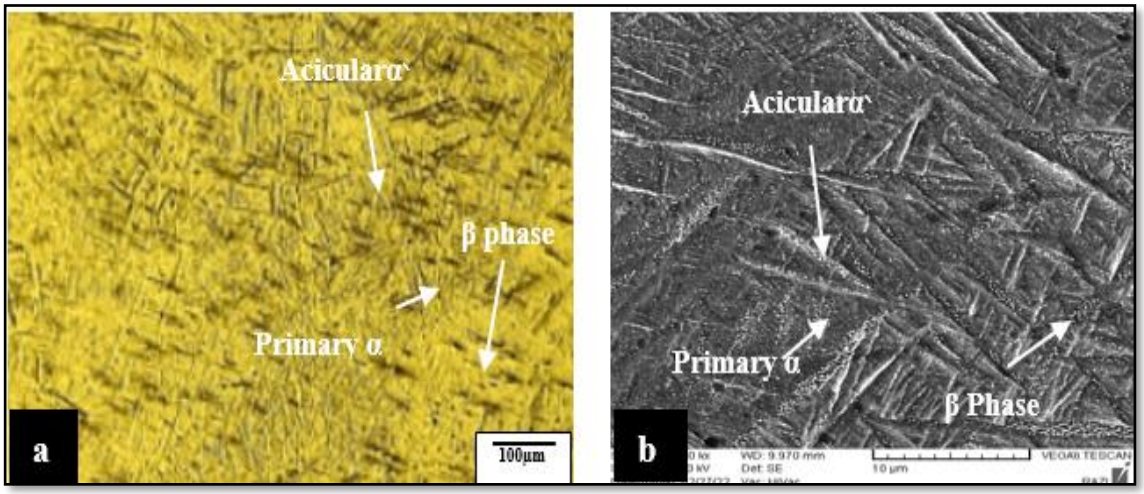

Figure (4.32): The HAZ microstructure of the B4 weld using an (a): OM and (b): SEM.

Figure (4.33) demonstrates the FZ microstructure of the B4 weld. It is observed that the FZ consists of large amount of acicular α` with small

amount of β retained on the grain boundaries. Porosity was also observed in the FZ of the B4 weld. Additionally, it was observed that the martensite did not form in the FZ of the A4 weld due to the lower level of the alloying elements in CP-Ti when compared to the FZ in the B4 weld.

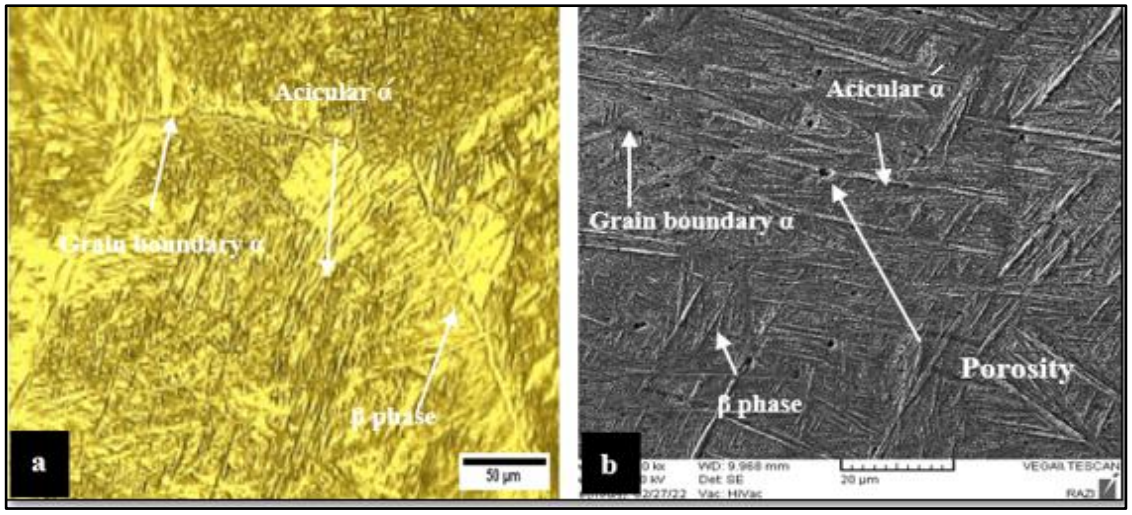

Figure (4.33): The FZ microstructure of the B4 weld using an (a): OM (b): SEM.

4.5.3 Fiber Laser Welds of the Highest Tensile Strength

Figure (4.34) shows the cross-section of the A12 and B12 welds, which have the highest tensile strengths among the CP-Ti and Ti-6Al-4V fiber laser welds. It was observed that the shape of the FZ changed to the nail head. The welding conditions of this weld were 1.5kW laser power and 20mm/s welding speed. Increasing the welding speed to this value reduced heat input to 75J/mm, so that it was not enough to form an hourglass shape. Pores were also observed due to the lack of sufficient time for gases to escape from the weld metal as a result of increasing the solidification rate, as mentioned previously. This is consistent with the results of the X-ray examination. Micrography revered in Figure (4.35a) that the HAZ structure consists of acicular α with an amount of serrated α grain as a result of the relatively high cooling rate. Figure (4.35b) shows that the FZ structure of the A12 weld contained an acicular α; the grains were finer compared to the FZ of the A4 weld due to the higher cooling rate. Figure (4.36) shows

the XRD performed on both base metal and FZ of (A12 and B12)samples for the determination of different phases. The main diffraction peaks of base metal reveals the presence of the α-Ti hcp phase. A α phases are identified for the HAZ and weld metal in welded joint. Figure(.36b)shows the attributed to both α and a α' martensite as they have similar lattice parameters(HCB).The only observed difference between the spectra of FZ and base metal was the increase in peak intensities at 38.5° and a decrease in peak intensity at 70.85° of FZ spectrum. The peak at 70.85° is attributed to α phase and the peak at 38.5° is associated to both α and a α' martensite. The conversion of α phase to a α' martensite led to a decrease in intensity of peak at 70.85°.

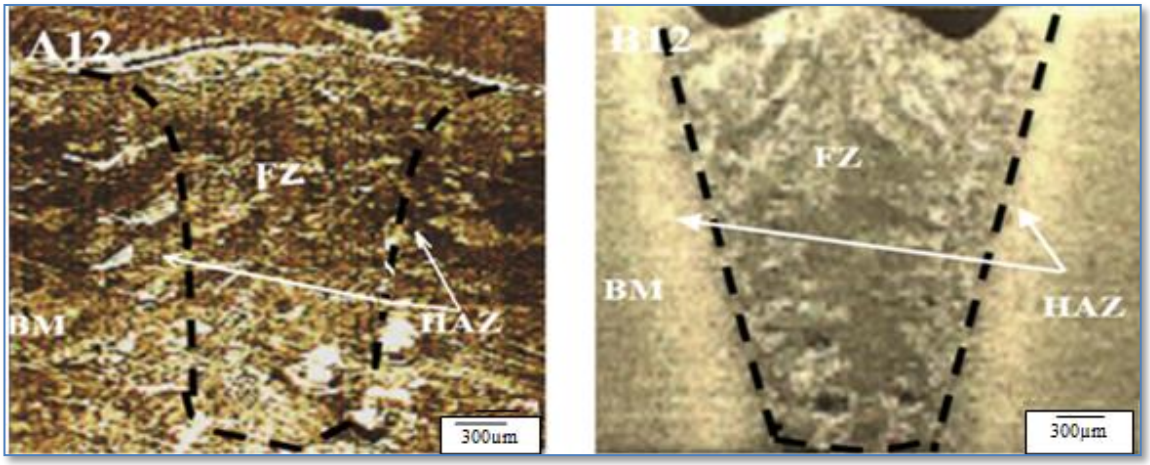

Figure (4.34): Cross-section of the A12 and B12 welds joined by the fiber laser method.

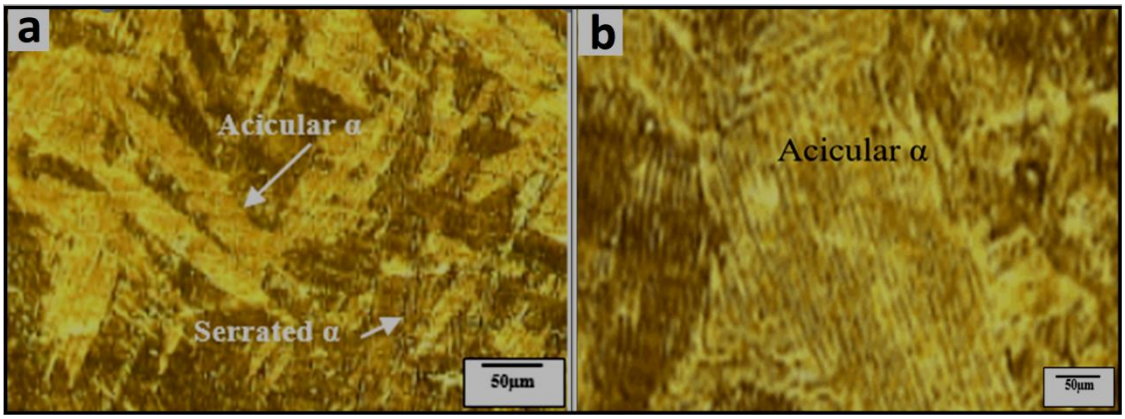

Figure (4.35): Optical microstructure of the (a): HAZ and (b): FZ of the A12 Weld joined by the fiber laser.

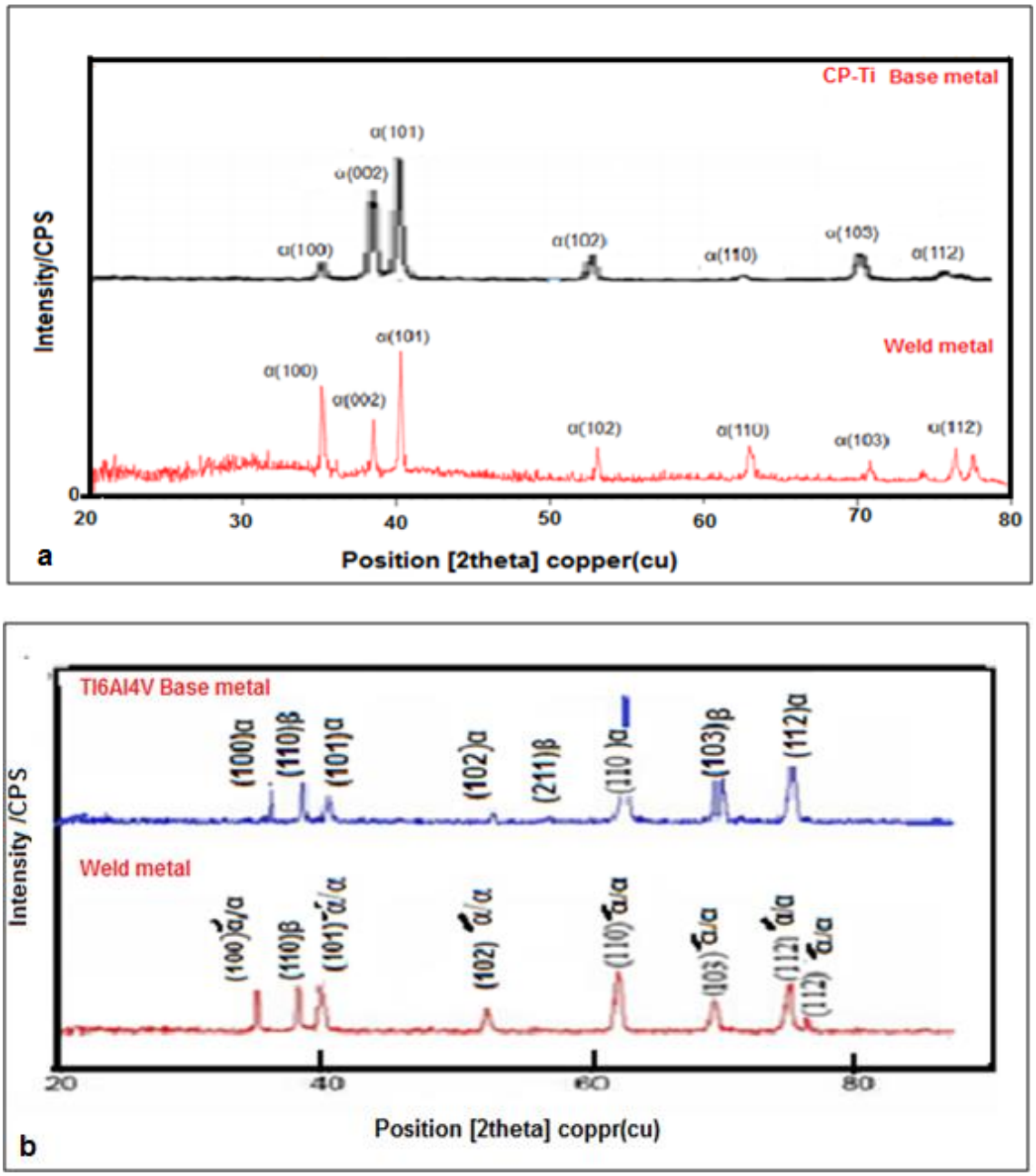

Figure (4.36): Calculated diffraction pattern in welded joints and base metal of (a):A12 (b):B12 samples.

4.5.4 Nd:YAG Laser Welds Joined with the Lowest Heat Input.

Figure (4.37) shows the microstructure of the A29 and B29 samples welded using the pulsed Nd:YAG laser from two sides at 1.9kW peak power and welding speed of 6mm/s. These welding conditions resulted in the lowest heat input (25.3J/mm) all over the welds. Therefore, the weld pools were V-shaped. It is also observed that the weld penetration depth

and weld pool width of the A29 weld were less than those of the B29 weld for the reason mentioned earlier in 4.6.1.

Figure (4.38) shows that the HAZ microstructure of the A29 weld, near the BM, consists of an acicular α, α phase and a small amount of β phase at the grain boundaries, while near the FZ consists of an acicular α. Figure (4.39) shows that the FZ microstructure of the A29 weld consists of a larger amount of acicular α than the HAZ. For the B29 weld, it was observed that the HAZ contains acicular α`, primary α and some amount β phase. The presence of martensite is due to the cooling rate being higher than the critical cooling rate. The amount of primary α and β phases increases near the BM and decreases near the FZ, as shown in Figure (4.40).

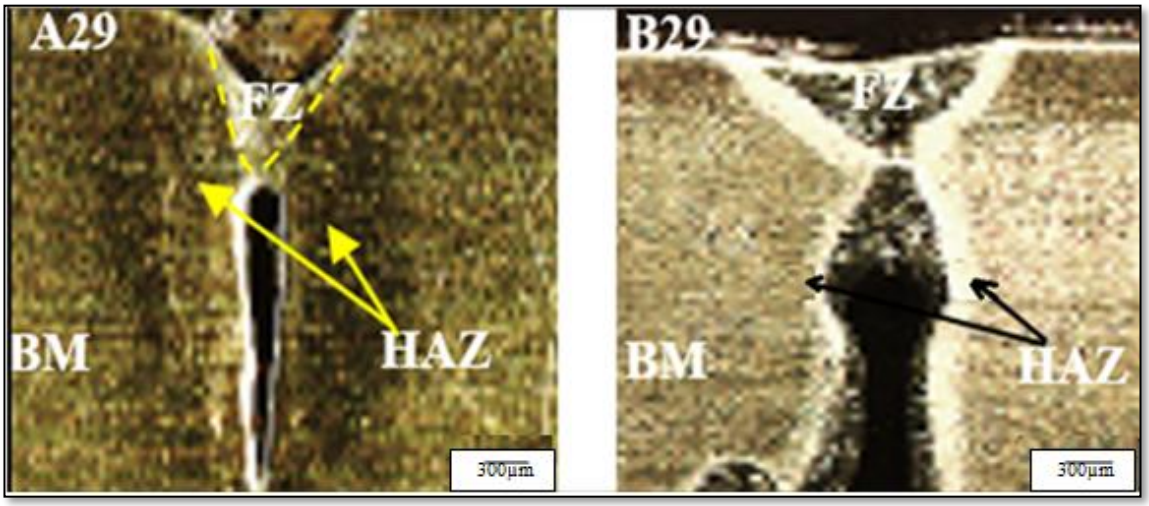

Figure (4.37): Cross–section of the A29 and B29 samples welded using the Nd:YAG laser with a 1.9kW peak power and a 6mm/s welding speed.

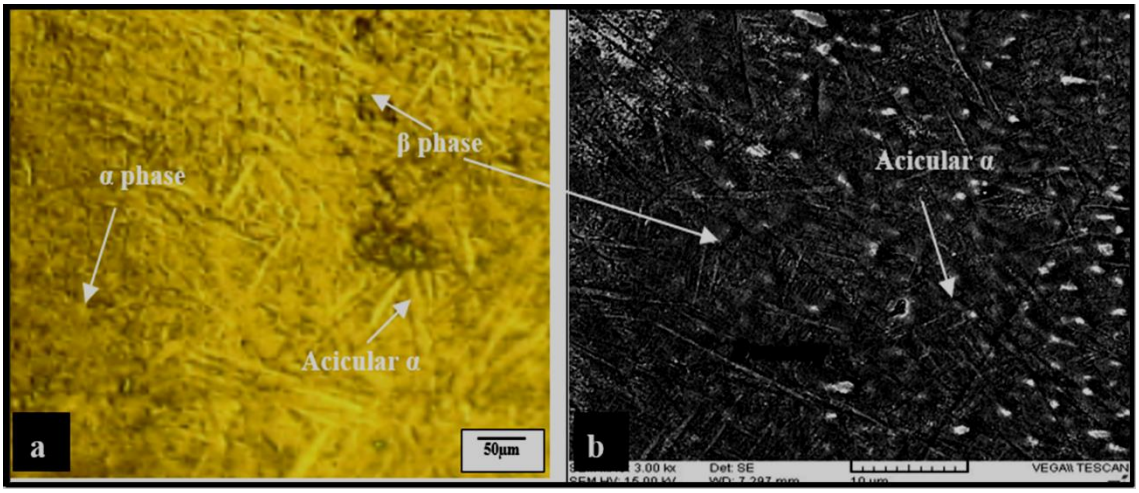

Figure (4.38): The HAZ microstructure of the A29 weld using an (a): OM and (b): SEM.

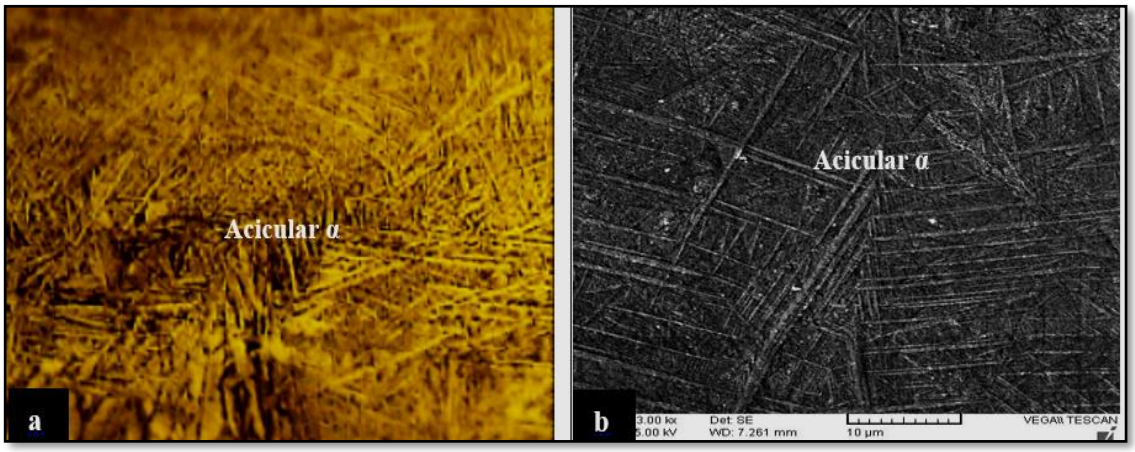

Figure (4.39): The FZ microstructure of the A29 weld using an (a): OM and (b): SEM.

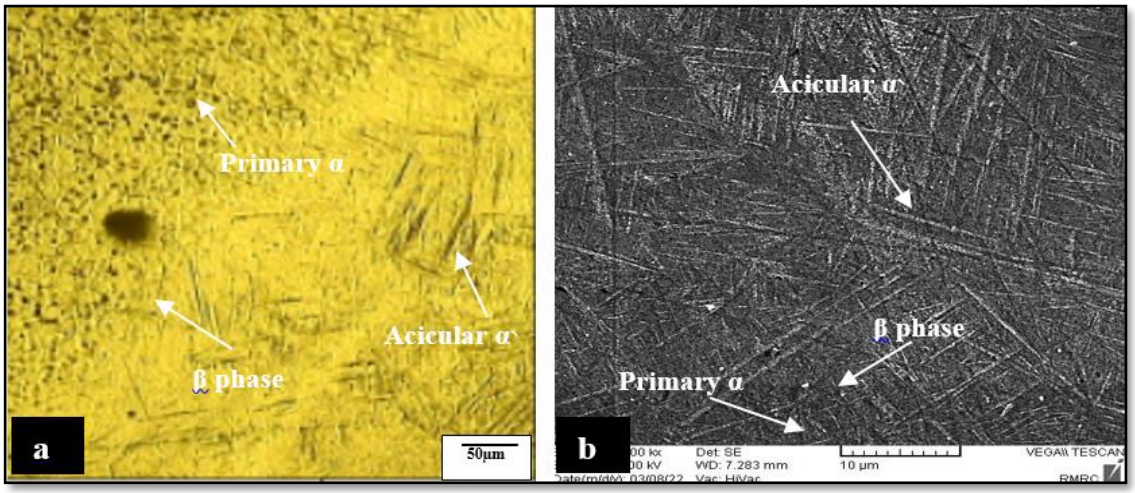

Figure (4.40): The HAZ microstructure of the B29 weld using an (a): OM and (b) SEM near the BM.

Figure (4.41) indicates that the FZ microstructure of the B29 weld consists of an acicular α` and a small amount of β phase.

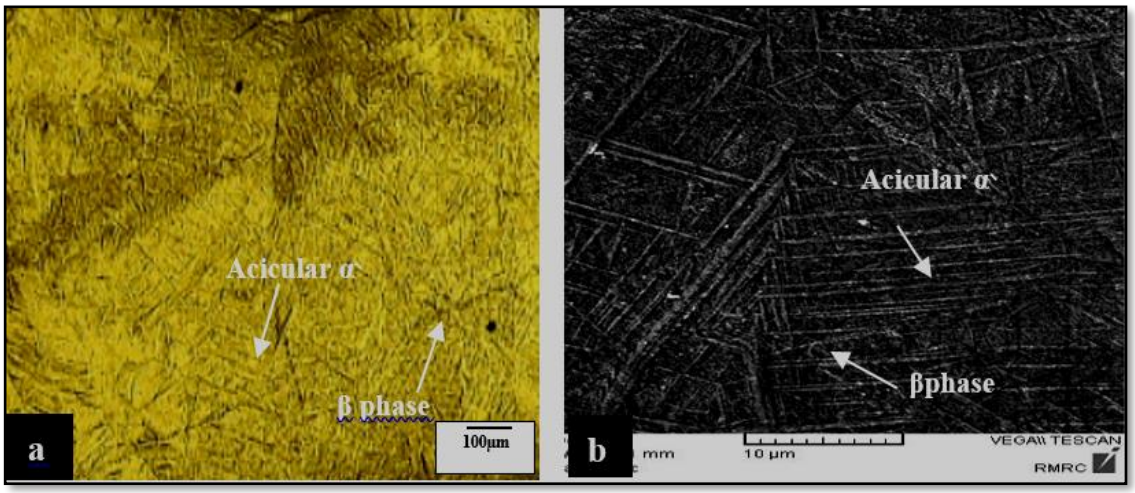

Figure (4.41): The FZ microstructure of the B29 using an (a): OM and (b) SEM near the BM.

4.5.5 Nd:YAG Laser Welds Joined with the Highest Heat Input.

Figure (4.42) shows the cross-section of A20 and B20 welds joined using the Nd:YAG laser at a peak power of 2.5kW and 3mm/s welding speed. These welding conditions resulted in the highest heat input (67J/mm) all over the Nd:YAG laser welds. Therefore, the weld pool for both welds was V-shaped. It is also noted that the weld pool of the B20 weld was wider than the A20 weld. Figure (4.43) indicates that the HAZ microstructure of the A20 weld consists of an acicular α and a small amount β phase. It is noted from the Figure (4.44) that the FZ microstructure consists of a large amount of acicular α.

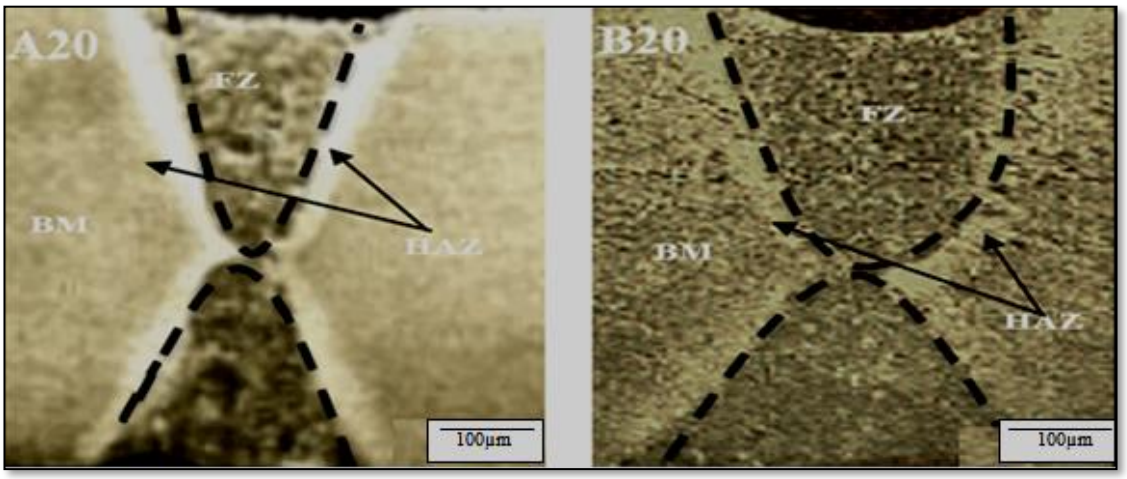

Figure (4.42): Cross-section of the A20 and B20 welds.

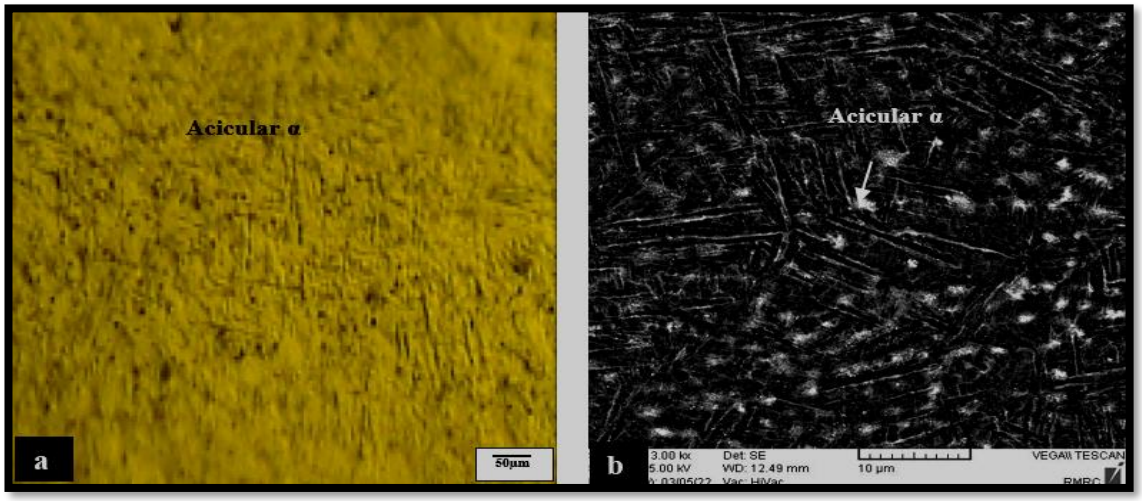

Figure (4.43): The HAZ microstructure of the A20 weld using an (a): OM and (b): SEM.

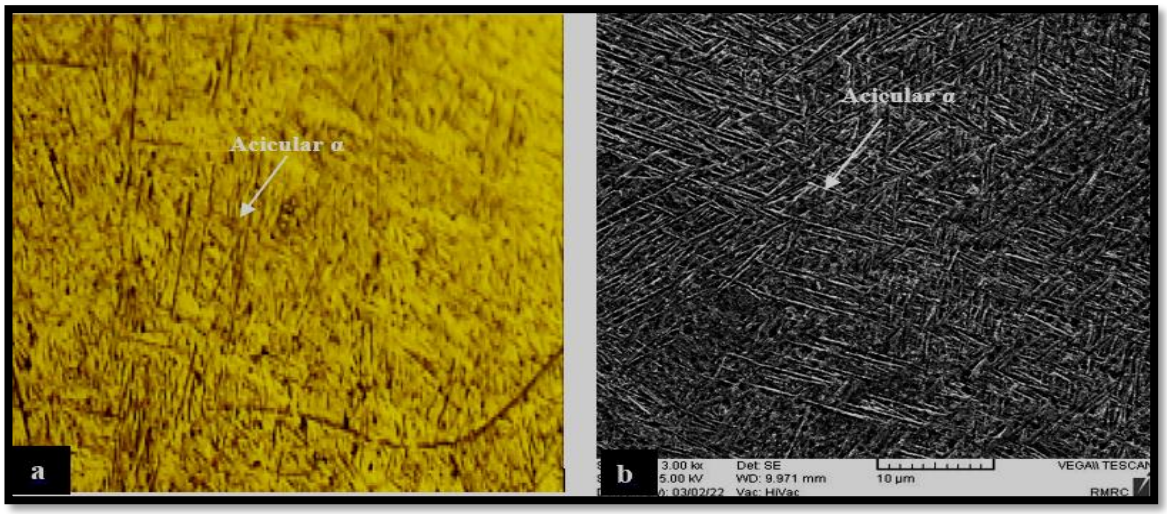

Figure (4.44): The FZ microstructure of the A20 weld using an (a): OM and (b): SEM.

Figure (4.45) shows that the HAZ microstructure of the B20 weld consists of a large amount of acicular α`, primary α, and β phases. Figure (4.46) illustrates that the FZ of the B20 weld consists of an acicular α` and a small amount of β phase.

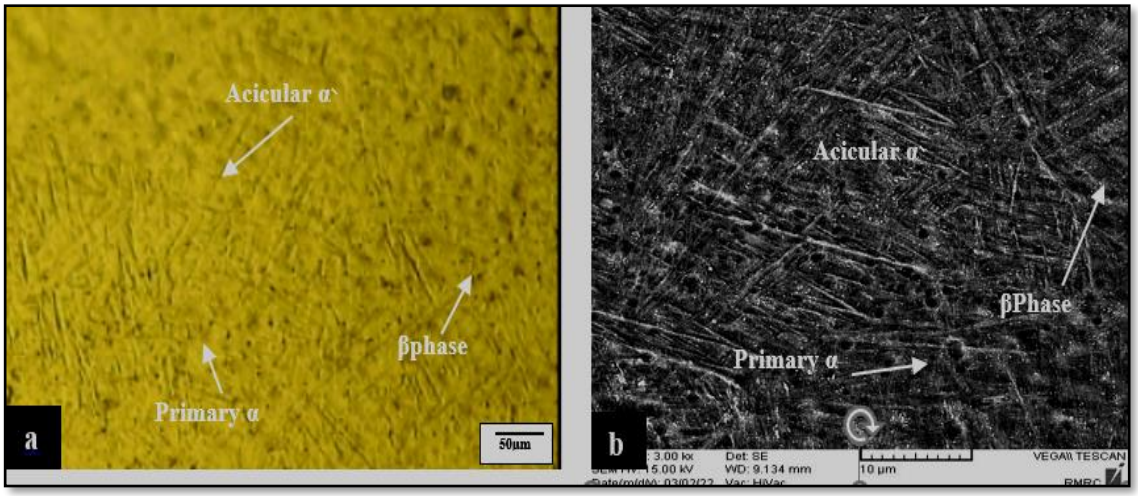

Figure (4.45): The HAZ microstructure of the B20 weld using an (a): OM and (b): SEM.

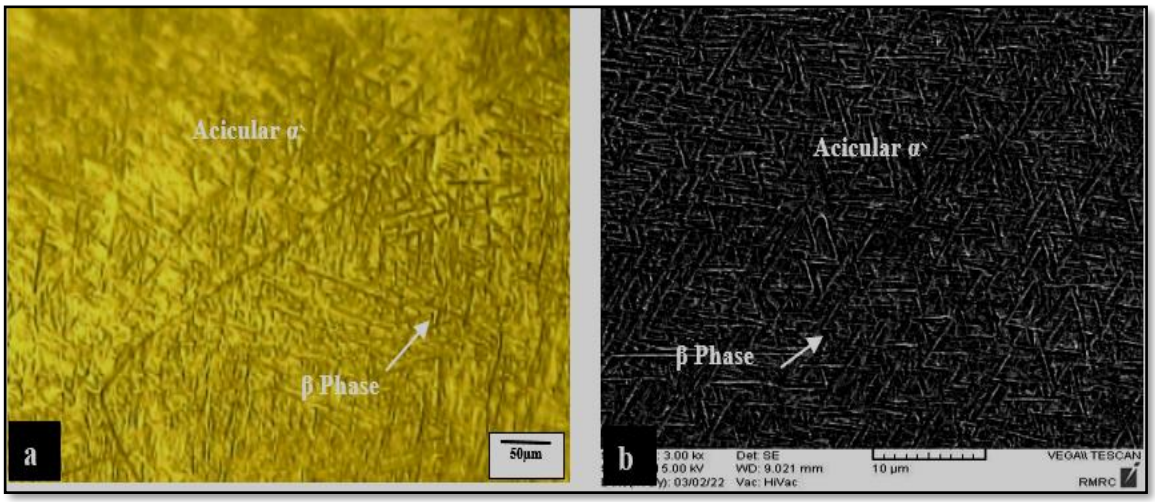

Figure (4.46): The FZ microstructure of the B20 weld using an (a): OM and (b): SEM.

4.5.6 Nd:YAG Laser Welds of the Highest Tensile Strength.

Figure (4.47) illustrates the cross-sections of the A28 and B24 welds, which have the highest tensile strengths compared to other welds. The A28 weld was laser welded at 2.5kW peak power and 5mm/s welding speed, while the B24 weld was welded at 2.5kW peak power and 4mm/s welding

speed. These welding conditions resulted in heat inputs of 40J/mm and 50J/mm respectively. These heat inputs were enough to give the weld pool an hourglass shape for both welds.

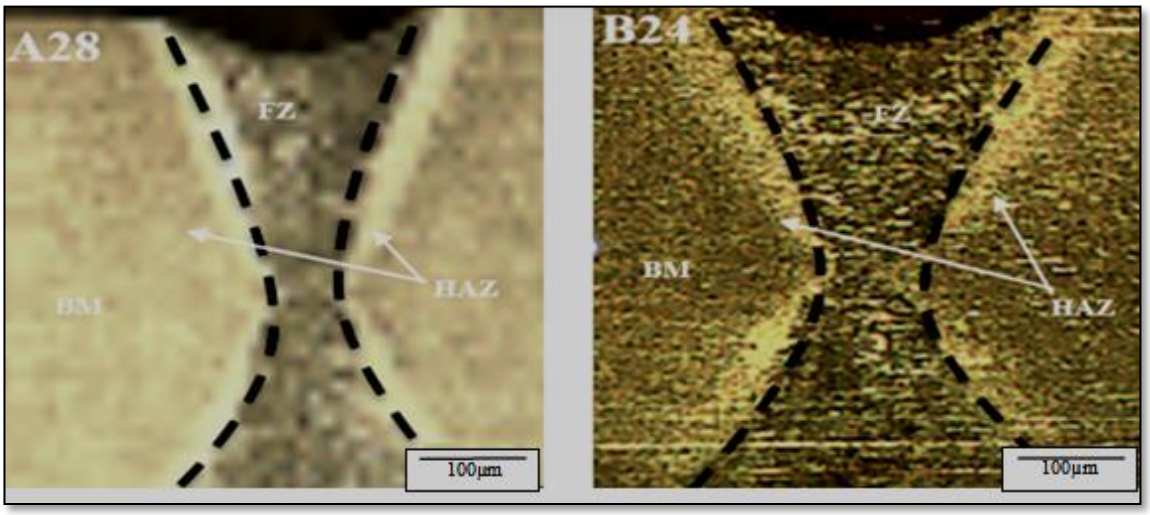

Figure (4.47): Cross-section of the A28 and B24 welds.

Figure (4.48) exhibits that the HAZ microstructure of the A28 weld consists of acicular α in addition to α grains. The FZ microstructure of this weld however consists of acicular α as shown in Figure (4.49).

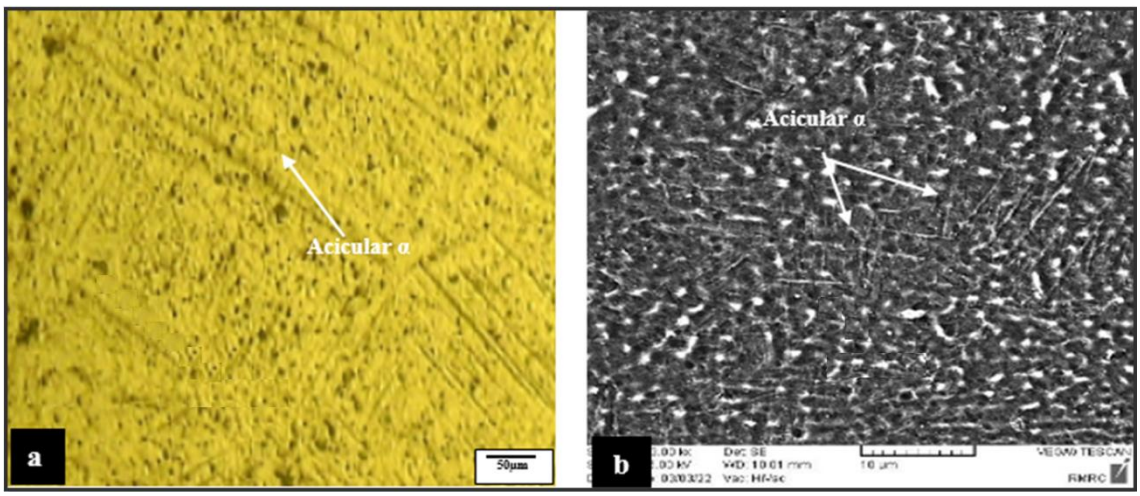

Figure (4.48): The HAZ microstructure of the A28 weld using an (a): OM and (b): SEM.

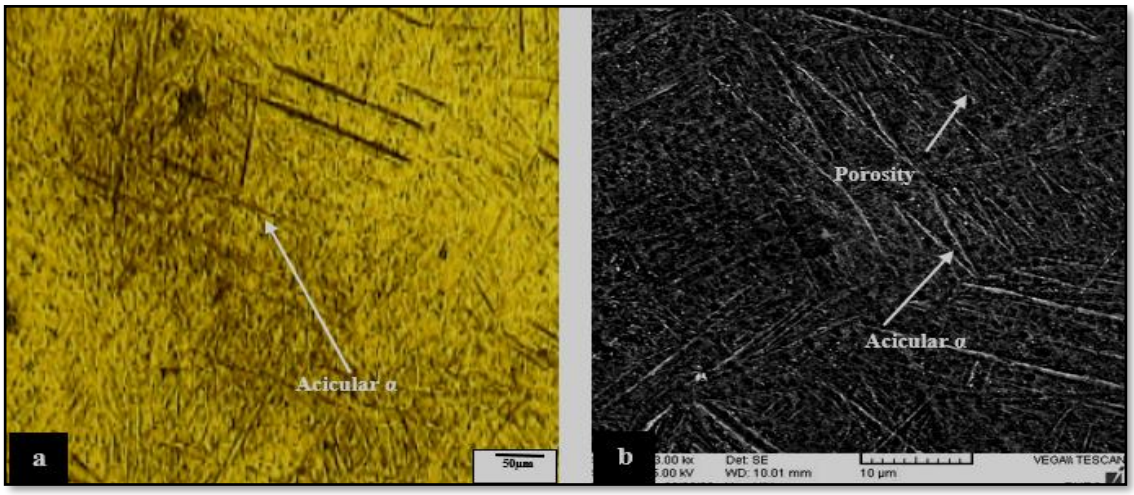

Figure (4.49): The FZ microstructure of the A28 weld using an (a): OM and (b): SEM.

Figure (4.50) shows that the HAZ microstructure of the B24 weld consists of a martensitic phase (acicular α`) near the FZ, and an acicular α` and primary α near the BM [111]. Figure (4.51) shows that the FZ microstructure of the B24 weld consists of an acicular α` due to the relatively high cooling rate. The cooling rate required for a full martensite phase to occur is above 410K⁰/s [114].

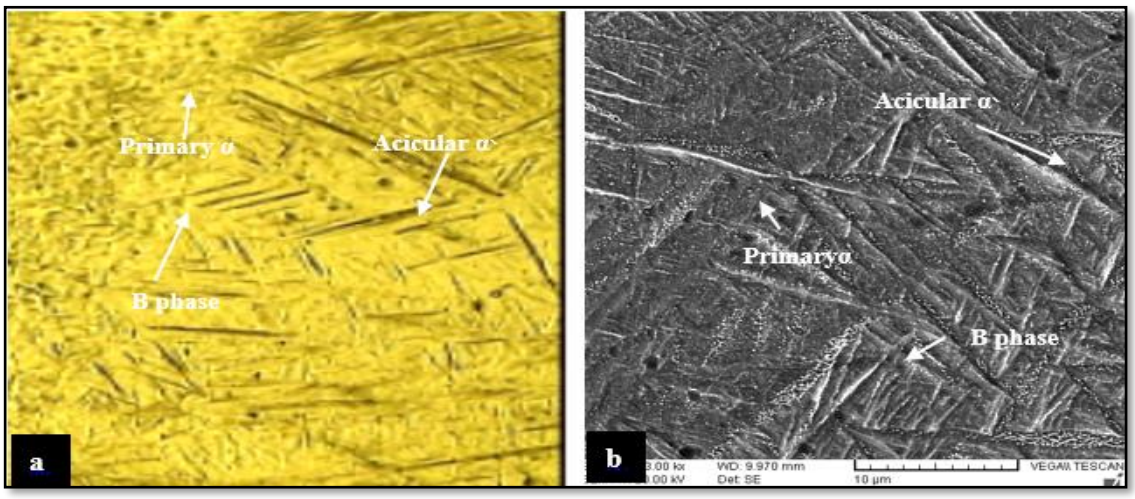

Figure (4.50): The HAZ microstructure of the B24 weld using an (a): OM and (b): SEM near the BM.

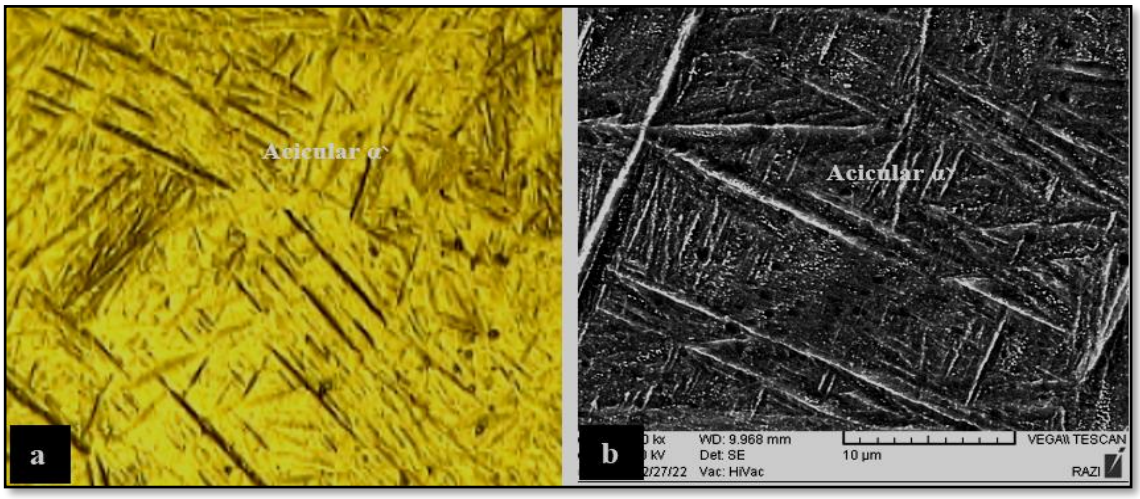

Figure (4.51): The FZ Microstructure of the B24 weld using an (a): OM and (b): SEM.

4.6 Mechanical Tests

4.6.1 Microhardness of the welds

Hardness is one of the most important mechanical properties that distinguish between materials. The hardness values of the welds depend on the microstructures formed during welding, and the size of the grains. In this study, Vickers microhardness was measured at different regions of the cross-section of the weld (Figure 3.11).

Figure (4.52) illustrates the hardness distribution across the A13 weld joined by the fiber laser. It was observed that the highest hardness value was in the weld center with an average of 353HV, then decreased to those of the HAZ before decreasing to those of the BM. The relatively high hardness in the FZ was due to the acicular α formed in this region.

The low heat input, and thus the high cooling rate led to the formation of fine acicular α grains in the FZ, which raised the hardness value, but it was not enough to form the martensite phase. The occurrence of the martensite phase requires higher cooling rates, or larger amount of stabilizers. The hardness of the CP-Ti mainly depends on the size of α grains due to the low

content of stabilizers. The HAZ hardness increased while advancing towards the FZ due to increasing the amount of acicular α. It was observed from the figure that the FZ and HAZ widths were small when the heat input was low.

Figure (4.53) shows the A12 weld hardness distribution. It was noticed that the average hardness value of the weld center was 268HV. It was also observed that the hardness decreased across this weld compared to the A13 due to the presence of a coarse acicular α because of the lower cooling rate. Increasing the heat input led to a grain growth, so the hardness decreased; this agrees with the [12]. For the same reasons the FZ and HAZ were wider than those of the A13 weld.

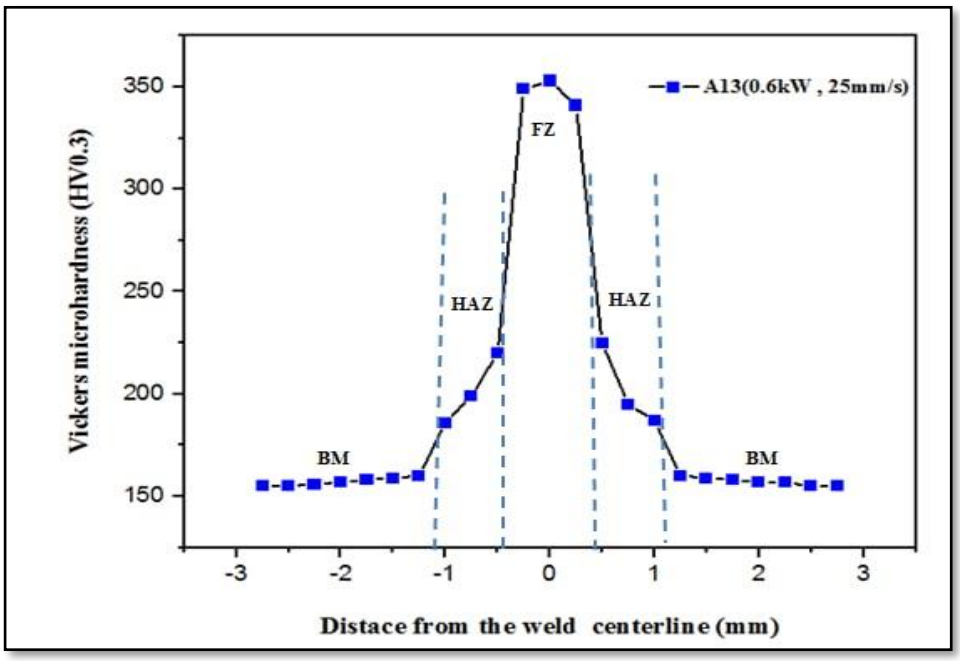

Figure (4.52): The hardness distribution across the A13 weld joined by the fiber laser.

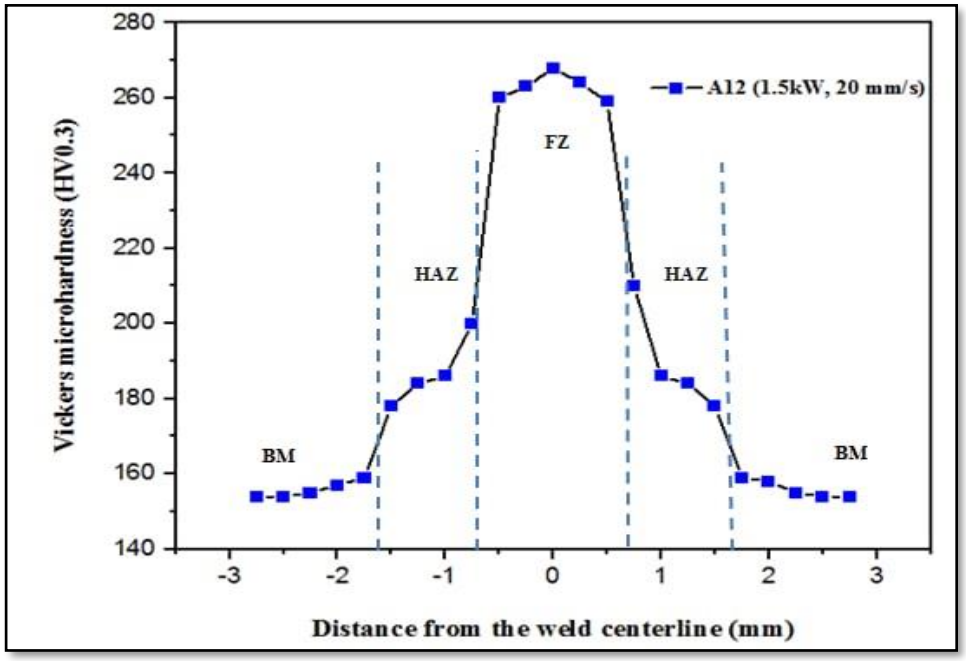

Figure (4.53): The hardness distribution across the A12 weld joined by the fiber laser.

Figure (4.54) illustrates the distribution of hardness across the A4 weld. It was observed that the hardness of this weld is lower than those of the A13 and A12 welds. Increasing the heat input to 150J/mm led to a lower cooling rate forming coarser grains. The hardness in the FZ of this weld was 230HV. It was also observed that the FZ and HAZ widths were larger than those of the A13 and A12 due to the higher heat input.

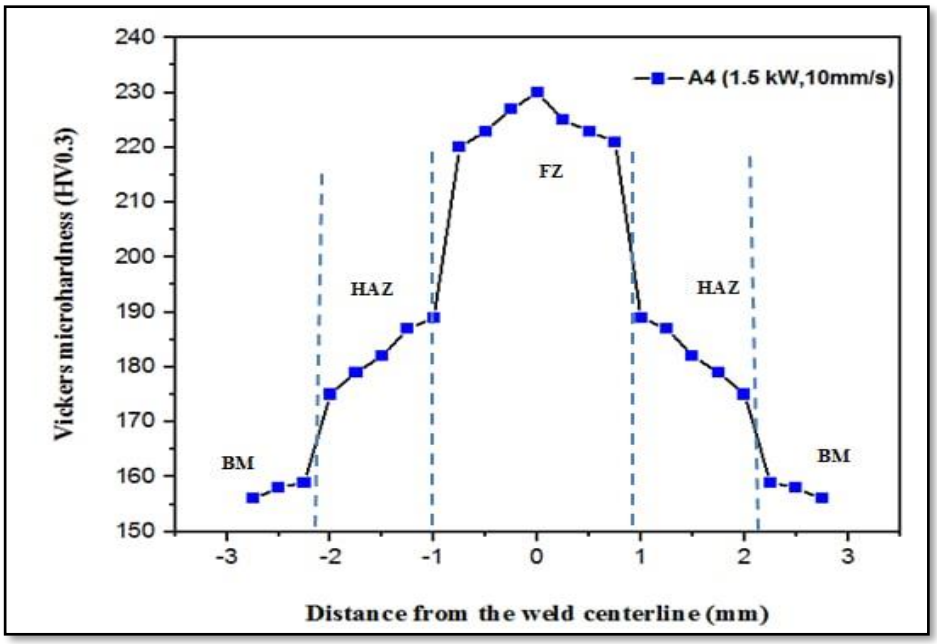

Figure (4.54): The hardness distribution across the A4 weld joined by fiber laser.

Figure (4.55) depicts the hardness distribution across the B13 weld. The average hardness value of the FZ was 478HV. This relatively high hardness value is due to the formation of acicular α` (martensite) phase as a result of the high cooling rate, and the presence of stabilizers. The hardness decreased by moving away from the FZ towards the HAZ due to the decrease in the amount of acicular α` formed; this agrees with [73,91].

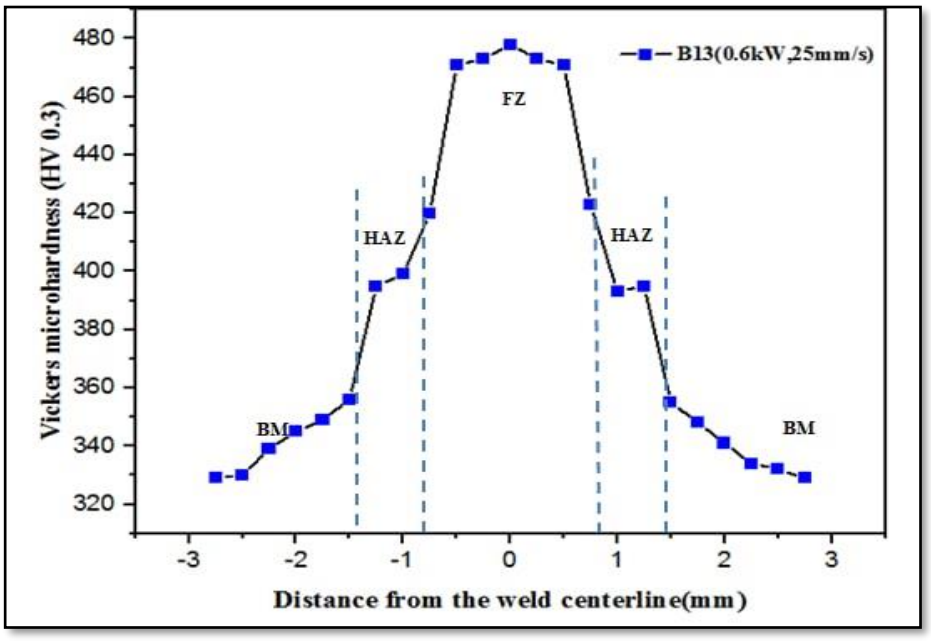

Figure (4.55): The hardness distribution across the B13 fiber weld.

Figure (4.56) shows that the hardness in the B12 weld center was 427HV. The hardness decreases with increasing the heat input due to the coarsening the acicular α` in the FZ and the HAZ. Figure (4.57) depicts the hardness distribution across the B4 weld. It was observed that the hardness in the weld center was 391HV. The gradual decrease in the martensite content while moving towards the BM was the cause of decreasing hardness values; this agrees with the [127]. It was also noted that the hardness across this weld was lower than that across the B13 and B12 welds, due to the coarseness of the grains formed as a result of the lower cooling rate. It can be concluded from the above that the hardness across the Ti-6Al-4V alloy fiber laser welds is remarkably higher than that across the CP-Ti welds due

to the formation of the hard acicular martensite as a result of the higher content of the stabilizers.

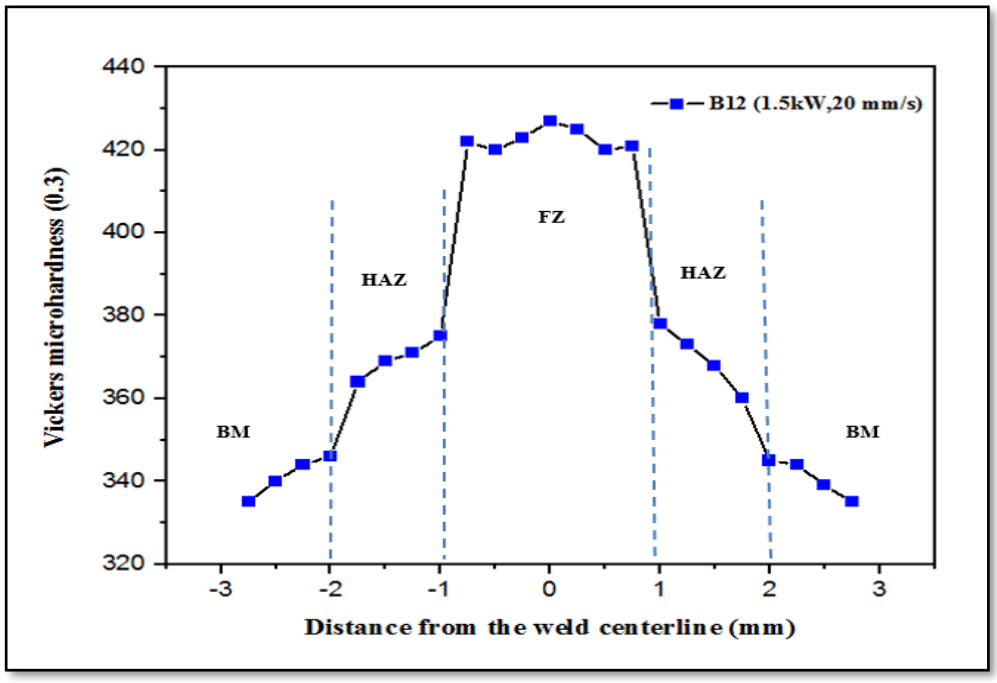

Figure (4.56): The hardness distribution across the B12 weld joined by fiber laser method.

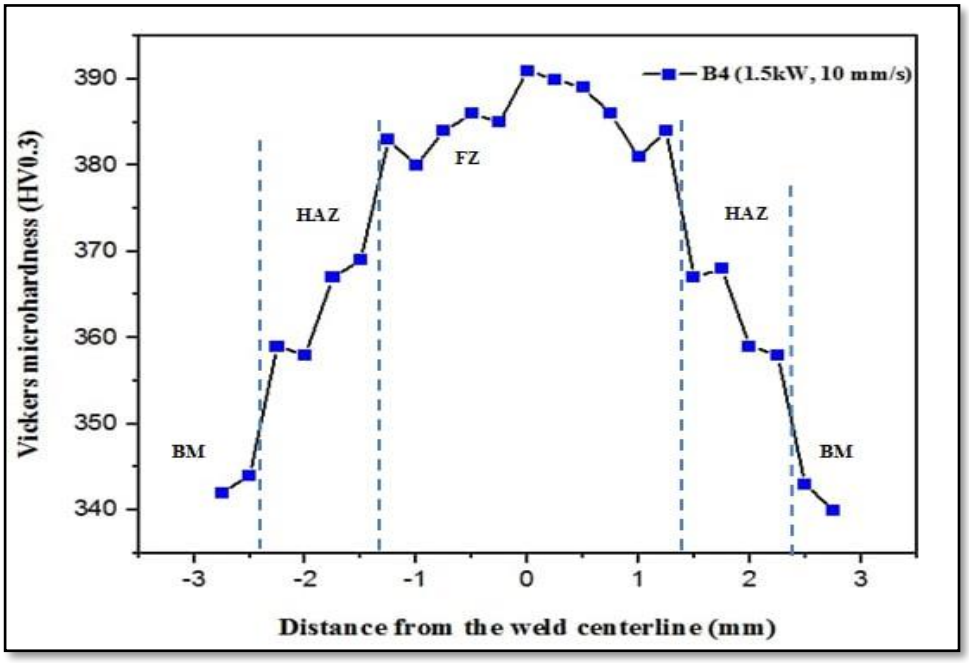

Figure (4.57): The hardness distribution across the B4 weld joined by fiber laser.

Figure (4.58) shows the Vickers microhardness distribution across the A29 weld joined by the pulsed Nd:YAG laser from both sides. It was noted from the figure that the highest hardness value was in the weld center with an average of 371HV, due to the fine acicular α formed as a result of the higher cooling rate. The amount of acicular α decreased while moving towards the BM. This corresponds to that revealed by the [109].

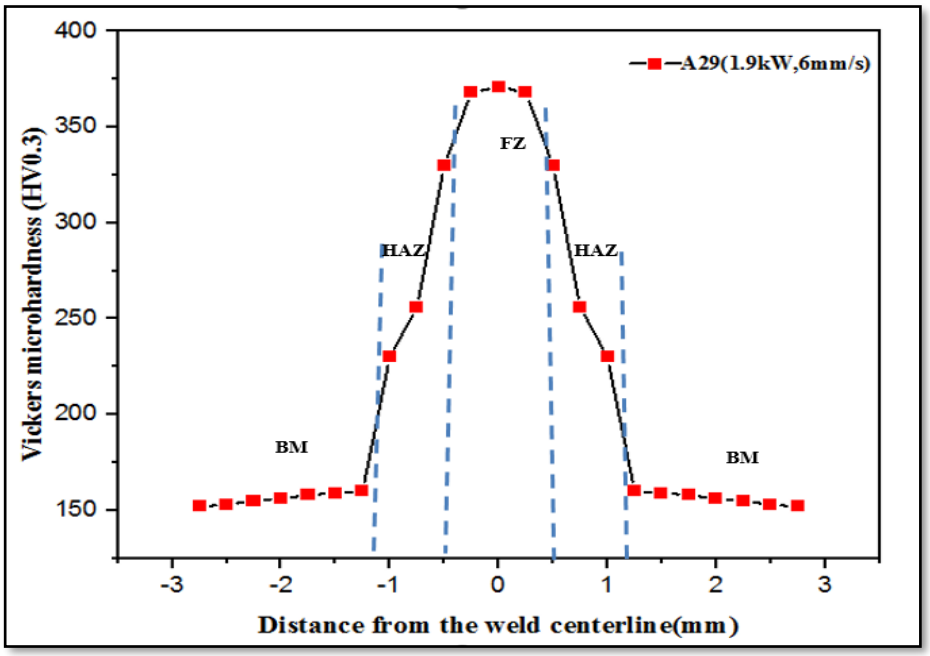

Figure (4.58): The hardness distribution across the A29 pulsed Nd:YAG laser weld.

Figure (4.59) demonstrates the microhardness distribution across the A28 weld. It was observed that the average hardness decreased compared to that across the A29 weld due to the increase in heat input; the hardness value of the weld center was 330HV. The microhardness distribution across the A20 weld showed in Figure (4.60) that the average hardness values in the weld center decreased to 240HV. The coarseness of the acicular α led to this lower hardness.

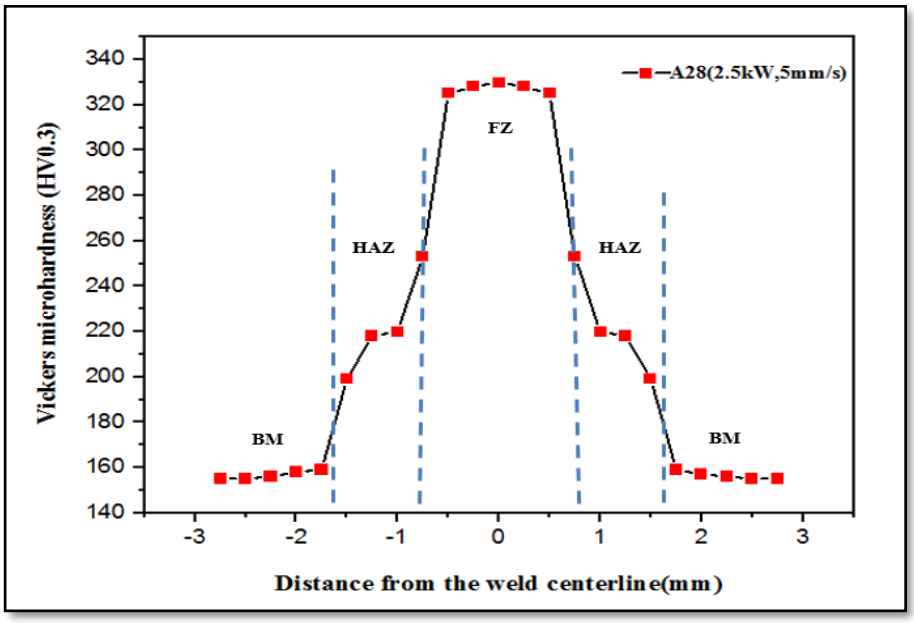

Figure (4.59): The hardness distribution across the A28 Nd:YAG laser weld.

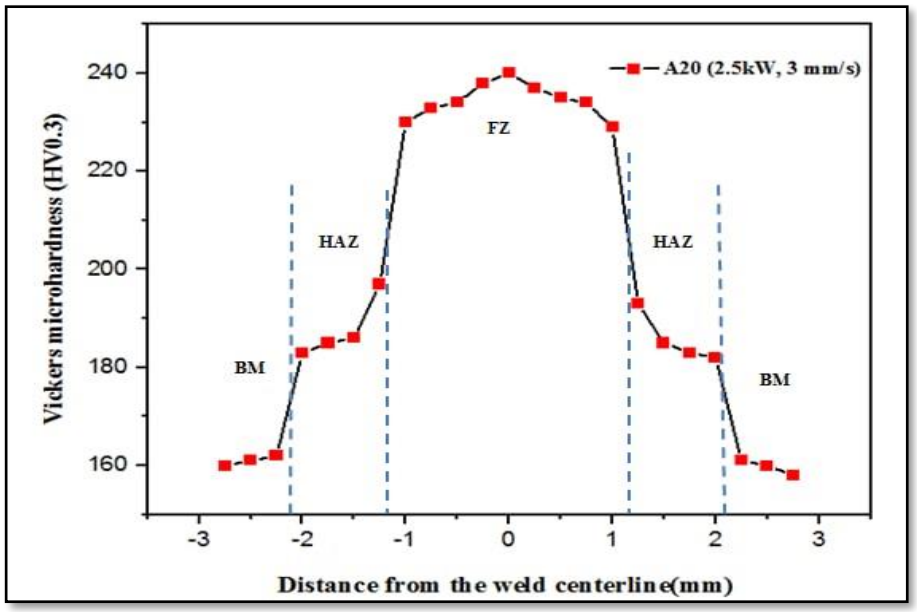

Figure (4.60): The hardness distribution across the A20 Nd:YAG laser weld.

On the other hand, the relatively high hardness in the FZ of the pulsed Nd:YAG laser Ti-6Al-4V welds is attributed to the large amount of martensitic phase formed in this zone, which decreases while moving towards the BM.

Figure (4.61) shows the microhardness distribution across the B29 weld. It was observed that the average hardness value in the weld center was 490HV. The relatively high hardness in the FZ could be attributed to the

presence of fine acicular α` (martensite) formed in this zone. The hardness distribution across the B24 weld showed in Figure (4.62) that the average hardness value in the weld center was 430HV. The reason behind the decrease in hardness is the decrease in the cooling rate, which led to growth of grains. The FZ consists of a coarse acicular α`, therefore the hardness values decrease, this agrees with the [127].

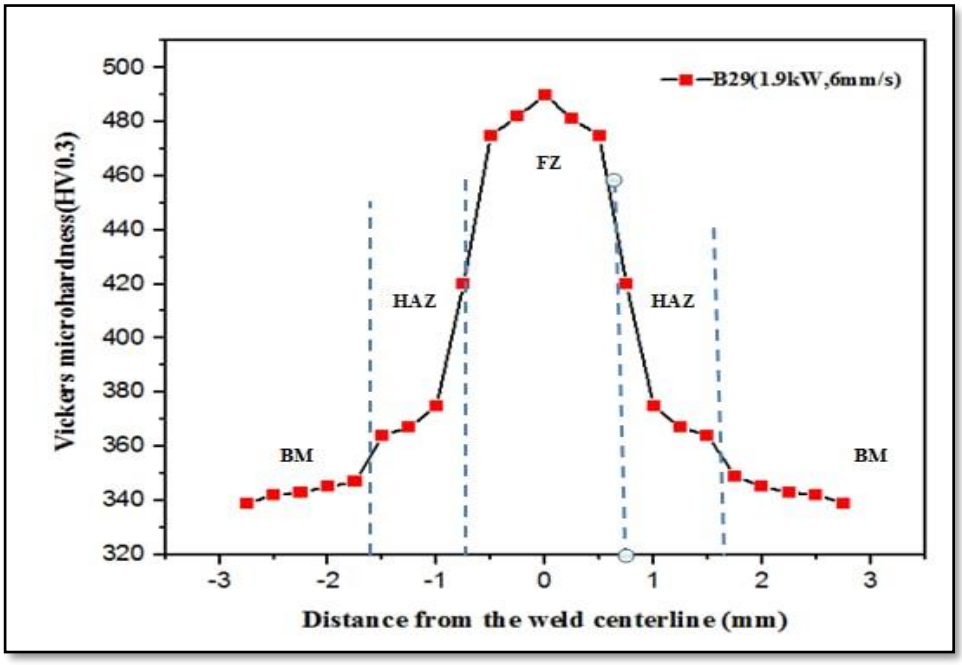

Figure (4.61): The hardness distribution of the B29 sample welded by Nd:YAG laser.

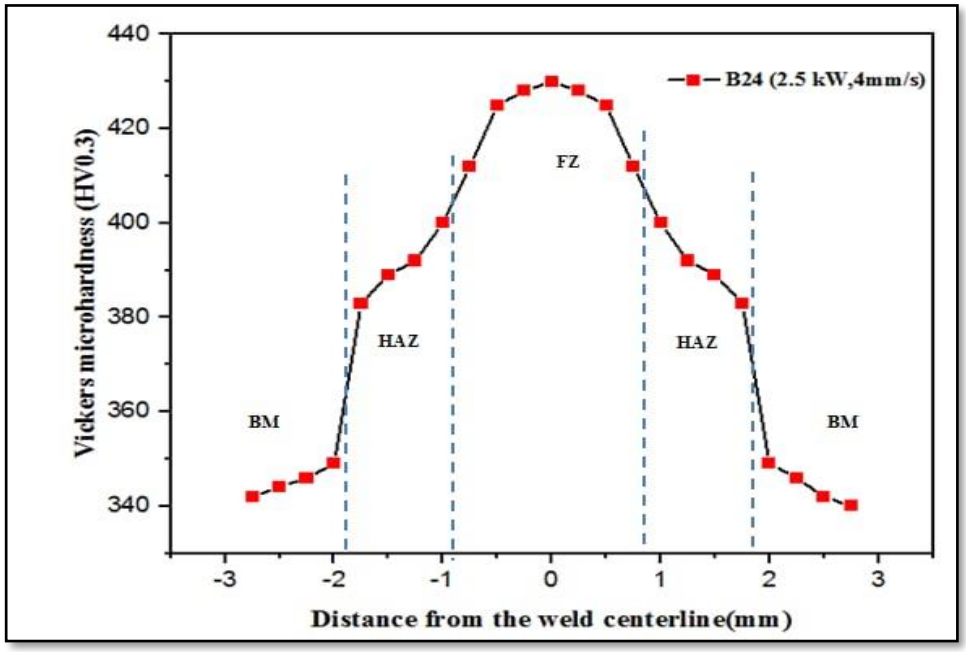

Figure (4.62): The hardness distribution across the B24 Nd:YAG laser weld.

Finally, Figure (4.63) demonstrates the hardness distribution across the B20 weld. The average hardness value of the weld center decreased to 410HV. The microstructure of the FZ became coarser due to the lower cooling rate associated with this weld. The hardness typically decreases due to the lack of grain boundaries, an impediment to the movement of dislocations [12].

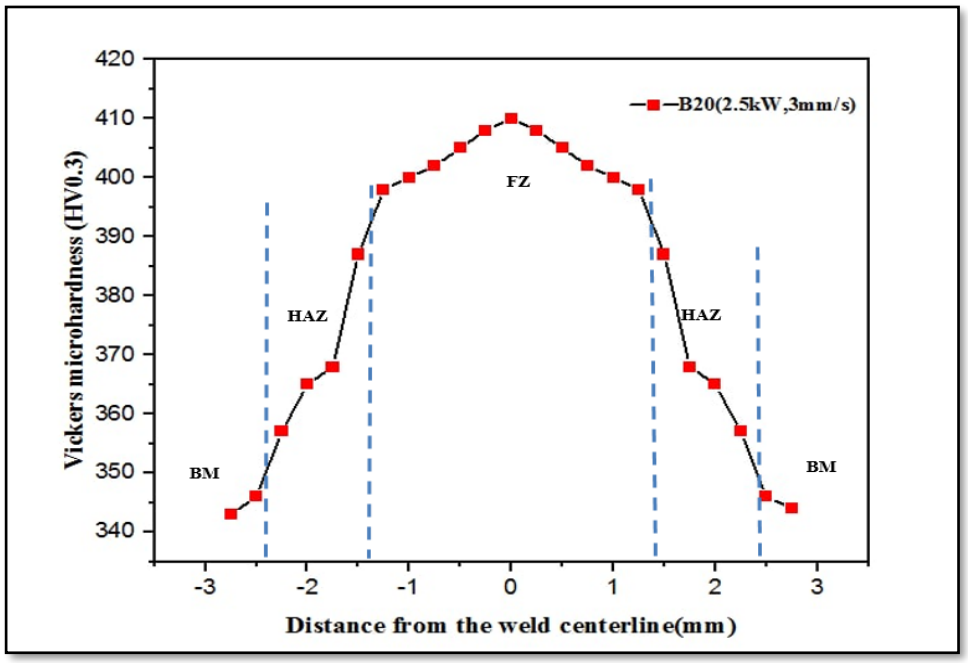

Figure (4.63): The hardness distribution across the B20 Nd:YAG laser weld.

As for the fiber welds, the hardness across the Ti-6Al-4V alloy Nd:YAG laser welds is significantly higher than that across the CP-Ti welds for the same reason mentioned earlier. However, the Nd:YAG laser welds exhibit hardness notably higher than the fiber laser welds.

4.7 Tensile Strength of the Welds

The average tensile strength of the CP-Ti and Ti-6Al-4V BM's were 752MPa and 1836MPa respectively. On the other hand, It can be noted that the most efficiencies of the weld joints were less than 100%. This might be attributed to one or more of the following reasons: the presence of

microspores, incomplete penetration, presence of brittle nature of martensitic microstructures, poor fusion and welding burn through [127].

Figures (4.64) and (4.65) demonstrate the effect of laser power and welding speed on the average tensile strength values of the CP-Ti and Ti-6Al-4V welds joined by the fiber laser. It was noted that the tensile strength is directly affected by the heat input. The maximum heat input is produced with the highest laser power and the lowest welding speed, and the increase in heat input leads to an increase in the grain size, and thus the tensile strength decreases; this corresponds to [12]. Reduction of the heat input to a certain extent increases the tensile strength due to the increased cooling rate, which results in finer grains, and thus increases grain boundaries. Another reason, the relatively high cooling rates result in acicular α in the CP-Ti welds and acicular martensite in the Ti-6Al-4V welds, which definitely increase the tensile strength of the welds.

In the case of the A13 weld, the tensile strength and weld joint efficiency were 429MP. This relatively low values were due to the incomplete penetration of the weld as a result of the lower laser power and higher welding speed; this agrees with the [14].

It was also noticed from Figure (4.64) that the highest average tensile strength value was 790MPa, for the A12 weld joined at a 1.5kW laser power and a 20mm/s welding speed, due to the balance between the LBW power and welding speed required necessary to obtain a good weld quality. However, the highest heat input resulted in a weld (A4) with a tensile strength of 608MPa on average.

On the other hand, for the fiber laser Ti-6Al-4V welds, Figure (4.65) shows that the maximum average tensile strength was 1639MPa for the B12 weld joined at a 1.5kW laser power and a 20mm/s welding speed. It was also observed that the lowest tensile strength was 230MPa for the B13 weld

joined with the lowest heat input, and thus incomplete penetration of the weld. The tensile strength of the B4 weld joined with the highest heat input was 370 MPa.

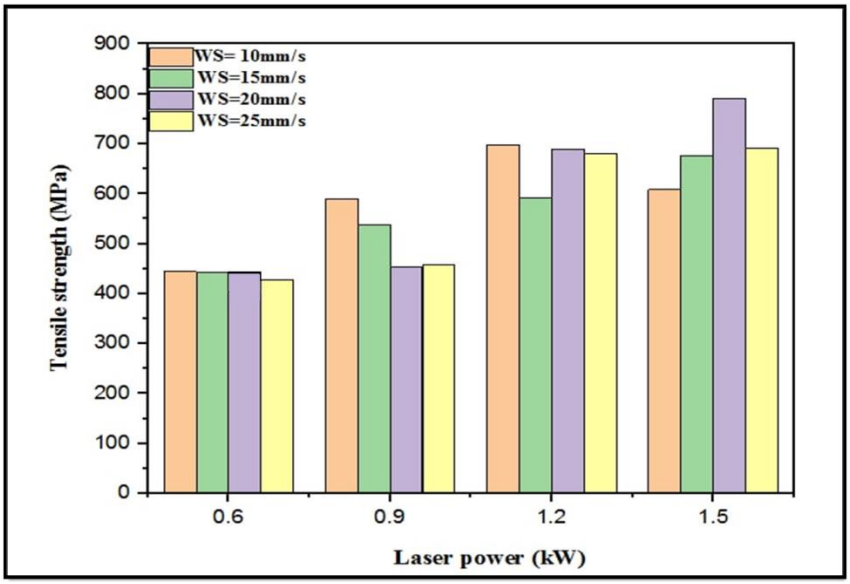

Figure (4.64): Effect of the laser power and welding speed on the tensile strength of the CP-Ti weld joined by the fiber laser method.

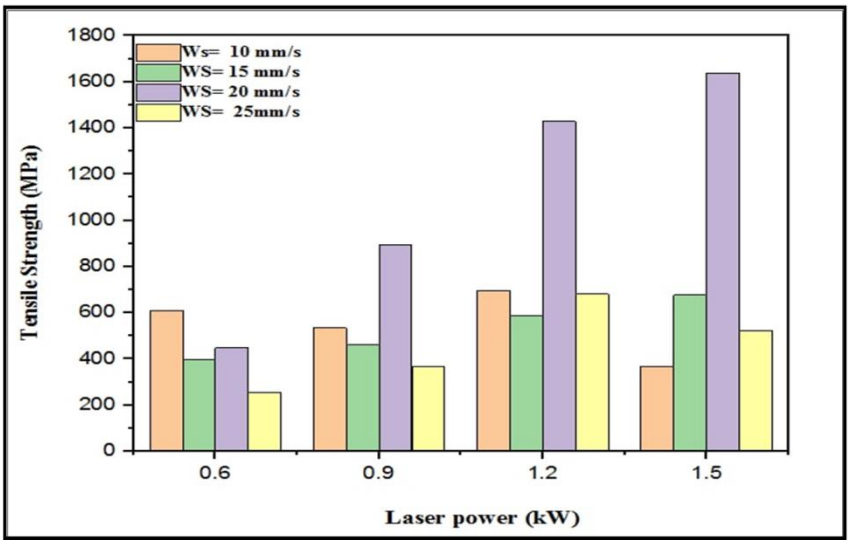

Figure (4.65): Effect of the laser power and welding speed on the tensile strength of the Ti-6Al-4V weld joined by fiber laser method.

Figures (4.66) and (4.67) show the average tensile strength values of the CP-Ti and Ti-6Al-4V welds joined by the Nd:YAG laser. It is observed that the maximum tensile strength value was 850MPa for the A28 weld joined at a 2.5kW laser power and a welding speed of 5mm/sec. This value might be due to the good penetration and to acicular α formation. The

lowest value of the average tensile strength was 293MPa for the A29 weld joined with a laser power of 1.9kW and a 6mm/s welding speed, which refers to the lowest heat input and the highest cooling rate, leading to an incomplete penetration. Moreover, the average tensile strength value was 480MPa for the A20 weld, might be due to formation of coarse martensite as a result of a lower cooling rate. It was also observed that the average tensile strength value of the B29 weld decreased to 480MPa due to a lack of weld penetration as a result of lower heat input. The average tensile strength value was 645MPa for the B20 weld joined at higher heat input. The maximum average tensile strength value was 1695MPa in the B24 weld due to a good penetration and fine martensite formed as a result of the high cooling rate.

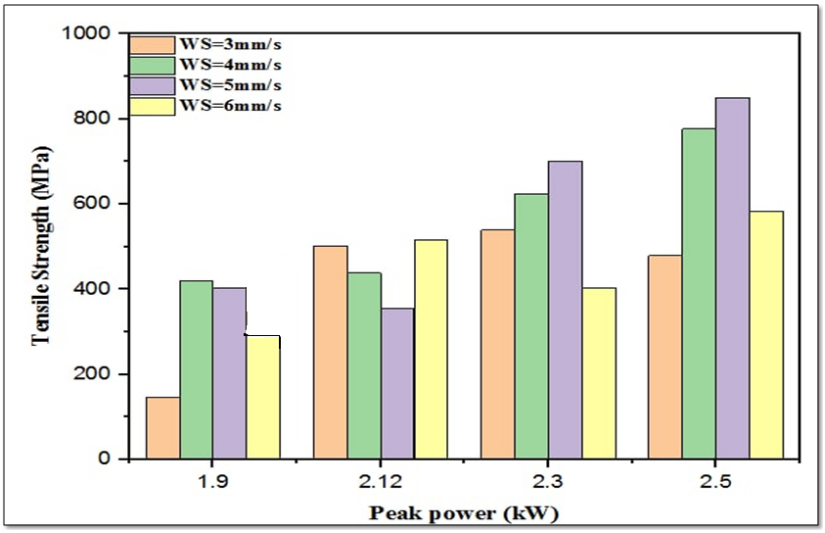

Figure (4.66): Effect of laser power and welding speed on the tensile strength of the CP-Ti weld joined by the Nd:YAG laser method.

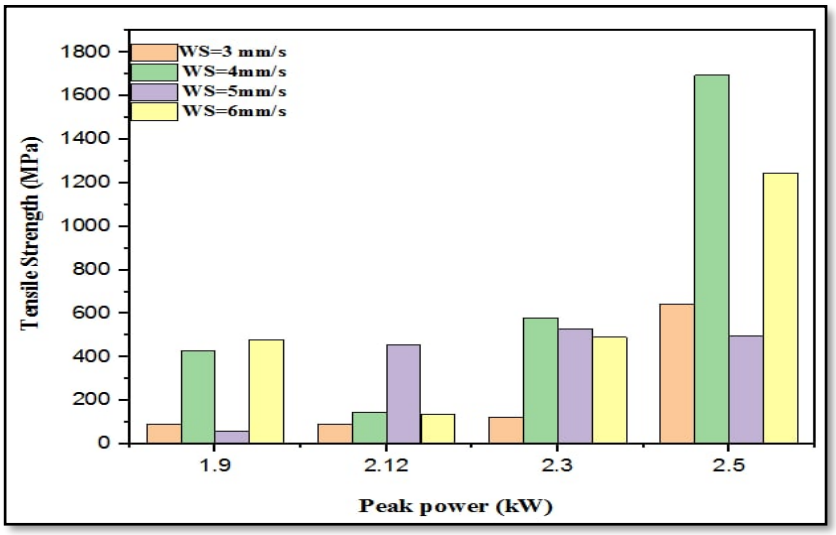

Figure (4.67): Effect of laser power and welding speed on the tensile strength of the Ti6Al4V weld joined by the Nd:YAG laser method.

4.8 Fractography Examination

The visual examination of the fracture surfaces of the samples after carrying out the tensile test showed that the samples welded by fiber and Nd:YAG laser had mostly brittle fractures, as shown in Figure (4.68). Some pores were also observed, which is consistent with the results of the X-ray examination. The samples on the left side of the figure, welded with minimal heat input, exhibited poor penetration, so the weld area was small, and the fractures appeared brittle. The samples in the middle of the figure, which were welded with the highest heat input, presented mostly brittle fractures. However, the samples on the right side of the figure that showed highest tensile strength values exhibited brittle-ductile mode fractures as shown in Figure (4.69).

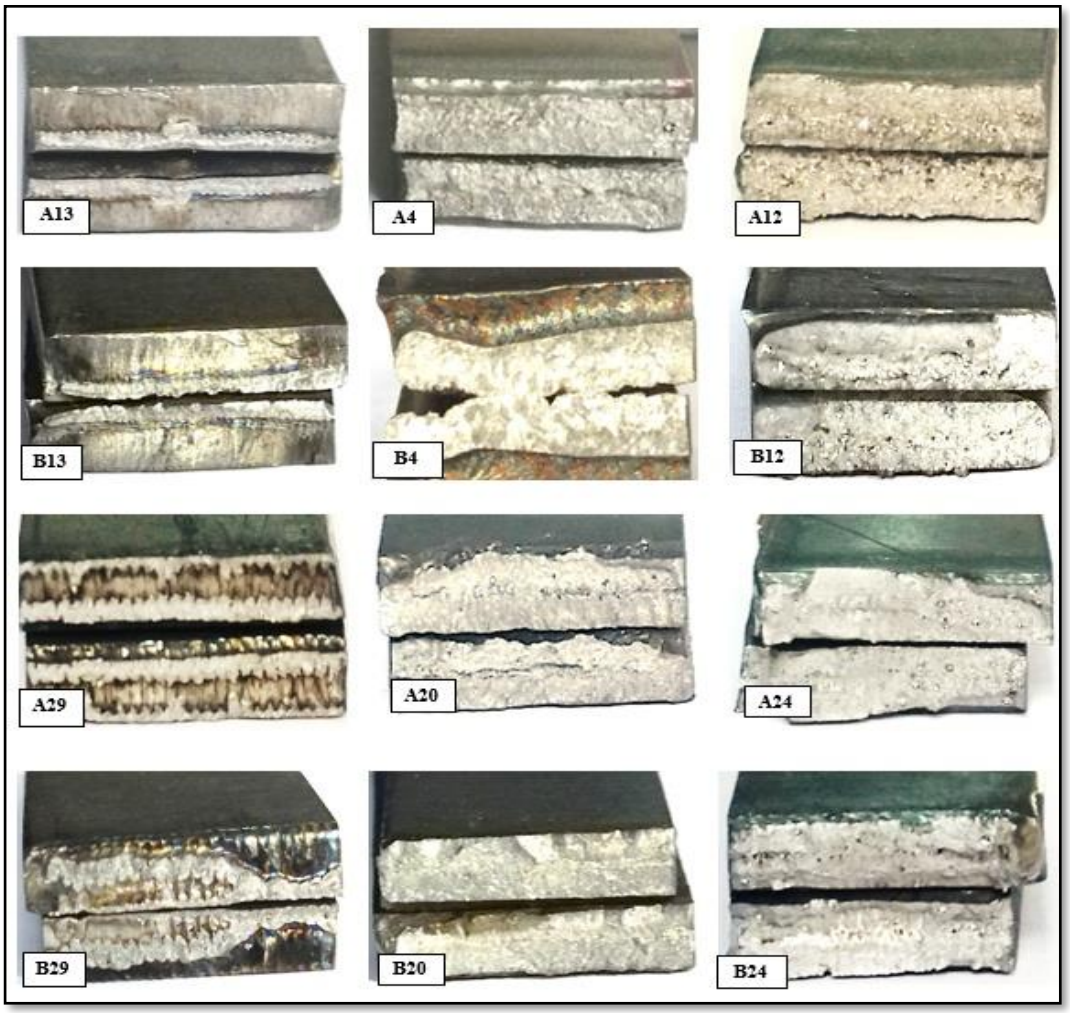

Figure (4.68): Fracture surfaces of the welds at the lowest heat input, highest heat input and the highest tensile strength.

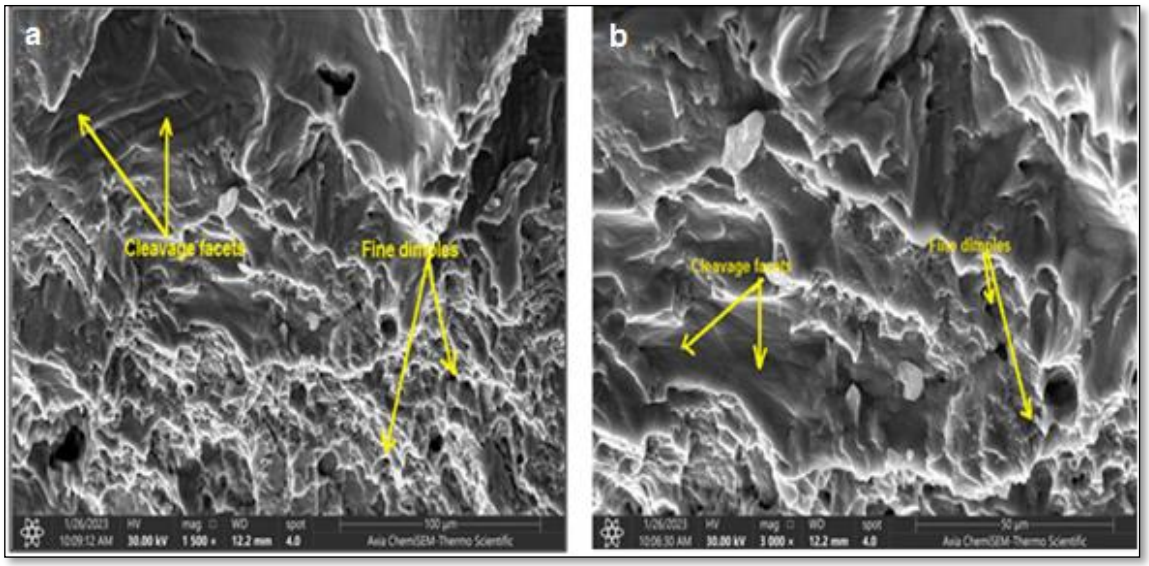

Figure (4.69): SEM fractography of the tensile specimens (a) A12 sample, (b) higher magnification image of sample welded by fiber laser methods.

Chapter Five

Conclusions and Future Recommendations

CHAPTER FIVE: CONCLUSIONS AND FUTURE RECOMMENDATIONS

5.1 Conclusions

Continuous fiber and pulsed Nd:YAG lasers were used for welding similar 3mm thick butt joints of CP-Ti and Ti-6Al-4V alloys. The most important results of this research can be concluded as follows:

1. The average HAZ width in fiber laser welds increased with the increase of laser power. The maximum average extent of the HAZ was 6.45mm and 6.69mm in the A4 and B4 welds respectively. Increasing the laser welding speed decreased the width of the HAZ. The HAZ's of the Ti-6Al-4V alloy welds were wider than those appeared in the CP-Ti welds.

2. The maximum penetration depths of the fiber CP-Ti and Ti-6Al-4V welds were 2.65mm and 2.75mm, respectively, at a laser power of 1.5kW and 10mm/s welding speed. On the other hand, the maximum depths of penetration of the Nd:YAG CP-Ti and Ti-6Al-4V welds, joined from both sides, were 2.75mm and 2.83mm respectively, at a peak power of 2.5kW and 3mm/s welding speed.

3. The geometry of the weld pool changed from a V-shape to an hourglass when the laser power was increased to 1.5kW and 2.5kW while using the fiber and Nd:YAG laser welding respectively, and vice versa when the welding speed was increased to 25mm/s and 6mm/s. The weld pool width was directly proportional to the increase in laser power, and inversely to the increase in welding speed for both methods.

4. The FZ microstructure of the CP-Ti laser welds consisted of acicular α, and there was no martensite formed. However, the FZ microstructure of the Ti-6Al-4V welds showed an acicular α` (martensite) phase.

5. The HAZ microstructure of the CP-Ti welds was mainly composed of acicular α near the FZ, which gradually decreased while moving towards the BM. On the other hand, the HAZ microstructure of the Ti-6Al-4V welds consisted of a small amount of acicular α` (martensite), primary α and β grains near the BM, and a large amount of acicular α` near the FZ.

6. The maximum average hardness values across the CP-Ti and Ti-6Al-4V welds joined using the fiber and Nd:YAG laser methods were in the weld center. Across all welds, the hardness decreased steeply while advancing towards the BM.

7. The hardness across the Nd:YAG laser welds was higher than that across the fiber welds, and was significantly higher across the Ti-6Al-4V welds than that across the CP-Ti welds.

8. The maximum average hardness values at the weld center of the CP-Ti and Ti-6Al-4V welds joined by the fiber and Nd:YAG laser method were 353HV, 478H, 371HV and 490HV respectively, which were associated with the lowest heat input.

9. For the CP-Ti welds joined by the fiber and Nd:YAG laser methods, the maximum average tensile strength values were 790MPa (A12) and 850MPa (A28) respectively, while for the Ti-6Al-4V alloy welds were 1639MPa (B12) and 1695MPa (B24) respectively. For both the CP-Ti and Ti-6Al-4V alloy welds, the highest tensile strength values were associated with the highest laser power and the welding speed sufficient for full penetration.

10.The most prominent defects observed in laser welds were the incomplete penetration and a few of porosity mainly related to the lowest heat input, in addition to deep craters associated with the highest heat input. There were no indications of cracks across all laser welds.

11. The fracture behavior of all laser welds was brittle, except the welds showed the highest tensile strengths were fractured with a brittle-ductile mode.

5.2 Future Recommendations

The results of this research can be used in future studies of laser welding processes for other titanium alloys, and some fields covered by this study can be modified in future. The following recommendations for future studies can be mentioned.

1. Investigation of the effect of pulsed Nd:YAG and fiber laser welding parameters on the wear and creep resistances of the CP-Ti and Ti-6Al-4V welds.

2. Studying the effect of using helium as a covering gas on the weld pool geometry and the mechanical properties of Ti alloy laser welds.

3. Investigating the effect of heat input on the mechanical and microstructural characteristics of the β- Titanium alloy welds joined by the CW fiber and CW Nd:YAG lasers.

References

References

1- Shaogang W. and Xinqiang W. (2012), *Investigation on the microstructure and mechanical properties of Ti–6Al–4V alloy joints with electron beam welding*, Materials and Design, Vol. 36, PP. 663–670.

2- Kazi B. A. and Abdul M. M. (2012), *Parametric Optimization of Machining Ti-alloys in Respect to Surface Roughness - A Review,* Applied Mechanics and Materials, Vols. 152-154, PP. 468-473.

3- An RTI International Metals, Inc. Company (2000), *Titanium Alloy Guide*, Staffordshire B78 3RW England.

4- Christoph L. and Manfred P. (2003), *Titanium and Titanium Alloys. Fundamentals and Applications*, Wiley-Vch, Germany.

5- Joseph A. (2016), *Experimental Characterization and Numerical Simulation of Fiber Laser Welding of AA2024-T3and Ti6Al4V*, A Thesis submitted for the Degree of Doctor of Philosophy of Imperial College London and Diploma of Imperial College.

6- Ali G. (2016), *Crack risk in Nd: YAG laser welding of Ti-6Al-4V alloy,* Materials Letters, Vol. 197, PP. 2 33-235.

7- Yassin M. A., Khairul S. M. S., Mahadzir I. and Basim Ali K. (2014), *Titanium and its Alloy*, International Journal of Science and Research (IJSR), Vol.3, PP. 1351 – 1361.

8-ASM handbook (1993), *Welding, Brazing and Soldering*, Vol. 6.

9-Cui L., Bin L., Ze-feng W., Xiao-yong Q., Bing Y. and Ai-hua W. (2017), *Stitch welding of Ti−6Al−4V titanium alloy by fiber laser,* Transactions Nonferrous Metals Society of China, Vol.27, PP.91-101.

10- Malis K. P. R., Ramawath P. N., Madhukar S. and Chelluboina H.K. (2020), *Review on different welding techniques of Titanium and its alloys,*

International Journal of Scientific Research in Science, Engineering and Technology (IJSRSET), | Vol., Print ISSN: 2395-1990.

11-Bibhudutt A. B. (2014), *Laser Beem Welding of Commercially Pure Titanium Sheets,* A thesis submitted in partial fulfillment of the requirements for the degree of Master Technology in Materials Engineering, National Institute of Technology, Rourkela.

12-Muralimohan C., Divi V., Pendyala. N. R., Senthil K.S. and Narayanaswami S. (2019), *Effect of Process Parameters and Heat Input on Weld Bead Geometry of Laser Welded Titanium Ti-6Al-4V Alloy,* Journal of Materials Science Forum, Vol. 969, PP. 613-618.

13- Auwal S. T., Sadagoppan R., Farazila Y. and Sunusi M. M. (2018), *A review on laser beam welding of titanium alloys*, Journal of The International Journal of Advanced Manufacturing Technology, Vol. 97, PP. 1071–1098.

14- Chandan K., Manas D., Paul C.P. and Singh B. (2017), *Experimental investigation and metallographic characterization of fiber laser beam welding of Ti-6Al-4V alloy using response surface method*, Journal of the Optics and Lasers in Engineering, Vol. 95, PP. 52–68.

15-Elijah K-A.j. (2009), *Principles of Laser Welding Materials Process*, John Wiley & Sons, Inc, Hoboken, New Jersey.

16- Seiji K. (2020), *Fundamentals and Details of Laser Welding*, Springer Nature Singapore Pte Ltd.

17-Monika L. (2014), *Advanced Materials*, VŠB – Technical University of Ostrava.

18- Pei-quan. X. () , *Microstructure characterization of Ti−6Al−4V titanium laser weld and its deformation*, Journal of Transactions of Nonferrous Metals Society of China, Vol. 22, PP.2118−2123.

19- Lisiecki A. (2012), *Welding of titanium alloy by different types of lasers*, Journal of Archives of Materials Science and Engineering**,** Vol. 58,

PP.209-218.

20- Lisiecki A. (2012), *Laser Welding of Titanium Alloy Ti6Al4V Using A Disk Laser*, International Virtual Journal Machines, Technologies, Materials,Vol.7 PP. 53-56.

21- Krebs, Robert E. (2006), *The History and Use of Our Earth's Chemical Elements*: A Reference Guide (2nd edition). Westport, CT: Greenwood Press.

22- Akman E. and Demir A. (2009), *Laser welding of Ti6Al4V titanium alloys*, Journal of Materials Processing Technology, Vol. 209, PP. 3705-3713.

23- David H. P. (2016), *Welding Engineering .An Introduction***,** John Wiley & Sons, Ltd**.**

24- Matthew J. Donachine, Jr. (2000), *Titanium ATechnical Guide,* ASM International.

25- Sakari T. (2018), *Welding of Ti-6Al-4V: Influence of welding process and alloy composition on microstructure and properties*, Thesis for the Degree of Doctor of Philosophy, Department of Industrial and Materials Science Chalmers University of Technology Gothenburg, Sweden.

26- Jianglin H. (2011), *The Characterization and Modelling of Porosity Formation in Electron Beam Welded Titanium Alloy,* A dissertation submitted to The University of Birmingham for the degree of Docter of Philosophy.

27- Patrizia B., Liang-Yu C., Juliana D. C. T., Andréa C. R., Facundo A. and Paola L. (2021), *Passive Layers and Corrosion Resistance of Biomedical Ti-6Al-4V and β-Ti Alloys,* Journal of Coatings, Vol.11, PP. 487.

28- Motyka.M, Kubiak K., Sieniawski J. and Ziaja W. (2014), Phase Transformations and Characterization of α+β Titanium Alloys, Journal of Comprehensive Materials Processing, Vol 2.PP.7-36.

29- Maciej M., (*2021),* Martensite Formation and Decomposition during Traditional and AM Processing of Two-Phase Titanium Alloys—An Overview, Journal of Metals, Vol. 11, PP. 48.

30- Navneet K. (2017), *Experimental evaluation of the effect of workpiece heat treatments and cutting parameters on the machinability of Ti-10V-2Fe-3Al β titanium alloy using Taguchi's design of experiments*, Journal of International Machining and Machinability of Materials, Vol. 19, No. 4.

31- Seyedvahid S. (2017), *Thermo-Mechanical Behavior of Severely Deformed Titanium*, Thesis Submitted to the Graduate School of Sciences and Engineering In Partial Fulfillment of the Requirements for the Degree of Doctor of Philosophy, Department of Mechanical Engineering Özyeğin University.

32- Sani A. S. Suleimanb I. Y. and Eyinavia I.A. (2019), *Classification, Properties, Applications of Titanium, and Its Alloys used in Automotive industry- A Review*, American Journal of Engineering Research (AJER), Vol.8, PP. 92-98.

33- Boyer R. R. (2010), *Attributes, characteristics, and applications of titanium and its alloys,* Journal of Titanium Processing, Vol. 62, PP.21–24.

34-Barriobero-Vila P. (2015), *Phase Transformation Kinetics During Continuous Heating of α+β and Metastable β Titanium Alloys*, Thesis Submitted to the Graduate School of Sciences and Engineering In Partial Fulfillment of the Requirements for the Degree of Doctor of Philosophy Materials Science and Technology (IMST) of the Vienna University of Technology (TU Wien).

35- Gerd L. and James C. W. (2007), *Titanium*, 2nd edition, Springer-Verlag Berlin Heidelberg.

36- Vydehi A. J. (2006), *Titanium Alloys, An Atlas of Structures and Fracture Features*, Taylor & Francis Group.

37- Brian A. W. (2010), *Microstructural and Property Relationships in - Titanium Alloy Ti-5553,* Thesis Presented in Partial Fulfillment of the

Requirements for the Degree Master of Science in the Graduate School of The Ohio State University.

38-Marcio W. B S. (2019), Investigation of the Mechanical Behaviour and Microstructural Evolution of Titanium Alloys UndersuperPlastic and Hot Forming Conditions, Thesis, In Partial Fulfillment of the Requirements for the Doctorate Dell ''Universities De Toulouse.

39- Merve N. D. (2019), *Production of TI-6AL-4V Alloy by 3D Electron Beam Melting Technique and Development of Its Post Treatments*, A Thesis, In Partial Fulfillment of the Requirements for the Master's Degree of Science in Metallurgical and Materials Engineering Submitted to the Graduate School of Natural and Applied Sciences of Middle East Technical University.

40- Edgar J. R. R. (2010), *Effect of Boron on the Microstructure and Properties of Ti-6Al-4V*, A Thesis, In Partial Fulfillment of the Requirements for the Master's Degree of Science in Metallurgical and Materials Engineering Submitted to the Department of Applied Physics and Mechanical Engineering Division of Engineering Materials, Lulea University of Technology, Sweden.

41- *Tim* P., *Yuan* T., *Mana* A., *Osamu* K., *Masami* M. and *Wojciech* M., (2017), Welding of titanium alloys, International Conference on Precision Machinery and Manufacturing Technology (ICPMMT).

42- Timotius P., Yuan T, Osamu K., Yasuyuki M. and Gakuya K. (2014), Research on Various Welding Methods on Aerospace Titanium Alloys: collaboration between Akita University and AUT University, International Journal of the Society of Materials Engineering for Resources, Vol. 20, PP. 35-39.

43- Saroja S., Vijayalakshmi M. and Baldev R. (2012), Ti–5Ta–1.8Nb: An Advanced Structural Material for High-Performance Application in Aggressive Oxidizing Environments, Journal of Transactions of the Indian Institute of Metals, Vol. 65, PP.111–133.

44- Auwal T.S., S. Ramesh S., Yusof F. and Manladan M.S. (2018), A review on laser beam welding of copper alloys, The International Journal of Advanced Manufacturing Technology, Vol. 96, PP.475–490.

45-Md I.K. (2007), Welding Science and Technological ,New Age International Publishers.

46- Ready F.J. (1997), Industrial Applications of Lasers", Academic Press, USA, 1997.

47-Ifflander R. (2001), Solid-State Lasers for Materials Processing, Springer, New York, NY.

48-Weaam M .M.J. (2020), *Experimental and Optimization Investigation of Laser Welding Parameters for Similar and Dissimilar Ti and Ti6Al7Nb Alloy Sheets*. A Thesis Submitted to College of Materials Engineering of University of Babylon in Partial Fulfillment of Requirements for the Degree of Doctor in Materials Engineering /Metals.

49-Seiji K., (2013), *Handbook of Laser Welding Technologies*, Wood head Publishing Limited, India.

50-Akshay G., Hemant D., Vivek K., Akshay P. and Ankita V.,(2017), *Review on Laser Welding of Titanium Alloy*, International Conference on Ideas, Impact and Innovation in Mechanical Engineering (ICIIIME 2017),Vol. 5.

51-Elijah K. A. J. (2009), *Principles of Laser Materials Processing*, John Wiley & Sons, Inc., Hoboken, New Jersey.

52-George C. (1991), *Laser Machining Theory and Practice*, Springer Science and Business Media New York.

53- Rasha K. M. Al-Dabbagh. (2007)*Analytical composition between Laser Beam and Electron Beam Welding*, A Thesis Submitted to the College of Engineering of Nahrain University in Partial Fulfillment of the Requirements for the Degree of Master of Science in Laser and Optoelectronics Engineering.

54- Khalid M. Abed Umaish. (2014), *Dissimilar Metals Stainless Steel AISI 304H, to Low Carbon Steel DIN St33 Welding by Pulsed Nd :YAG Laser*, A Thesis Submitted to College of Materials Engineering of the University of Babylon in Partial Fulfillment of Requirements for the Degree of Master of Science in Metallurgical Engineering.

55- Donato C., Antonio D. and Donato S. (2022), *Numerical Study on the Influence of the Plasma Properties on the Keyhole Geometry in Laser Beam Welding,* Journal of the Frontiers in Physics, Vol.9.

56- Motlagh H.S.N., Parvin P., M.Jandaghi P. and Mohammed J.T.(2013), *The Influence of Different Volume Ratios of He and Ar in shielding gas mixture on the power was Temperatures for Nd: YAG andCO2 laser welding,* Journal of Optics&LaserTechnology, Vol. 54, PP.191–198.

57- Volpp J. (2018), *Impact of fume particles in the keyhole vapor*, Journal of the Applied Physics A, Vol. 125, PP.70.

58- Seiji K. and Yousuke K. (2009), Elucidation of Phenomena in High Power Fiber Laser Welding, and Development of Prevention Procedures of Welding Defects, Proceedings of SPIE - The International Society for Optical Engineering, Vol. 7195.

59-Yu F. (2010), *Mechanical properties of laser beam welded Ti6Al4V*, Thesis Submitted to the University of Nottingham for the degree of Doctor of Philosophy.

60- Meda L.N., Cosmin S., Dalibor C., Laurentiu C., Mihai R., and Daniela M. (2008), *Repairing method of fixed partial prostheses in dentistry: laser Welding*, Proceedings of SPIE - The International Society for Optical Engineering.

62- Jae Y. L., Sung H. K., Dave F. F. and Choong D. Y.,(2002) *Mechanism of keyhole formation and stability in stationary laser welding*, Journal of Physics D:Applied Physics, Vol. 35,PP.1570–1576.

63-Stanciu M.E., Păvălache.C.A., DumitruM.G., DontuG.O., Besnea D. and Vasile M.I. (2010), *Mechanism of Keyhole Formation in Laser Welding*, Journal of The Romanian Review Precision Mechanics, Optics & Mechatronics, Vol.20.

64- Aalderink J.B., Lange F., RGKM A. and MeijerJ. (2007), *Keyhole shapes during laser welding of thin metal sheets*, Journal of Physics D: Applied Physics, Vol.40, PP. 5388–5393.

65-Sinuhe` H. (2010), Laser Welding of Hardenable Steel, Thesis Submitted to the Lulea University Department of Applied Physics and Mechanical Engineering Division of Engineering Materials, as Partial Fulfillment of the Requirements for the Degree of Master.

66-Walter K. (2006), *Solid-State Laser Engineering Sixth Revised and Updated Edition*, Springer Science and Business Media, Inc.

67- BenyounisY.K.*, OlabiK.A. and M. S. J. Hashmi J.S.M. (2005), Effect of laser-welding parameters on the heat input and weld-bead profile, Journal of Materials Processing Technology**,** Vol**.** 164–165**,** PP.978-985**.**

68- Tadamalle A.P, Reddy Y.P. and Ramjee, E. (2013), Influence of laser welding process parameters on weld pool geometry and duty cycle, Journal of Advances in Production Engineering & Management, Vol. 8, PP. 52–60.

69- Abdel-Monem El-Batahgy, Abdel-Fattah K. and Thoria S. (2011), Effect of Laser Beam Welding Parameters on Microstructure and Properties of Duplex Stainless Steel, Journal of *Materials Sciences and Applications*, Vol.2, PP. 1443-1451.

70-Masoud H., Fanrong K., Blair C. and Radovan K. (2012), *Studying the Effect of Laser Welding Parameters on the Quality of ZEK100 Magnesium Alloy Sheets in Lap Joint Configuration*, Conference: 31st International Congress on Applications of Lasers & Electro-Optics, ICALEO At: Anaheim, USA.

71- Hui-Chi C. (2010), *Fiber Laser Welding of Dissimilar Materials*, A thesis submitted to The University of Manchester for the PhD degree in the Faculty of Engineering and Physical Sciences**.**

72- William M. S. and yotirmoy M. K. (2010), Laser Material Processing, Springer-Verlag London Limited.

73- Giuseppe C., Michelangelo M. and Sabina L. C. (2015), *Ytterbium fiber laser welding of Ti6Al4V alloy*, Journal of Manufacturing Processes, Vol.20, PP. 250-256.

74- Ahn J., Chen L., Davies M.C. and Dear P.J. (2016), Parametric optimization and microstructure alanalysis on high power Yb-fibre laser welding of Ti–6Al–4V, Journal of Optics and Lasers in Engineering,Vol. 86,PP.156–171.

75-Nasir A. (2005), New Developments in aAdvanced Welding, Wood head Publishing Limited Cambridge England.

76- Abu Syed H. K. (2011), *Nd:YAG Laser Welding of Ti-6Al-4V Alloy*, A Thesis Partial Fulfilment of the Requirements for the Degree of Master of Applied Science (Mechanical Engineering) at Concordia University.

77-Seiji K. (2020), Fundamentals and Details of Laser Welding, Springer Nature Singapore Pte Ltd.

78- Mende J., Schmid E., Speiser J., Spindler G. and Giesen A. (2015), *Thin-disk laser – Power scaling to the kW regime in fundamental mode operation,* Conference Paper *in* Proceedings of SPIE - The International Society for Optical Engineering.

79- Shankarling S.G. and Jarag J.K. (2010), *Laser Dye Journal of Resonance,* Vol. 15, PP. 804-818**.**

80- Britt El., Gihleengen, Lasse T. and Kim A. G. (2007),*Semeconducter Lasers.*

81- Sabina L. C., Giuseppe C., Michelangelo M., Andrea A. and Antonio D. L. (2015), *Microstructural characteristics and mechanical properties of*

Ti6Al4V alloy fiber laser welds, Journal of Procedia CIRP,Vol. 33,PP. 428 – 433.

82- Turichin G., Tsibulsky I., Somonov V., Kuznetsov M. and Akhmetov A. (2016), *Laser-TIG Welding of Titanium Alloys*, VII International Scientific-Practical Conference "Innovative Technologies in Engineering IOP Conf. Series: Materials Science and Engineering 142.

83- Kamal K. K. (2011), An Investigation of Dissimilar Welding Joint of AISI 304L Stainless Steel with Pure Copper by Nd:YAG Pulse Laser: Optimization of Tensile Strength, A Thesis Submitted in Partial Fulfillment of the Requirement for the Degree of Master of Technology in Mechanical Engineering (Specialization: Production Engineering).

84- John C. L. (2015), *Welding Metallurgy and Welding* , John Wiley & Sons, Inc., Hoboken, New Jersey.

85- Sindo K. (2003*), Welding Metallurgy Second Edition*. Hoboken, NJ.

86-Easterling E.K. (1992), *Introduction to the physical metallurgy of welding*. Butterworth Heinemann.

87- Lathabai S., Jarvis L.B. and Barton J.K. (2001), *Comparison of keyhole and conventional gas tungsten arc welds in commercially pure titanium*, Journal of Materials Science and Engineering,Vol. A299,PP. 81–93.

88- Fabrizia C., Vittorio A., Gaetano C., Francesco C. and Vincenzo S. (2013), *Investigation and Optimization of Laser Weiding of Ti-6Ai-4 V Titanium*, Journal of Manufacturing Science and Engineering, Vol.135.

89- Chamanfar A., Pasang T.,Ventura A. and Misiolek Z.W. (2016), *Mechanical Properties and Microstructure of Laser Welded Ti–6Al–2Sn–4Zr–2Mo (Ti6242) Titanium Alloy*, Journal of Materials Science & Engineering A, Vol. 663, PP. 213-224.

90- Cao X. and Jahazi M. (2009), *Effect of welding speed on butt joint quality of Ti–6Al–4V alloy welded using a high-power Nd:YAG laser*, Journal of Optics and Lasers in Engineering, Vol. 47, PP. 1231–1241.

91- Pramod K. and Amar N. S. (2018), *Effect of heat input in pulsed Nd:YAG laser welding of titanium alloy (Ti6Al4V) on microstructure and mechanical properties*, Journal of International Institute of Welding, Vol. 63, PP.673–689.

92- Jonathan E. B. (2011),*Understanding Porosity Formation and Prevention when Welding Titanium Alloys with 1µm Weave length Laser Beam*, thesis submitted to The University of Manchester for the degree of Doctor of Engineering in the Faculty of Engineering and Physical Sciences.

93-Amit K. (2006), *Tailoring Deffect Free Fusion Welds Based on Phenomenological Modeling*, AThesis to Materials Science and Engineering Submitted in Partial Fulfillment of the Requirements for the Degree of Doctor of Philosophy.

94- Jun Z.,and Hai-Lung T.,(2007), *Porosity Formation and Prevention in Pulsed Laser Welding,* Journal of Transactions of the ASME,Vol.129.

95- Shengyong P., Weidong C. and WEN W. (2014), *A Quantitative Model of Keyhole Instability Induced Porosity in Laser Welding of Titanium Alloy*, Journal of Metallurgical and Materials Transactions A, Vol 45, PP.2808–2818.

96- Alireza A. , Ahmed S. A. and Abu Syed K. (2020),*Microstructural Characterization and Mechanical Properties of Fiber Laser Welded CP-Ti and Ti-6Al-4V Similar and Dissimilar Joints*, Journal of Metals , Vol.10,PP. 747.

97- Jan F. and Alexander F.H. K. (2014), *Undercuts in Laser Arc Hybrid Welding,* 8th International Conference on Photonic Technologies LANE.

98- Himani S. P. (2019), *Phenomena in material addition to laser generated melt pools,* AThesis to Luleå University of Technology Department of Engineering Sciences and Mathematics Division of Product and Production DevelopmenSubmitted in Partial Fulfillment of the Requirements for the Degree of Doctor of Philosophy.

99- Kaplan H.F.A. and Powell J. (2011), *Spatter in laser welding*, Journal of Laser Applications,Vol. 23.

100- Dongsheng W., Xueming H., Fang L. and Lijin H. (2017), *Understanding of spatter formation in fiber laser welding of 5083 aluminum alloy*, Journal of International Journal of Heat and Mass Transfer, Vol. 113, PP. 730–740.

101- Tongtong L., Renzhi H., Xin C., Shuili Go. and Shengyong P. (2018), *Localized boiling-induced spatters in the high-power laser welding of stainless steel: three-dimensional visualization and physical understanding*, Journal of Applied Physics A, Vol. 124, Article number.654.

102-Mikell P. G. (2010), *Fundamentals of Modern Manufacture (Materials, Processes, and Systems)*, 4th Edition, John Wiley & Sons, Inc.

103- Xianguo Li., XIE J. and ZHOU Y. (2005), *Effects of oxygen contamination in the argon shielding gas in laser welding of commercially pure titanium thin sheet*, Journal of Materials Science, Vol. 40, PP. 3437 – 3443.

104- Duradundi S.B, Krishna S. P. and Buvanashekaran G. (2009), *The Effect of Laser Beam Welding on Microstructure and Mechanical Properties of Commercially Pure Titanium*, Journal of International Journal of Material Science, Vol 4, PP. 299–312.

105-Mohammed. J. T., Malek G F., Papan E. and Dadras S. (2012), Process Optimization in Titanium Welding with Pulsed Nd:YAG Laser, Journal of Science of Advanced Materials, Vol. 4, pp. 489–496.

106- Squillace A., Prisco U., Ciliberto S. and Astarita A. (2012), *Effect of welding parameters on morphology and mechanical properties of Ti–6Al–4V laser beam welded butt joints*, Journal of Materials Processing Technology**,** Vol. 212,PP. 427-436.

107- Shirguppikar S.S., Ganachari S.V., Dhaingade S.P. and Apte D.A. (2014), *Study of Laser Welding Technique for Titanium Alloy Sheet*,

International Journal of Advanced Engineering Research and Studies, ISSN,2249–8974.

108- Pakniat M., Malek G. F. and Mohammed .J. T. (2016), *Hot cracking in laser welding of Hastelloy X with pulsed Nd:YAG and continuous wave fiber lasers*, Journal of Materials and Design,Vol. 106,PP.177–183.

109- Ceyhun K. and Engin K. (2017), *Robotic Nd:YAG Fiber Laser Welding of Ti-6Al-4V Alloy*, Journal of Metals ,Vol. 7,PP. 221.

110-Ruifeng Li., Feng Z., Tianzhu S., Bin L., Shujin C. and Yingtao T. (2019), *Investigation of strengthening mechanism of commercially pure titanium joints fabricated by autogenously laser beam welding and laser-MIG hybrid welding processes*, The International Journal of Advanced Manufacturing Technology, Vol. 101,PP. 377–389.

111- Fedor F., Martin F., Volker V., Pedro A., Stefan B. and Nikolai K. (2018), *Metallurgical aspects of joining commercially pure titanium to Ti-6Al-4V alloy in a T-joint configuration by laser beam welding*, The International Journal of Advanced Manufacturing Technology, Vol. 97,PP. 2019–2031.

112- Ahmad C., Meng-Fu H., Timotius P., Masahiro T. and Wojciech Z. M.(2020), *Microstructure and mechanical properties of laser welded Ti–10V–2Fe–3Al (Ti1023) titanium alloy*, Journal of Materials Research and Technology Volume 9, PP. 7721-7731.

113- Na Q., Xiaohong Z., Shuai C., Dan C. and Shi H. (2020), *Effect of Laser Power on Tensile Performance of TA15 Laser-Welded Lock Bottom Joint*, Journal of Metals and Materials International, Vol. 27, PP.4645-4656.

114- Peter O., Rasheedat M., Nana A., Sisa P., Samuel S., Yasuhiro O., Togo S., Martin M., Tien-Chien J. and Esther A. (2021), Laser Butt Welding of Thin Ti6Al4V Sheets: Effects of Welding Parameters, Journal of Composites Scince,Vol.5,PP.246.

115-InagakiI.,Tsutomu T.,Yoshihisa S.N.A.(2014), *Application and Features of Titanium for the Aerospace Industry*, Journal of Materials Science.

116- Xinjin C., Abu Syed H. K., Priti W., Javad G., Anand B., Jonathan C., and Mamoun M. (2014), *Global and Local Mechanical Properties of Autogenously Laser Welded Ti-6Al-4V*, Journal of *Metallurgical and Materials Transactions A*, Vol. 45, PP.1258–1272.

117- Baohua C., Chris A., Jon B., Paul H. and Dong D. (2014), *Fluid Flow Characteristics and Porosity Behavior in Full Penetration Laser Welding of a Titanium Alloy*, Journal of Metallurgical & Materials Transactions. Part B, Vol. 46, PP.906-918.

118- Jilabi A.S. J. A.Z. (2015), *Welding of Rail Steels*, A thesis submitted to the University of Manchester for the degree of PhD in the Faculty of Engineering and Physical Sciences.

119- Ghusoon R M., Ishak M.,Aqida N.S. and Hassan A. A. (2017),*Weld bead profile of laser welding dissimilar joints stainless steel*,4th International Conference on Mechanical Engineering Research (ICMER2017).

120- Murav'ev I.V. (2005), *Problems of Pore Formation in Welded Joints of Titanium Alloys*, Journal of Metal Science and Heat Treatment, Vol. 47, PP. 7 – 8.

121- Zhimin W., Lulu S., Wenchao K., Zhi Z., Wei Y. and Chunming W. (2020), Laser Oscillating Welding of TC31 High-Temperature Titanium Alloy, Journal of *Metals*,Vol. 10, PP.1185.

122- Kezhao Z., Chaowei H., Dong L., Chunyan Y., Hong Z.N., Zhibin Y., Yefeng B.,(2022), Fiber laser welding of dissimilar titanium (Ti-6Al-4V/cp-Ti) T-joints and their laser forming process for aircraft application, Journal of Materials Research and Technology,Vol.17, PP.1652-1661.

123- Beguin D.J, Gazagne V., Balcaen Y., Alexis J. and Andrieu E. (2022), *Laser Welding of Titanium Alloys with an Yb: YAG Disk Source,Journal of* Materials Science Forum,Vol. 941, PP. 845-850.

124- Tim P., Yuan T., Mana A., Osamu K., Masami M., and Wojciech M. (2017), Welding of titanium alloys,MATEC Web of Conferences 123 (ICPMMT).

125- Liua H., Nakatab K., Zhanga X.J., Yamamotoc N. and Liao j.,(2012), *Microstructural evolution of fusion zone in laser beam welds of pure titanium,* Journal of Materials Characterization, Vol. 65, PP. 1-7.

126- Cui L., Kutusna M., Simizu T. and Horio K. (2009), *Fiber laser-GMA hybrid welding of commercially pure titanium Journal of* Materials and Design, Vol. 30, PP. 109-114.

127- Seyed R. E.H., Kai F., Pulin N., Ke Z., Jian H., Yuan C., Da S., Zhuguo L., Baochao G. and Song X. (2018), *Fracture surface characterization of laser welding processed Ti alloy to stainless steel joints,* Journal of Welding in the World, Vol. 62, PP.947–960.

128- Xiuyang F. and Jianxun Z. (2014), Effect of underfill defects on distortion and tensile properties of Ti-2Al-1.5Mn welded joint by pulsed laser beam welding, The International Journal of Advanced Manufacturing Technology, Vol. 74,PP.699-705.

Appendix

Appendix

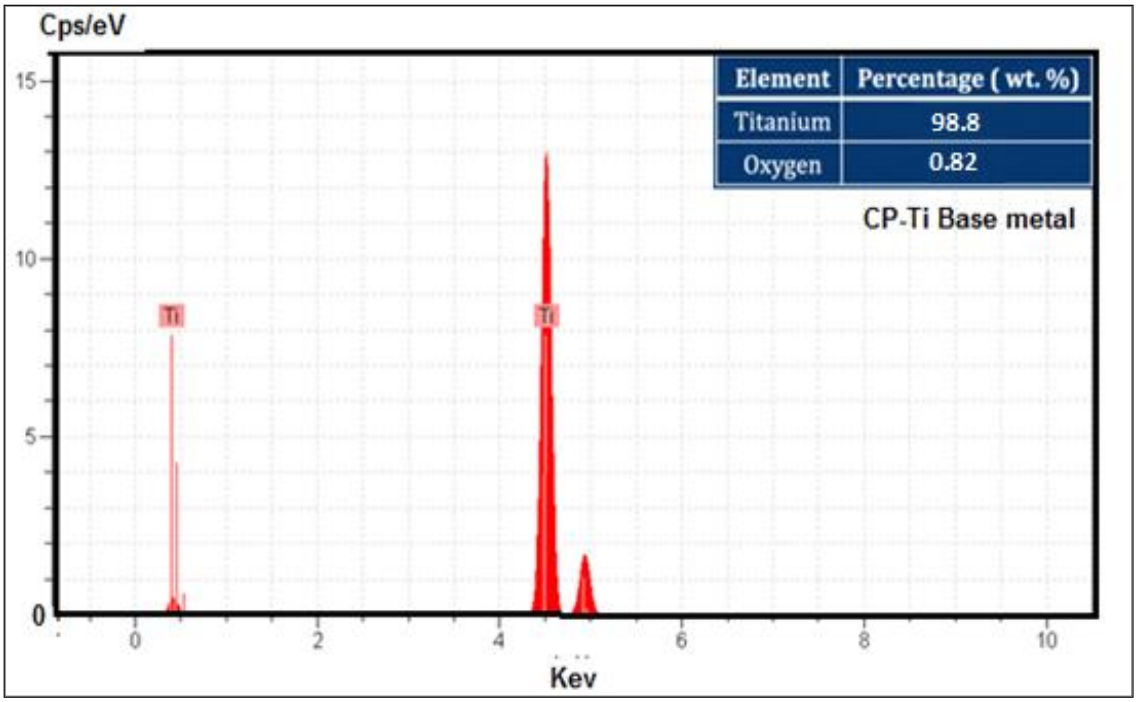
Cps/eV
15
10
5
0
Ti
Ti
0
2
4
6
8
10
Kev
Element
Percentage (wt. %)
Titanium
98.8
Oxygen
0.82
CP-Ti Base metal

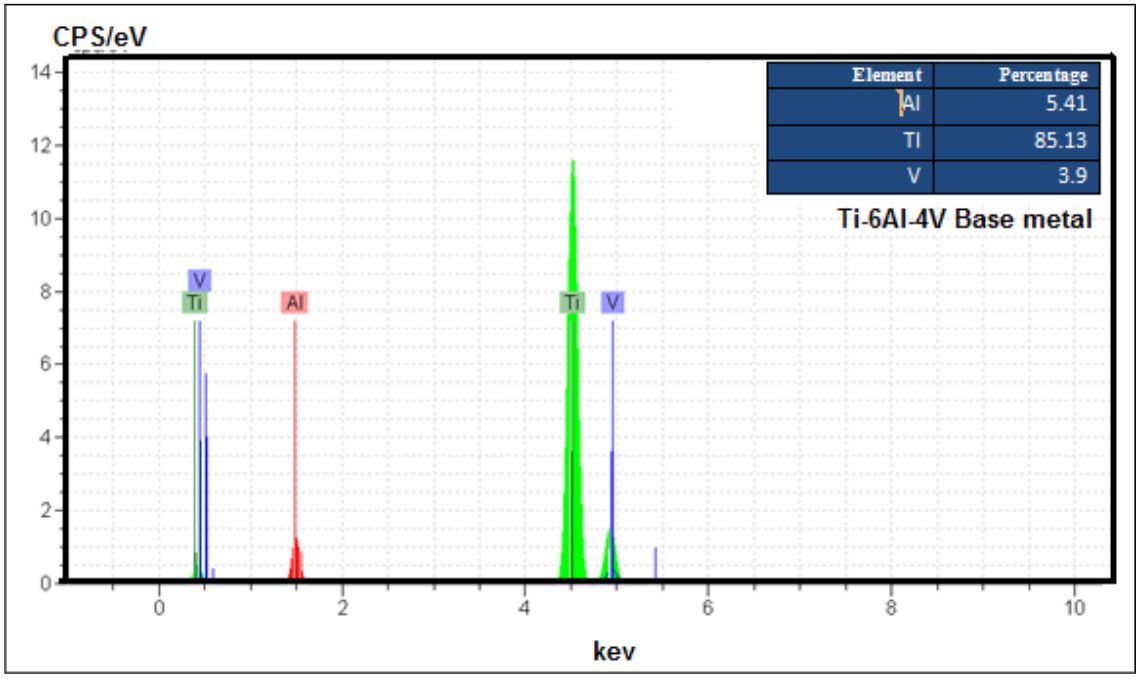
CPS/eV
14
12
10
8
6
4
2
0
V
Ti
Al
Ti
V
0
2
4
6
8
10
kev
Element
Percentage
Al
5.41
Ti
85.13
V
3.9
Ti-6Al-4V Base metal


Stress-Strain
A12
867.05
780.34
693.64
606.93
520.23
433.52
346.82
260.11
173.41
86.70
0.00
Stress
0.00
0.042
0.056
0.070
0.083
0.097
0.111
0.125
0.139
strain


Stress-Strain
B12
2104.35
1893.91
1683.48
1473.04
1262.61
1052.17
841.74
631.30
420.87
210.43
0.00
stress
0.000
0.115
0.138
0.160
0.183
0.206
0.229
strain